Doctoral Dissertation
Doctoral Program in Metrology (35^{th}cycle)

High accuracy Yb optical lattice clock: frequency comparisons and contributions to International Atomic Time

By

Irene Goti

******

Supervisor(s):
Dr. Davide Calonico, Supervisor, INRiM
Dr. Marco Pizzocaro, Co-Supervisor, INRiM

Doctoral Examination Committee:
Prof. Livio Gianfrani, Referee, University of Campania *Luigi Vanvitelli*
Dr. Belfi Jacopo, Referee, Leonardo Company

Politecnico di Torino
2023

Declaration

I hereby declare that the contents and organization of this dissertation constitute my own original work and do not compromise in any way the rights of third parties, including those relating to the security of personal data.

Irene Goti
2023

* This dissertation is presented in partial fulfillment of the requirements for **Ph.D. degree** in the Graduate School of Politecnico di Torino (ScuDo).

Abstract

During my PhD at the Politecnico di Torino, I worked at the Italian National Institute of Metrological Research (INRiM) in the field of frequency standards. In particular, in these three years, my research activity has been focused on the improvement and characterization of IT-Yb1, a Ytterbium optical lattice clock developed at INRiM.
In the last decades, a great effort has been made to develop optical clocks, which are considered the most promising candidates for the redefinition of the second in the International System of Units (SI). Indeed, optical clocks have the potential to improve by several orders of magnitude the accuracy of the current definition of the second, which is based on the hyperfine transition of the ground state of the Caesium atom.
During these three years, I have succeeded in improving both the accuracy of IT-Yb1 and its robustness. In particular, I have characterized IT-Yb1, achieving a fractional frequency systematic uncertainty of 2×10^{-17}, the smallest uncertainty ever reported for our clock. To reach this goal, I worked on the implementation of an upgraded optical setup for the realization of a vertical optical lattice and on the characterization of several systematic shifts affecting the clock frequency, such as the lattice shift and the DC Stark shift. Moreover, I worked on the robustness and the clock's reliability, trying to make its operation as continuous as possible. Significantly, in the last two years, IT-Yb1 has proven to be very reliable, operating almost continually for 14 months with an uptime of up to 75% in some weeks.
The highlights of my PhD are summarized in the following. First, an absolute frequency of IT-Yb1 was performed against the primary frequency standard developed at INRiM, the Caesium fountain clock IT-CsF2. In addition, in the last few years, IT-Yb1 has participated in several international comparison campaigns in collaboration with other European and Asian National Metrology Institutes. Furthermore, IT-Yb1 is among the eight optical clocks that have ever submitted data to the Bureau International des Poids et Mesures (BIPM) to contribute to the calibration of the

International Atomic Time (TAI). Remarkably, in the last year, IT-Yb1 has regularly contributed to the steering of TAI for 14 consecutive months, showing impressive continuity and robustness. All these results are a clear demonstration of the importance of IT-Yb1 in the international scenario of optical clocks and represent a significant contribution to the future redefinition of the SI second based on an optical standard.

Finally, during the third year of the Ph.D., I spent four months with an Erasmus+Traineeship fellowship at the Laboratoire Charles Fabry in Palaiseau (France), where I worked on the Cyclopix project. In this experiment, the light-scattering of a Rb atomic sample trapped in an optical dipole trap is studied to observe the collective effects in the light emitted by the atoms. This internship was a great opportunity to learn new cooling and trapping techniques, such as optical tweezers, that can be useful for the realization of a new generation of optical clocks.

Contents

Chapter 1

Introduction

Time is one of the seven fundamental physical quantities in the International System of Units (SI). On 20 May 2019, the SI base units were officially redefined. As

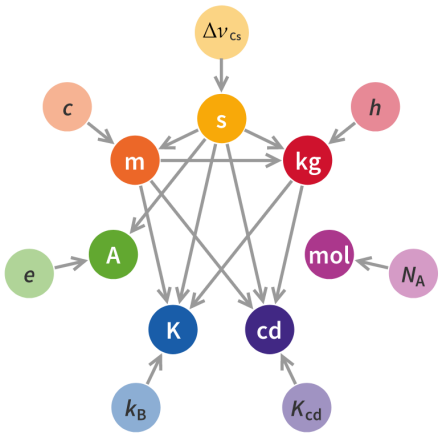

Fig. 1.1 Scheme of the new SI after the last redefinition in 2019.

schematized in Fig. 1.1, from that moment, the definitions of all the seven SI base units (the second, the meter, the kilogram, ampere, kelvin, the mole and the candela) are intrinsically connected to the numerical value of seven physical constants: the hyperfine transition frequency of Caesium ($\Delta\nu_{\mathrm{Cs}}$), the speed of light in vacuum (c), the Planck constant (h), the elementary electric charge (e), the Boltzmann constant (k_{B}), the Avogadro constant (N_A) and the luminous efficacy (K_{cd}) respectively.
From Fig. 1.1, we note that all the other base units, except the mole, directly depend on the definition of the second. This dependence put the SI second in a particularly prominent position.

Time and frequency metrology is the field of physics that studies the definition and the measurement of the second, the development of international timescales, and the comparison between different standards. In the last decades, the development of atomic manipulation techniques and the progress in the field of coherent electromagnetic radiations have led to the implementation of atomic clocks, which currently are the most accurate time standards. The current definition of the SI second is based on the transition frequency of the ^{133}Cs atom, in the microwave regime. But recently, the development of optical atomic clocks, which have shown better accuracy and lower instability than microwave clocks, has opened the possibility of redefining the SI second in the optical regime.
In this Chapter, I will present the current definition of the SI second (Section 1.1), and I briefly describe the operating principle of atomic clocks and its fundamental limits (Section 1.2). Next, in Section 1.3, I will give an overview of the different ongoing techniques to implement an optical frequency standard. The main metrological application of optical clocks, i.e., clocks comparisons and the contribution to the International Atomic Time, are described in Section 1.4. Finally, in Section 1.5, I will introduce some of the most promising proposals for the construction of next-generation optical clocks.

1.1 Definition of the SI second

Since 1967, the definition of the SI second is based on the unperturbed hyperfine transition frequency of the ground state of the ^{133}Cs atom, which thus represents the primary representation of the SI second. The current official definition, effective from 2019, is as follows:

> *The second, symbol s, is the SI unit of time. It is defined by taking the fixed numerical value of the Caesium frequency $\Delta\nu_{Cs}$, the unperturbed ground-state hyperfine transition frequency of the caesium133 atom, to be 9192631770 when expressed in the unit Hz, which is equal to s^{-1}*

Although the performance of primary Cs standards and more in general of microwave clocks has constantly improved since their introduction, the best Cs fountain clocks worldwide are limited by a fractional uncertainty of about 2×10^{-16} [1–5]. This limit can be overcome by using optical radiations and optical atomic transitions

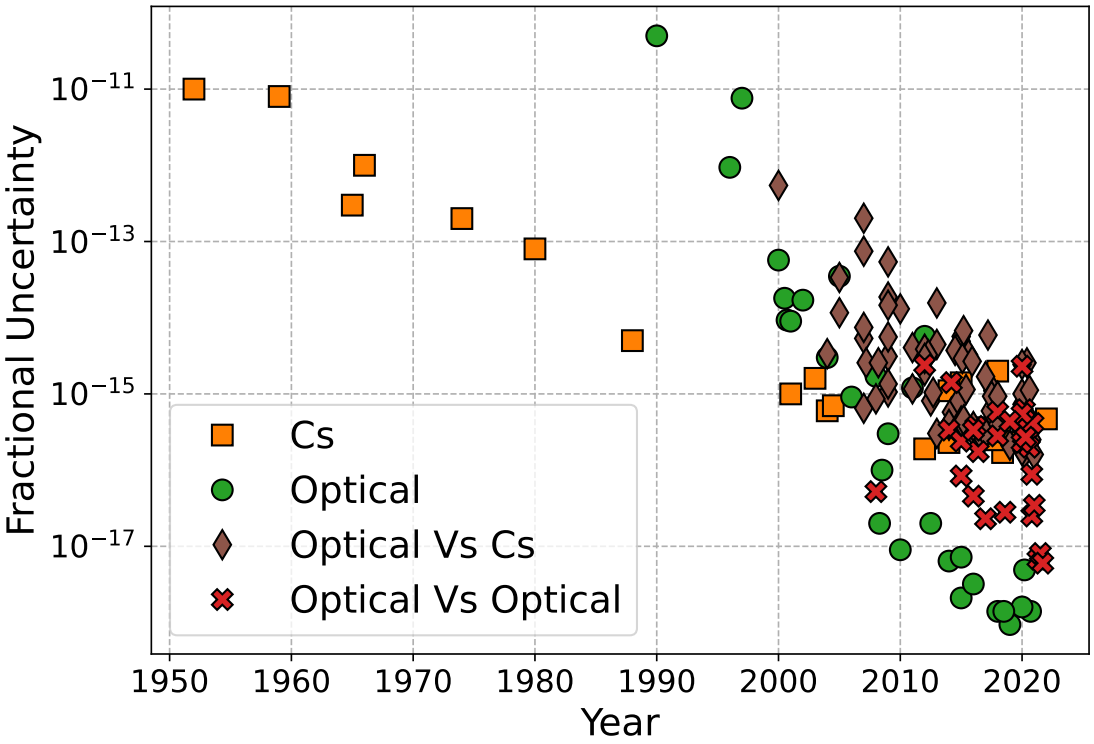

Fig. 1.2 Improvement over the years of frequency standards in terms of fractional uncertainty. Primary standards, i.e., Cs clocks, are shown as orange squares, while optical clocks are represented as green circles. Brown diamonds represent the fractional uncertainty of optical standard absolute frequency measurements evaluated through a comparison with Cs clocks. We note that the results of these measurements have a fractional uncertainty comparable to the Cs clocks, thus suggesting that optical clocks do not significantly contribute to the uncertainty. Finally, red crosses represent the fractional uncertainty of comparison measurements between optical clocks. The data used in this Figure are taken from the BIPM website [6], updated to February 2023.

as a frequency standard. Indeed, the improvement in laser cooling and trapping techniques and ultra-stable lasers, together with the development of frequency combs, has allowed the realization of optical clocks. In particular, in recent years, it has been widely demonstrated that optical clocks represent better frequency standards [7–10], both in terms of fractional frequency instability and estimated systematic uncertainty. Figure 1.2 shows the progress in the performance of optical clocks compared to Cs clocks. In particular, orange squares represent the progress over the last decades in the performance of Cs clocks in terms of fractional uncertainty, while green

circles represent the systematic fractional uncertainty of optical clocks. We note that, nowadays, optical clocks have a better fractional uncertainty of more than two orders of magnitude than the best primary standards. In addition, the Figure reports the fractional uncertainties of frequency measurement comparison between optical clocks and Cs clocks (brown diamonds) and between two optical clocks (red crosses). Interestingly, the uncertainty affecting the more recent frequency measurements of optical clocks against Cs standards is comparable to the uncertainty of the Cs clocks themselves. From this, it is possible to deduce that the performance of the clocks comparisons is limited by the uncertainty of Cs clocks. The data used in this Figure

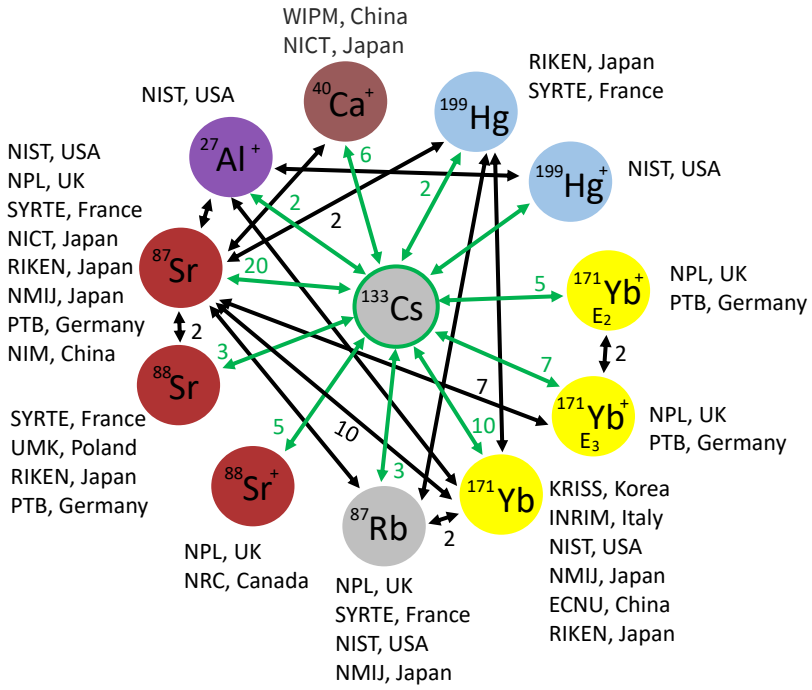

Fig. 1.3 Representation of the SRS indicated by the CCTF arranged around the primary frequency standard. The performed absolute frequency measurement against the Cs clock and ratio measurements are represented as green and black arrows, respectively. The numbers indicate how many times each comparison has been carried out, where this value differs from 1. The data are taken from the BIPM website, updated to February 2023 [6]. The National Metrological Institutes (NMIs) that implemented the optical clocks and performed the measurements are also reported.

are taken from the International Bureau of Weights and Measures (BIPM) website [6], updated to February 2023. The BIPM is the international organization established by the Metre Convention responsible for the realization of the International System of

Units (SI) and dissemination of the SI units. In particular, the BIPM is in charge of the establishment of time scales, such as the International Atomic Time (TAI) and the Coordinated Universal Time (UTC), described more in detail below in Section 1.4.1. Another international metrological organization is the International Committee for Weights and Measures (CIPM), an advisory committee composed of 80 metrologists of high standing. The CIPM has established several Consultative Committees (CC), including the Consultative Committee for Time and Frequency (CCTF). Since the early 2000s, the CCTF indicated specific atomic transitions as recommended values of standard frequencies. Among these, those characterized by an uncertainty comparable to that of a Cs fountain, are selected as a secondary representation of the second (SRS), including the transition $^1S_0 \rightarrow ^3P_0$ of ^{171}Yb, which is the object of this thesis. As explained in Section 1.4.1 and Chapter 5, the SRS may submit data to the BIPM to contribute to the realization of TAI. Figure 1.3 schematically illustrates the SRS and the number of absolute frequency measurements performed relative to the primary Cs standard (green arrows). Moreover, black arrows represent the frequency ratio measurement between two SRS. In addition, the National Metrological Institutes (NMIs) and the research institutes that developed the SRS and performed these comparison measurements are indicated.

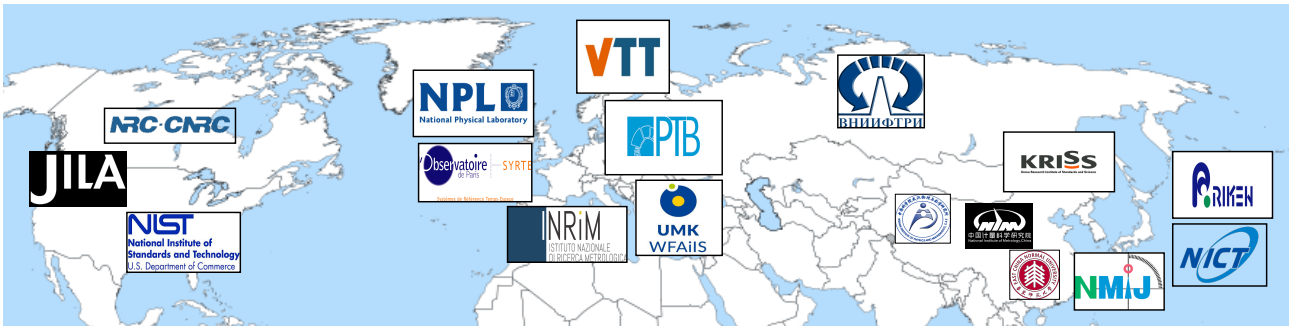

Fig. 1.4 Representation of National Metrological Institutes (NMI) and research labs studying optical clocks worldwide.

Figure 1.4 shows the worldwide distribution of the major NMIs and research labs that are developing an optical clock. The abundance of research groups and NMIs involved in the implementation of atomic clocks and their comparisons demonstrate the relevance of this research field and the interest of the scientific community.

Towards a redefinition of the SI second

The progress in the field of optical clocks achieved in the last years paves the way for a redefinition of the SI second [11–13]. In 2022, the CCTF published a roadmap [14, 15] stating relevant milestones to be achieved to proceed to a redefinition of the SI second. The main goals are:

- Validation that Optical Frequency Standards (OFS) are 100 times better than Cs clock, i.e., characterized by a fractional uncertainty of 10^{-17}-10^{-18}.
- Ensures continuity with the current definition of the SI second. This requirement is accomplished by measuring the frequency of the OFS relative to the primary Cs standard with a fractional uncertainty $\frac{\Delta\nu}{\nu} < 3 \times 10^{-16}$ limited by the Cs clock [13].
- Comparisons between OFS (same species or frequency ratio) with an agreement better than $\Delta\nu/\nu < 5 \times 10^{-18}$. This would ensure the high reliability of OFSs.
- Regular cotribution of OFS to TAI as SRS.

At present, it is not clear which is the best candidate among the SRS for a future redefinition of the second. A recent proposal suggests following a different approach and defining the second as a composite frequency unit based on the weighted mean of several atomic transition values [12].
Based on the current situation, the estimated timeline for the new definition of the second is around 2030 [14].

1.2 Atomic clocks

An atomic clock consists of three main components: the local oscillator (LO), the atomic reference and a frequency correction system. The local oscillator is the source of electromagnetic radiation used to interrogate the atomic frequency reference. The frequency reference is a transition between two specific energy levels of an atom and, being an intrinsic property of the atomic species, it is a quantity well reproducible.

The LO is kept resonant with the atomic transition by a correction loop, and its frequency is measured with a counter.
The performance of an atomic clock is evaluated in terms of accuracy and stability. The accuracy is the difference between the measured frequency and its unperturbed value. The accuracy of an atomic clock is affected by systematic effects caused by environmental factors that perturb the clock transition. Therefore, all these systematic effects and their uncertainties must be quantified, to ensure high clock accuracy. The result of this characterization is usually summarized in the so-called *accuracy budget* of the atomic clock. Instead, the stability of a clock is the variation of the measured frequency over time. It is a statistical quantity and is usually calculated as the Allan deviation $\sigma_y(\tau)$ [16, 17], which describes the root mean square random drift error as a function of average time τ. When only the contribution of the white frequency noise is considered, the instability of the clock is proportional to $\tau^{-1/2}$.

1.2.1 Fundamental limits of an atomic clock

Quantum projection noise

The instability of an atomic clock subject to white frequency noise is given by [18]:

$$\sigma_y(\tau) = \frac{1}{K}\frac{1}{SNR}\frac{\Delta\nu}{\nu_0}\sqrt{\frac{T}{\tau}} \tag{1.1}$$

where K is a parameter close to the unity that depends on the spectroscopic technique used to interrogate the clock transition, $\Delta\nu$ is the linewidth of the transition, ν_0 is the clock frequency, T is the duration of a clock cycle, τ is the total averaging time of the measurement and $SNR = S_{\max}/\delta S$ is the signal-to-noise ratio of the measurement and it is defined as the ratio between the maximum signal $S_{\max}$ and the noise δS evaluated at a measurement time $\tau = 1\,\mathrm{s}$.
The fundamental limitation of an atomic clock stability is represented by the quantum projection noise (QPN) [19]. The QPN is a quantum mechanical effect caused by the measurement process itself. When the clock transition is interrogated, the probability of finding the atom in the excited state or in the ground state is P and $1-P$, respectively. The QPN is a statistical fluctuation of the measurement result that results in a fluctuation of the detected signal δS. In particular, the signal-to-noise ratio that appears in Equation 1.1 for a sample composed of N atoms is given by

$SNR = S_{\max}/\delta S = \frac{NP_{\max}}{\sqrt{NP(1-P)}}$. The QPN is thus a source of noise that contributes to δS and that limits the atomic clock stability $\sigma_y(\tau)$.

Dick effect

Although the fundamental limit to the stability of an atomic clock is the QPN, the real limiting factor is usually represented by the Dick effect [20]. This effect is caused by the LO frequency noise and the clock cycle structure. In particular, the Dick effect arises because the clock transition is probed for a finite interval, smaller than the entire clock cycle time. Therefore, between two consecutive interrogations, i.e., during the dead time, the LO frequency can drift. This drift leads to aliasing effects that limit the clock stability.

The most obvious and effective strategy to improve the atomic clock instability is therefore to produce LOs the less noisy as possible. This can be achieved by stabilizing the LO to a state-of-the-art Fabry-Pérot cavity. However, with the same LO noise, the Dick effect increases with the dead time, so it is crucial to reduce the clock cycle time and maximize the interrogation time.

In literature, several approaches allowing to eliminate the Dick effect are proposed. For example, it is possible to suppress the Dick effect by operating two atomic clocks in a zero-dead-time configuration [21, 22], or by implementing quantum non-demolition measurements [23–25].

1.3 Optical clocks

An optical clock is an atomic clock whose frequency reference is in the visible range. The two main types of optical clocks are the single ion and the neutral atoms clocks. Ion clocks are based on the interrogation of a single atom confined in a Paul trap and laser-cooled to low temperatures [26–28]. On the contrary, in a neutral clock, an atomic sample of up to 10^4 atoms is cooled and trapped in an optical lattice and interrogated by the probe laser. One of the main advantages of neutral clocks is the possibility to interrogate a large number of atoms. This led to an increase in the SNR and a consequent improvement in the clock stability, as can be deduced from Eq. 1.1. On the other hand, ion clocks take advantage of specific transitions particularly insensitive to external perturbations. Therefore, at present, it is not easy to establish which type of optical clock could provide the best performance. However, both

neutral atoms and single ion clocks have better accuracy and stability compared to the best Cs fountains (Fig. 1.2) [8, 9, 29], achieving fractional uncertainty at the level of 10^{-18} after a few hours of measurement [7, 10].
Below, we will focus on neutral optical clocks and their development, which is the main topic of this thesis.

Neutral optical clocks: operating principle

Figure 1.5 schematically shows the typical clock cycle of a lattice clock. In this type of experiment, the atomic beam is produced by sublimating atoms from a solid sample. The hot atoms are then cooled and trapped in the optical lattice by combining the action of laser beams and magnetic fields (panel a). After that, all the laser beams and the magnetic field are switched off, and the atoms remain in the lattice (panel b). This step is crucial to prevent external electromagnetic fields from perturbing

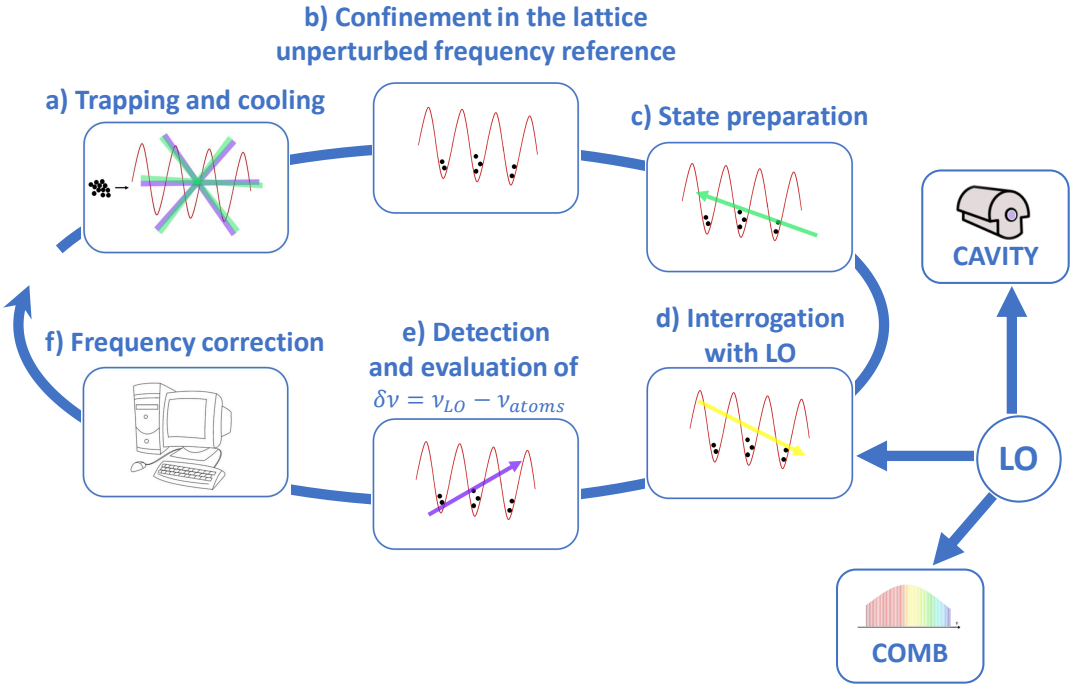

Fig. 1.5 Schematic representation of a lattice clock cycle divided into several phases (a-f). The local oscillator used to interrogate the clock transition is illustrated on the right. It is stabilized through a cavity and its frequency is measured by a frequency comb.

the clock transition. Then, the atomic sample is prepared in the ground state of the clock transition (panel c) and subsequently is interrogated with the probe laser (panel

d). The fraction of atoms that populate the excited state of the clock transition is detected by a fluorescence measurement (panel e). From this signal, it is possible to calculate the frequency detuning between the clock laser and the atomic reference $\delta\nu = \nu_{LO} - \nu_{atoms}$. Finally, the frequency of the LO is thus digitally corrected to make it resonant with the atomic transition (panel f). Since the detection procedure is a destructive process, the atoms have to be reloaded into the lattice before proceeding with another clock interrogation.
In the next Chapter, each step of the clock cycle will be described in detail.
As schematized, the LO is frequency stabilized on an ultra-stable Fabry Pérot cavity, and its frequency is continuously measured through an optical frequency comb.

How to count the LO frequency

A frequency comb is a femtosecond pulsed laser whose spectrum is composed of several equally spaced lines (or teeth) in the frequency domain [30]. Figure 1.6 shows the spectrum of a frequency comb. The frequency of the n^{th} tooth is de-

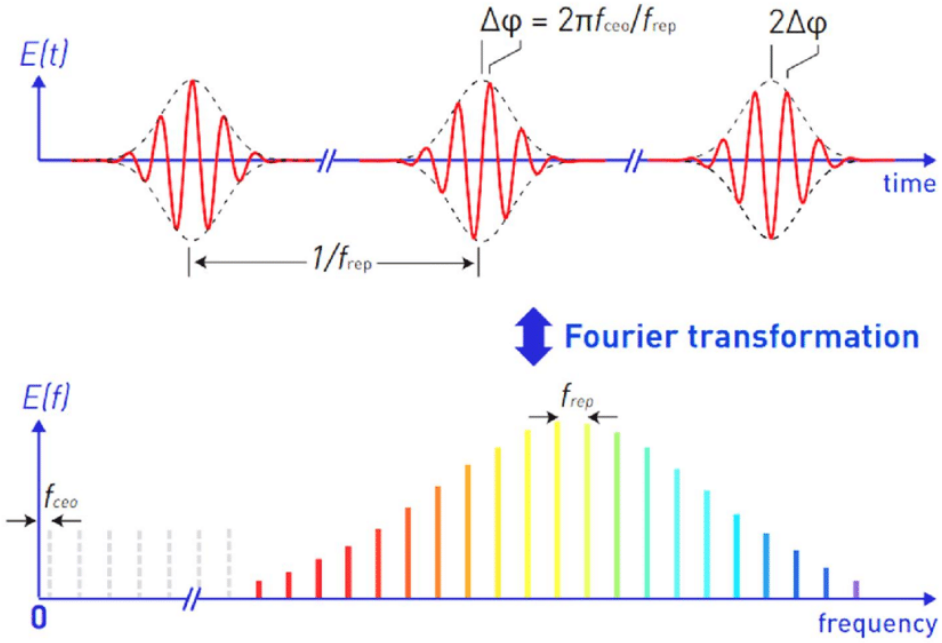

Fig. 1.6 Representation of the electric field of the femtosecond pulsed laser that composes the frequency comb, adapted from [31]. The corresponding spectrum in the frequency domain is calculated as the Fourier transform of the electric field. The frequency spectrum of the comb consists of a series of lines equally spaced.

termined by two quantities: the repetition rate f_{rep} and the carrier-envelope offset frequency f_{CEO}. f_{rep} is the separation in frequency between two consecutive teeth, while $f_{\text{CEO}} = f_{\text{rep}} \frac{\Delta\phi}{2\pi}$ where $\Delta\phi$ is the phase difference between two pulses of the femtosecond laser. In particular, the frequency of the n^{th} tooth is given by:

$$f_n = n \times f_{\text{rep}} + f_{\text{CEO}} \tag{1.2}$$

To evaluate the frequency of the optical clock f_{clock}, the LO radiation is sent to the frequency comb and its beat note with the nearest comb line is measured.
The frequency comb is the instrument that allows us to down-convert the frequency of an optical clock in the microwave domain. By using a frequency comb, it is thus possible to directly compare the frequency of two optical clocks, as well as the frequency of an optical clock and a primary Cs frequency standard [32].

1.4 Metrological Applications

1.4.1 Contribution to the International Atomic Time

One of the primary applications of optical clocks is the contribution to the calibration of the International Atomic Time (TAI). Furthermore, this is also one of the requirements reported in the roadmap for the redefinition of the second. TAI is a time scale defined by BIPM and is based on the weighted average of the frequency value measured by over 450 atomic clocks worldwide. Most of the frequency standards used to evaluate TAI consist of Cs atomic clocks, but recently also optical clocks have started to contribute to the realization of TAI [33], as described in Section 5.3. Since 1977, TAI is evaluated starting from another time scale called EAL (échelle atomique libre) [34], as illustrated in Fig. 1.7. EAL is a scale generated by the monthly contributions of a large ensemble of free-running and commercial atomic clocks. TAI is produced from the frequency value of EAL, corrected each month of a quantity evaluated by comparing the EAL frequency with the frequency of the primary and secondary frequency standards that were running during that month. This correction is called "steering". By following this procedure, TAI results in a very stable time scale, consistent with the definition of the SI second [35]. All the monthly contributions to TAI are published by BIPM in the so-called Circular T [36],

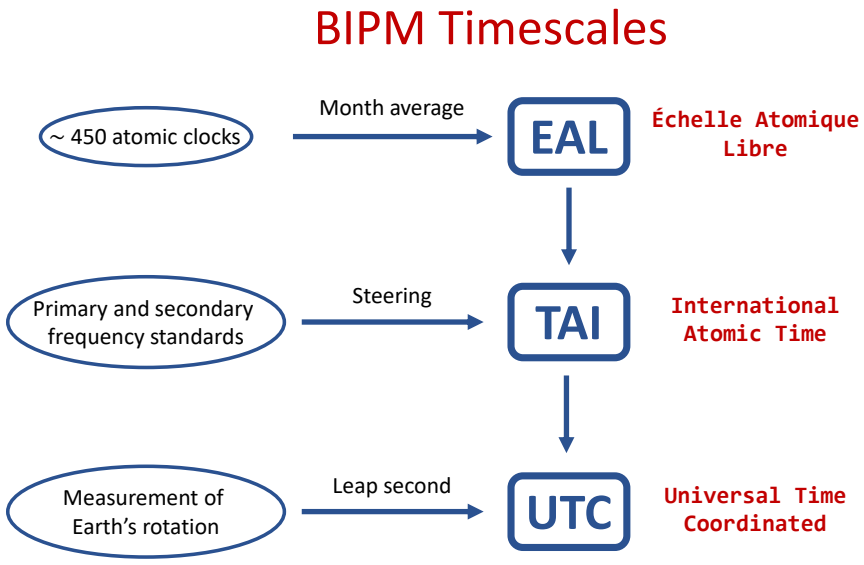

Fig. 1.7 Scheme of the realization of different time scales defined by BIPM. The contributions of primary and secondary frequency standards serve to correct (or steer) the EAL frequency and to obtain TAI.

a bulletin that reports the technical information about the primary and secondary standards used to steer TAI.
As schematized in Fig. 1.7, from TAI is obtained UTC (Universal Time Coordinated), the most common time scale used in everyday life. UTC is evaluated from TAI by adding a leap second when necessary, to compensate for an eventual difference between TAI and the time measured through the rotation of the Earth [37]. Currently, the difference between TAI and UTC amounts to 37 leap seconds, but basically, the frequency of the two timescales is the same. In the following, I will refer to TAI for correctness, but the same considerations can be applied to UTC.

1.4.2 Atomic clocks comparisons

As anticipated in Section 1.1, the completion of optical clock comparisons against a primary frequency standard and other optical clocks represents one of the milestones that must be achieved to proceed toward the redefinition of the SI second. In this context, there are two main types of clock comparisons: local and remote. When a local comparison is performed, both the clock under test and the reference clocks

are located in the same laboratory or research institute. On the contrary, in a remote comparison, the two clocks may be placed very far away from each other. In the latter case, the comparison can occur via different methods, such as satellite techniques and optical links. As well as for comparisons against a primary frequency standard, all these techniques are suitable for measuring optical frequency ratios, i.e., for performing clock comparisons between two optical clocks.
An alternative method to measure the absolute frequency of a clock is to use as a frequency reference the value of TAI evaluated by the BIPM. In this case, the clock frequency is measured by a frequency comb against a local maser, which is then compared with TAI. The advantage of this comparison technique lies in the fact that being the frequency of TAI evaluated as a weighted average of hundreds of atomic clocks, its systematic uncertainty is usually much lower than that of comparisons against a single Cs clock. Moreover, this method does not require the availability of a Cs clock (neither local nor remote).

1.4.3 Transportable optical clocks

An important and promising tool to overcome the limitations and difficulties of the comparison techniques described above is represented by the development of transportable optical clocks (TOC). These devices are optical clocks characterized by sufficient compactness, lightness and robustness to be transported and operated outside the laboratory. In the last years, a few TOCs have been realized worldwide based both on neutral atoms and ions. In particular, the TOCs developed at PTB, University of Brimingham and Düsseldorf and RIKEN are based on neutral ^{87}Sr atoms [38–40], while that developed at China Academy of Science is based on $^{+}$Ca ions [41, 42]. The most efficient TOC shows performance comparable to laboratory-based systems.
Transportable clocks can be utilized in a variety of experiments, such as metrological comparisons, fundamental physics tests and space applications. Moreover, in a more distant future, it is expected that TOCs will be commercially available and will be employed for geodetic height measurements and synchronisations of telecommunications networks and GNSS systems. In addition, the industrialisation of TOCs would allow the distribution of optical clocks also outside the National Metrological Institutes, thus contributing to the development of the optical clock network. In this context, a prototype of a commercial TOC has been recently developed in the

German Opticlock project [43]. However, the unavailability of several key components, such as ultrastable laser with 10^{-16} fractional instability and optical setups for atomic cooling, still represents a limitation for the industrialisation of TOCs.
In the next few years, a lot of effort will be made to improve the performance of TOCs. Indeed, the European project TOCK (Transportable optical clocks for key comparisons) is currently ongoing and aims to develop TOCs characterized by a fractional uncertainty better than 5×10^{-18} and an instability lower than $5 \times 10^{-15}/\sqrt{\tau/s}$. Moreover, several European clock comparisons involving TOCs are planned within the project TOCK.

1.4.4 Other applications

The high accuracy and stability demonstrated by optical clocks make these devices appealing for several applications besides pure metrological interests. For example, optical clocks can be used to test General Relativity by measuring the gravitational red-shift of the clock transition [44]. Indeed the gravitational potential of Earth induces on clocks placed at a different altitude of about 10 cm a frequency shift of the order of 10^{-17}, that is a quantity resolved by the best developed optical clocks. This high sensitivity makes optical clocks a powerful tool to determine the gravity potential with higher accuracy than the currently employed geodetic leveling method, which combines geoid field modeling and GNSS techniques. With this method, the uncertainty of the gravity potential is of the order of a few centimeters [45, 46].
Another promising application for optical clocks is the accomplishment of experiments aiming to test the Standard Model by measuring the variation of fundamental constants. Indeed, the frequency of an atomic transition depends on the fine-structure constant α and on the mass ratio between electron and proton $\mu = m_p/m_e$. In particular, clocks based on different atomic species have a different sensitivity to the variation of these parameters. Therefore, by comparing two or more clocks, it is possible to measure a drift of the clock frequency due to a potential variation of the fundamental constants [47]. So far, no significant variation of α and μ has been observed, and the constraints on the variations of these parameters are of the order of $\dot{\alpha}/\alpha \sim 10^{-18}$/year and $\dot{\mu}/\mu \sim 10^{-17}$/year [48].
The study of the fine structure constant variation is also relevant for the detection of dark matter [49, 50]. Indeed, the presence of a dark matter cluster in the vicinity

of the Earth would induce a variation of the fine structure constant, which can be detected by comparing the frequency of optical clocks in different locations. Also for this type of experiment, no relevant variation of α has been detected, and the recent experiment involving optical clocks at NPL, SYRTE and PTB [51] resulted in a measured constraint of $|\frac{\delta\alpha}{\alpha}| < 5 \times 10^{-17}$.
Other reasons for interest in the field of optical clocks are the possibility of improving the resolution of VLBI techniques [52] and global navigation satellite systems [53].

1.5 Next generation clocks

In the last few years, much progress has been made in the research field of optical clocks. These have led to several improvements in the ion and lattice clocks, but also to the development of new types of optical clocks. Among various ideas to develop the next generation atomic clocks, some of the most promising are based on the optical tweezer technique [54, 55]. This method represents a powerful tool to manipulate the atom and to have good control of the atomic state. In particular, an optical tweezer is a laser cooling technique that exploits a focused laser beam to trap down to a single atom. Moreover, it is possible to create a long-lived entangled state [56] by combining the tweezer technique with Rydberg excitations [57]. If this kind of state is used as the atomic reference of a clock, the corresponding stability is expected to be better than the stability of a traditional optical clock. In addition, this atomic system would offer the possibility to execute several quantum metrology experiments.
Another interesting research field in the frequency metrology context is the development of chip-scale atomic clocks [58–60]. These devices are based on microwave transition in warm vapors of alkali metals and exploit a phenomenon called coherent population trapping (CPT) which allows for eliminating the microwave cavity. In this way, the clock side is drastically reduced. The drawback is relatively poor long-term stability, of the order of $3 \times 10^{-12}\, 1/\sqrt{\tau}$ [61]. Recently, chip-scale lasers are being developed [62], paving the way to the realization of chip-scale optical clocks. Besides being important for military purposes, chip-scale atomic clocks are also interesting for several civil applications, such as GNSS navigation and time synchronization.
One of the last ideas proposed to develop an optical clock involves the nuclear

transition of ^{229}Th [63, 64]. This isotope is a promising candidate for the realization of a high-accuracy frequency standard because it has a very long lifetime and a very low sensitivity to external perturbations. Moreover, the signal-to-noise ratio of a nuclear clock is expected to be much higher than that of an atomic optical clock, because the number of interrogated nuclei would be up to 10^{14} [64], 10 orders of magnitude higher than the number of atoms in a neutral clock. Nuclear clocks are also interesting for fundamental physics tests since the transition frequency is affected by the strong interaction and can be used to test the variation of fundamental constants [65, 66].

Chapter 2

IT-Yb1 Optical lattice clock: experimental setup

IT-Yb1 is the ytterbium optical clock developed at INRiM. Since it is a traditional neutral lattice clock, ^{171}Yb atoms are loaded into a 1D optical lattice at the magic wavelength to interrogate the unperturbed clock transition $^1S_0 \rightarrow {}^3P_0$. This transition is interrogated by our Local Oscillator (LO): a yellow laser beam at 578 nm that is stabilized on an ultrastable Fabry Pérot cavity.
In this chapter, I provide a detailed description of the experimental setup of IT-Yb1 and a theoretical overview of the cooling and trapping techniques used in the experiment.
The chapter is organized as follows. In Section 2.1, I report the spectroscopic properties of ^{171}Yb atoms and an overview of the experimental setup. In Section 2.2, I describe the clock laser generation and its stabilization apparatus. After, Section 2.3 provides an overview of the lasers used to manipulate the atoms and their stabilization. Then, Section 2.4 describes the oven and the vacuum system we use to produce the atomic beam. Finally, in Section 2.5, I present the IT-Yb1 clock cycle and, in particular, the cooling and trapping techniques used to prepare the atoms in the optical lattice, the state preparation procedure, the spectroscopic techniques utilized to interrogate Yb atoms and the detection process.

2.1 Yb optical clocks overview

2.1.1 Yb atoms

Ytterbium is an earth-alkali-like atom, and its fermionic ($I = 1/2$) isotope ^{171}Yb is worthy of attention from a metrological point of view. Indeed, ^{171}Yb presents a spin- and total angular-momentum forbidden transition ($^1S_0 \rightarrow {}^3P_0$, $\Delta S \neq 0$, $J = 0 \leftrightarrow 0$) characterized by a natural linewidth of $\gamma_{Yb} \simeq$ 7 mHz [67], narrow enough to represent a suitable frequency reference when it is not perturbed by the environment. In addition, the ^{171}Yb energy-level structure makes this isotope suitable for fast and effective laser cooling.

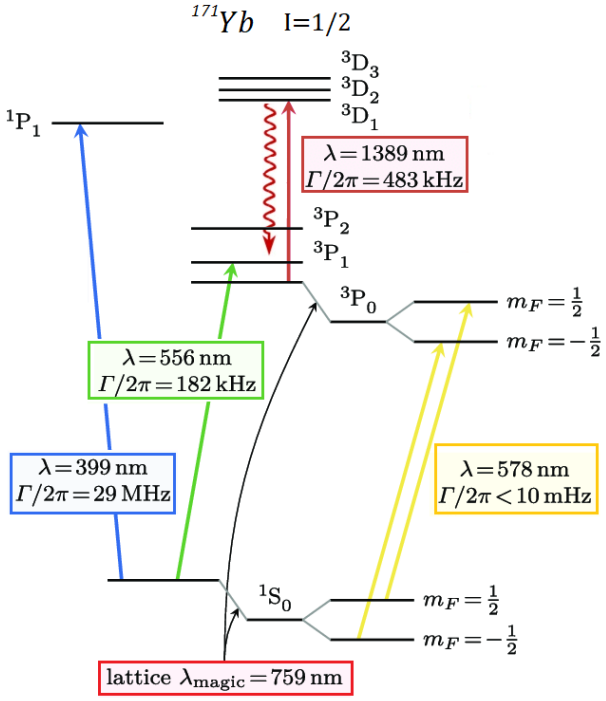

Fig. 2.1 Relevant energy levels of ^{171}Yb, from [68]. All the transitions exploited during our experiment are reported together with their linewidth. The scheme also illustrates the energy shift of the energy level composing the clock transition produced by the lattice radiation.

Figure 2.1 shows the ^{171}Yb energy levels relevant to our experiment. The clock transition at 578 nm is represented in yellow. The hyperfine splitting in different Zeeman sub-states $m_F = \pm 1/2$ is reported for each clock level $^1S_0$ and $^3P_0$. The two yellow arrows represent the two clock transitions $^1S_0 \rightarrow {}^3P_0$, $\Delta m_F = 0$ probed

during the clock operation. The Figure schematically illustrates the energy shift produced by the lattice laser on the clock levels (black arrows). The optical lattice is generated by a laser that operates at the magic wavelength [69] ($\lambda_{lattice}$ =759 nm for Yb atoms [70]) to induce the same perturbation in the two clock levels and thus to produce a zero total energy shift in the clock transition. To efficiently load the atoms in the optical lattice, it is first of all necessary to cool them. The cooling process is performed by exploiting the $^1S_0 \rightarrow {}^1P_1$ and the $^1S_0 \rightarrow {}^3P_1$ transitions at 399 nm and 556 nm, respectively. The large linewidth $\frac{\Gamma}{2\pi}$ of these transitions (29 MHz for the blue transition and 182 kHz for the green one) allows fast and efficient cooling. Finally, the scheme reports the transition $^3P_0 \rightarrow {}^3D_1$ at 1389 nm. This transition is used to repopulate the $^1S_0$ state after the clock interrogation process. Indeed, it brings the excited atoms from the $^3P_0$ level to the $^3D_1$ short-lived state. Then the atoms spontaneously decay first in the $^3P_1$ state and then in the ground $^1S_0$ state [71].

2.1.2 Overview of the experimental setup

Figure 2.2 shows a scheme of the entire optical setup of IT-Yb1. The main components of the apparatus are described in the following sections.
The atomic chamber and the oven (Sec. 2.4) are illustrated in grey in the center of the Figure. All the lasers exploited in the experiment are represented, together with the optical cavities used to stabilize them. In particular, the clock laser at 1156 nm is stabilized on an ultrastable Fabry Pérot cavity and its frequency is doubled to 578 nm (Sec. 2.2). The radiations at 798 nm, 1112 nm and 759 nm are stabilized on another cavity hereafter called "3-colors cavity" (Sec. 2.3.5). The preparation of all the laser beams takes place in different breadboards (Sec. 2.3), and then each laser beam is sent to the atomic chamber through polarization-maintaining optical fibers. The 798 nm laser is frequency doubled to obtain the blue radiation at 399 nm. This light is split in different beam paths, one of which is used for the detection, while the others are exploited to trap the atoms, i.e., for the slower and the first MOT stage. Similarly, the 1112 nm is frequency doubled to obtain the green radiation at 556 nm, which is then used for the MOT and to prepare the atomic state (this optical path is represented in Fig. 2.2 as "spin polarization"). The radiation at 759 nm is sent to the atomic chamber and generates the optical vertical lattice (Sec. 2.5.1), where atoms are trapped. The optical lattice must operate at the magic wavelength, and to ensure this condition its frequency is continuously measured by a frequency

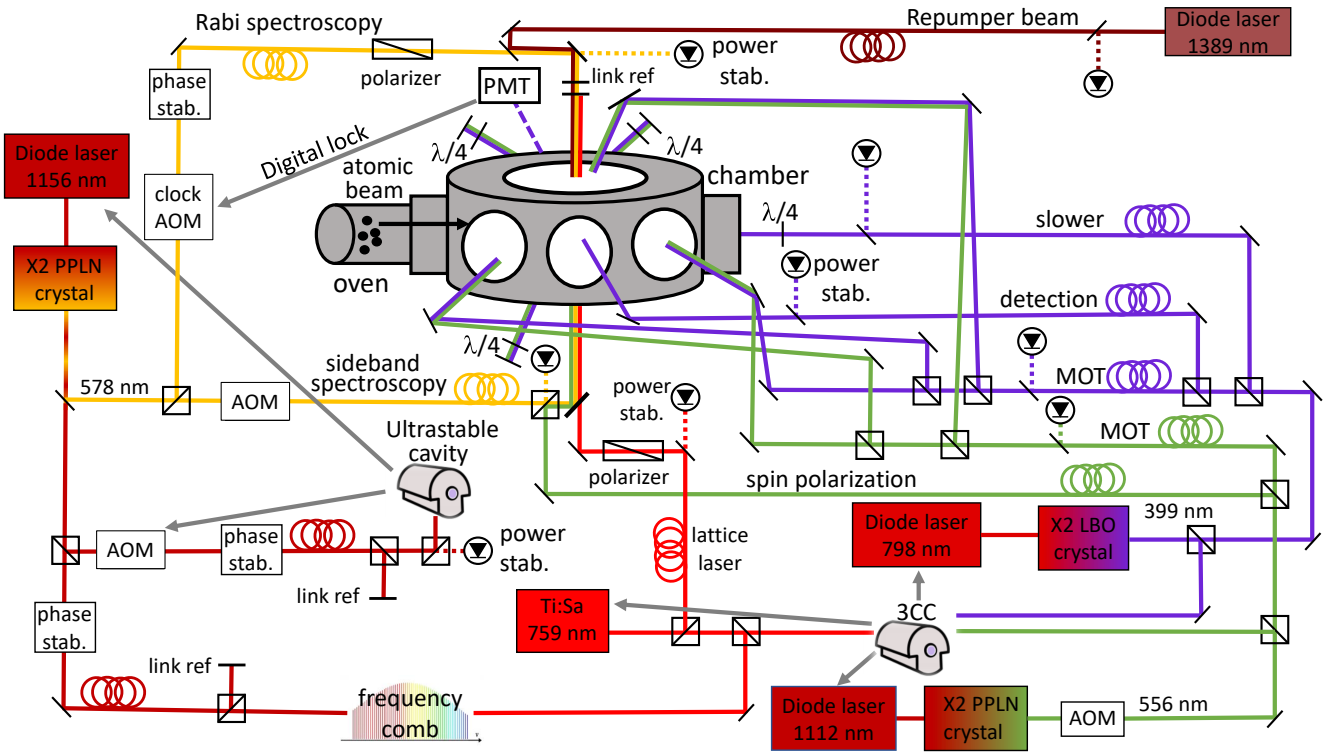

Fig. 2.2 Scheme of the experimental setup of IT-Yb1.The laser generations and their stabilization on two cavities are represented. All the laser beams are sent to the atomic chamber through polarization-maintaining optical fibers. Beam samplers labeled as "link ref" and photodiodes indicated as "power stab" represent the reference points for the fiber phase-noise cancellation and power stabilization. A photo-multiplier tube (PMT) collects the atomic fluorescence signal used to keep the clock laser resonant with the clock transition.

comb. The clock laser at 1156 nm is measured by the frequency comb as well. The frequency-doubled radiation at 578 nm is resonant to the Yb clock transition. It is split into two separate paths and sent to the atomic chamber to perform the Rabi spectroscopy and the sideband spectroscopy (Sec. 2.5.3).

Several mechanical shutters are placed along the optical paths to switch on and off the laser beams as needed to perform the different steps of the clock cycle.

The beam paths that directly contribute to the evaluation of the clock frequency, i.e., the Rabi spectroscopy beam and the 1156 nm beam paths headed to the ultrastable cavity and the optical comb, are provided with a fiber phase-noise cancellation system (Sec. 3.5). Their reference points are reported in Fig. 2.2 as "link ref". Before the interaction with the atoms, the power of all the laser beams is measured by a photodiode. Moreover, the detection, the lattice and the Rabi spectroscopy beams

are provided with a power stabilization system. After the clock interrogation, the excited atoms produce a fluorescence signal that is collected by a photo-multiplier tube (PMT).

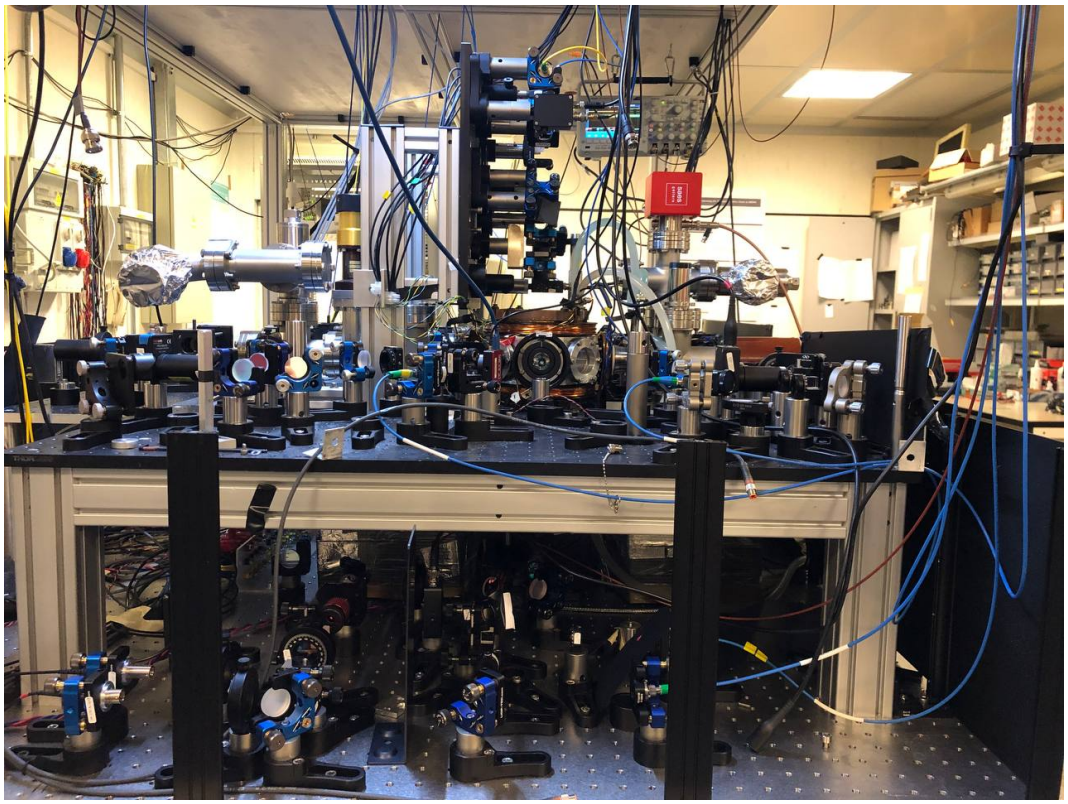

Fig. 2.3 Picture of the IT-Yb1 optical lattice clock at INRiM.

A picture of IT-Yb1 is shown in Figure 2.3. The image reports only the optical table that holds the atomic chamber.

2.2 Clock laser

2.2.1 Clock laser generation and preparation

The local oscillator of IT-Yb1 is a yellow laser beam at 578 nm that is generated through SHG process from a 1156 nm radiation. The infrared laser is a DL+TA pro (Toptica Photonics) with a maximum output power of almost 1 W. The SHG

occurs in a non-linear PPLN crystal connected to the seed laser via an optical fiber. Since the efficiency of the SHG process strongly depends on the non-linear crystal temperature, a controller (Thorlabs, TED200C) regulates the crystal temperature at a chosen working point. In typical working conditions, the non-linear crystal in single-pass configuration produces about 45 mW of yellow radiation, starting from an infrared seed power of 370 mW.

Figure 2.4 shows a scheme of the optical path for the preparation of both the 1156 nm and the 578 nm beams. After the frequency doubling process, a dichroic mirror

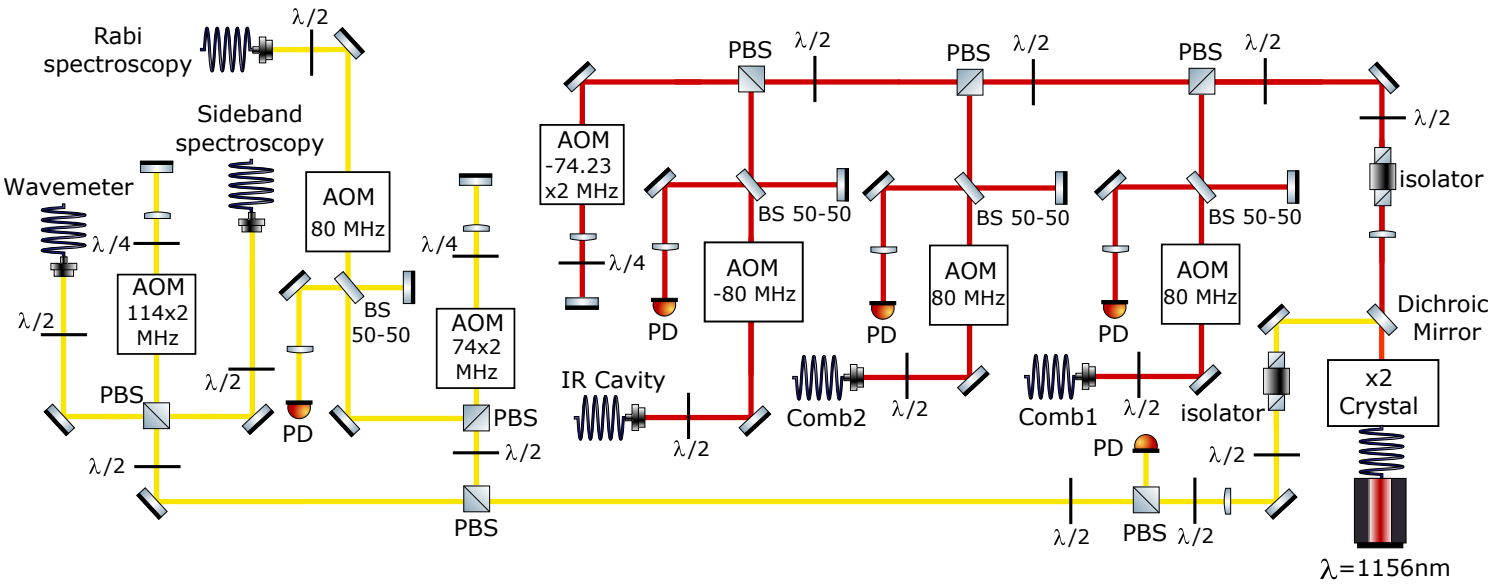

Fig. 2.4 Optical table for the preparation of the 1156 nm and the yellow 578 nm lasers. The scheme also reports the optical elements for the fiber phase noise stabilization.

separates the yellow radiation from the infrared one. The two laser beams pass through an isolator to avoid any possible damaging reflection from going back into the PPLN crystal. Several polarized beam splitters (PBS) divide the 1156 nm beam in three different paths, whose power is adjustable using a $\lambda/2$ waveplate in front of each PBS. Two optical paths are used to send the infrared radiation to two independent optical combs (comb1 and comb2 in Figure). The last 1156 nm beam double-passes an AOM and is sent to the ultrastable cavity described in the next Section.

Instead, the yellow beam is divided into two optical branches and is prepared for the atomic interrogations. In both cases, the beam frequency is properly tuned by a digitally controlled double-pass AOM. Then, the yellow beams are sent to the atomic

chamber through a polarization-maintaining optical fiber (OZ, QPMJ-3AF3AF-400) for the Rabi spectroscopy and the sideband spectroscopy (Sec. 2.5.3). The three infrared beams and the Rabi spectroscopy beam are provided with a fiber phase noise cancellation system, which I will describe in detail in Section 3.5.

2.2.2 Clock laser stabilization: ultrastable cavity

The DL+TA at 1156 nm utilized for the generation of the clock radiation is frequency stabilized on an ultrastable Fabry Pérot cavity with the PDH technique [72, 73]. The cavity is 10 cm long and is made of ULE (Ultra Low Expansion glass) and silica mirrors. The mirrors are provided with an antireflection coating at 1156 nm. A picture of the IT-Yb1 cavity is shown in Fig 2.5. The cavity is mounted on a glass support and is located inside a vacuum chamber designed and provided by Stable Laser System. The picture on the right side of Figure 2.5 shows the vacuum cham-

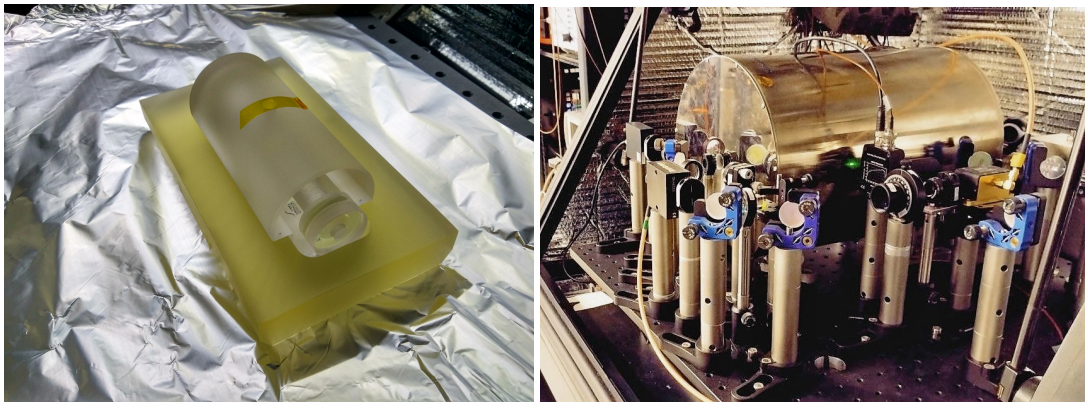

Fig. 2.5 IT-Yb1 ultrastable clock cavity. Left: picture of the cavity placed on its glass support. Right: picture of the vacuum chamber containing the cavity. In this image, you can also see the optical setup for the cavity stabilization and the acoustic enclosure.

ber that hosts the cavity. The temperature inside the chamber is controlled thanks to two thermal shields, both provided with heaters and temperature sensors. The internal thermal shield has been used to determine the zero-CTE (thermal expansion coefficient) point, that is 28.25 °C for this cavity. Therefore, the temperature of the vacuum chamber is stabilized at this value.
From the cavity ringdown time, the evaluation of the cavity linewidth results to be γ=2.0 kHz. Since the free spectral range (FSR) for a 10 cm long cavity is 1.5 GHz, it is thus possible to calculate the finesse F of the cavity as $F = FSR/\gamma = 750000$

and its quality factor $Q = 1.3 \times 10^{11}$.
The cavity and the optical setup that provides the frequency stabilization are mounted on a breadboard on top of an active vibration isolation platform (DVIA-T45) manufactured by Daeil Systems. The whole apparatus of the cavity is contained in an acoustic enclosure system (HERZAN, AEK-2002).
When the optical clock is running following the sequence described in Section 2.5, it is possible to estimate the instability of the cavity by considering the clock in-loop frequency corrections applied on the clock AOM (see figure 2.2) to make the clock laser resonant to the atomic frequency reference. Figure 2.6 shows the instability as an Overlapping Allan deviation. The cavity drift is compensated by an additional

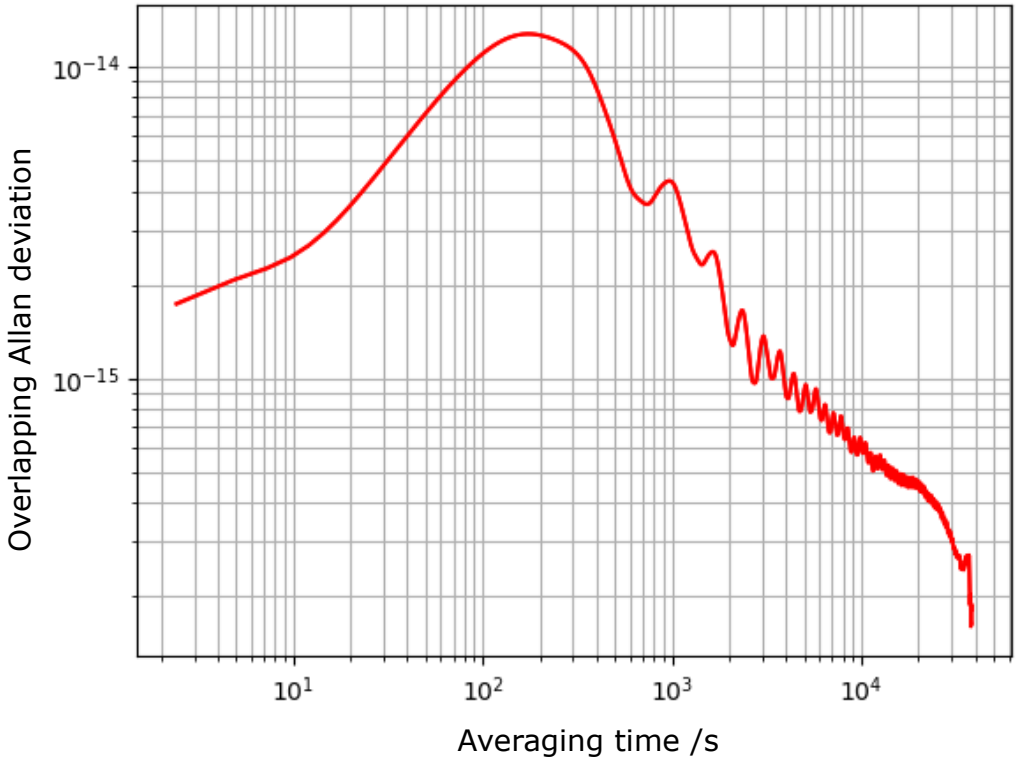

Fig. 2.6 Overlapping Allan deviation of the IT-Yb1 local oscillator evaluated through the frequency corrections applied to the clock AOM. The drift of the cavity is compensated by locking the clock to an H-maser.

digital lock on an H-maser via an optical frequency comb. For small averaging times, the signal is dominated by the stability of the cavity. Therefore, from Figure 2.6, it is possible to attribute to the cavity a flicker floor lower than $2 \times 10^{-15}\,(\tau/s)^0$. The instability then worsens at longer averaging times due to the long-term noise of the

cavity. Finally, starting from about 200 s of averaging time, the H-maser stability dominates and compensates for the cavity drift.

2.3 Laser for atomic manipulation

2.3.1 Blue 399 nm laser

Light generation

As schematically illustrated in Fig. 2.2, the laser beam at 399 nm is obtained from a laser source at 798 nm which is frequency doubled via the second harmonic generation process (SHG) [74] in a non-linear lithium triborate crystal (LBO). The laser source is a diode laser injected in a tapered amplifier (DL+TA pro) produced by TOPTICA Photonics. The maximum power generated by the 798 nm TA laser is

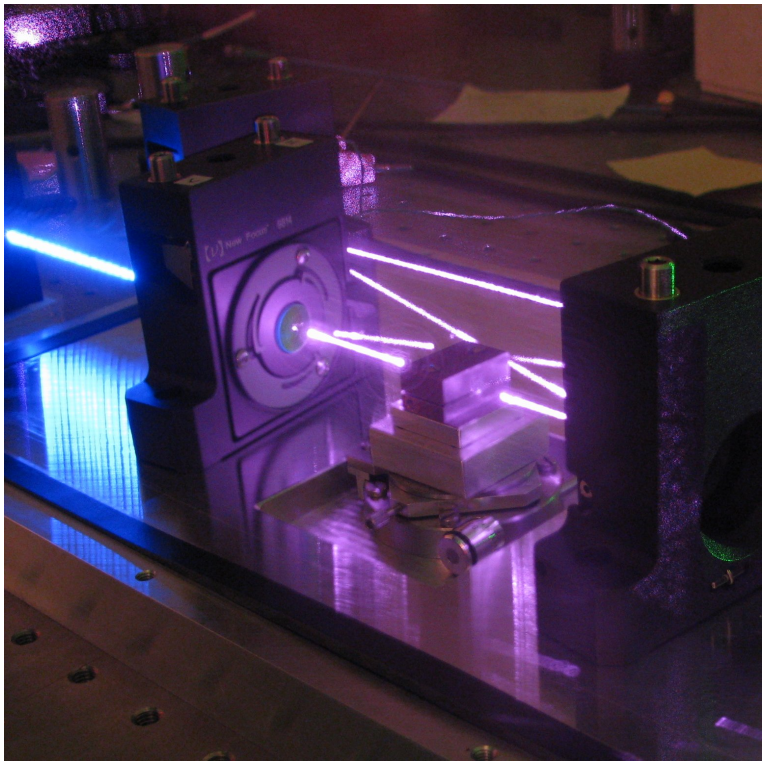

Fig. 2.7 Cavity for second harmonic generation, adapted from [75]. The mirrors forming the cavity form a bow-tie configuration. The non-linear crystal is observable between the mirrors.

2.7 W but usually, it operates at 2.25 W to not deteriorate the laser and guarantees a constant performance. Typically DL+TA lasers generate a slightly elliptical beam, whose mode is cleaned to a TE00 mode by coupling the laser beam to an optical fiber. The coupling efficiency is about 50%.
The cavity for the SHG process is shown in Fig. 2.7. The 399 nm enhancement cavity has a bow-tie configuration [75], and the maximum output power is 300 mW with a typical input power of 1.1 W. One mirror forming the duplication cavity is assembled on a piezo for frequency tuning, and the blue light is frequency locked using the Hänsch-Couillaud technique [76]. Furthermore, we recently implemented an automatic relock system which consists of a PID controlled by an Arduino board. A photodiode placed just after the cavity collects the optical signal for the relock. After digitally optimizing the locking parameters, the typical automatic relock time is about 5 s.

Laser beam preparation

Fig. 2.8 shows a schematic of the optical table for the generation and the preparation of the blue radiation. Before being amplified by the TA, a small fraction of the 798 nm laser is sent to the 3-colors cavity (see Section 2.3.5). The beam emitted by the TA laser is split, and a little fraction of power is sent to a multichannel wavemeter (Bristol 871 wavelength + Bristol fiber optic switch APC). After the generation of the blue radiation, the beam is split into three different optical paths for the slower, the MOT and the detection procedures. Each optical path is provided with an acoustic-optic modulator (AOM) for frequency tuning. The AOMs combined with a mechanical shutter digitally control the loading sequence and prevent MOT or slower beams from perturbing the detection process. All the laser beams are then collimated with a telescope to maximize the fiber coupling efficiency, which is about 60%. The blue radiations are sent via optical fiber (OZ QPMJ3AF3AF or Schäfter+Kirchhoff PMC-E-400-APC) to the optical table that hosts the atomic chamber (see Fig. 2.2). Both the slower beam and the first MOT are produced starting from a laser beam resonant to the $^1S_0 \rightarrow {}^1P_1$ transition at 399 nm (see Fig 2.1).

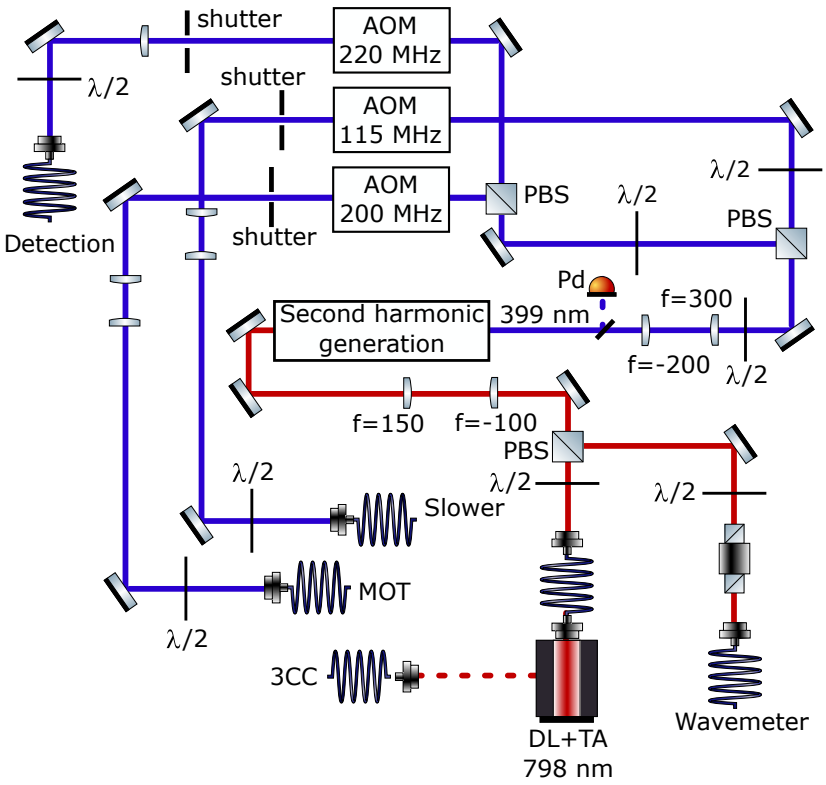

Fig. 2.8 Schematic of the optical table for the generation and the preparation of the blue radiation at 399 nm.

2.3.2 Green 556 nm laser

Light generation

The green light is generated from a 1112 nm laser through SHG in a non-linear periodically poled lithium niobate (PPLN) crystal. The 1112 nm light, as for the 798 nm, is obtained with a DL+TA pro laser manufactured by TOPTICA Photonics. Before the amplification, a small portion of the light emitted by the diode laser is picked up and sent to the multichannel wavemeter. The laser light is coupled to an OZ optical fiber that is directly plugged into the pigtail input fiber of the crystal. The maximum power attainable before the OZ fiber is 1 W. To not degrade the laser performance and to not overcome the maximum input power for the crystal (500 mW), in the operation conditions, the TA current is not maximized. The frequency doubling is performed in a single pass. As the efficiency of the duplication process strongly depends on the crystal temperature, the PPLN crystal is provided with a temperature

controller (Thorlabs, TED200C). In the operation condition, the TA output power is about 350 mW, and the input power in the PPLN crystal is 200 mW. After the SHG, we obtain 15 mW of green light at 556 nm. We note that one of the main limiting factors in this SHG process is the low coupling efficiency between the OZ-AFC fiber and the APC pigtail of the crystal.

Laser beam preparation

The optical setup for the green light beam preparation is illustrated in Fig. 2.9. Before the amplification, a portion of the infrared radiation at 1112 nm emitted by

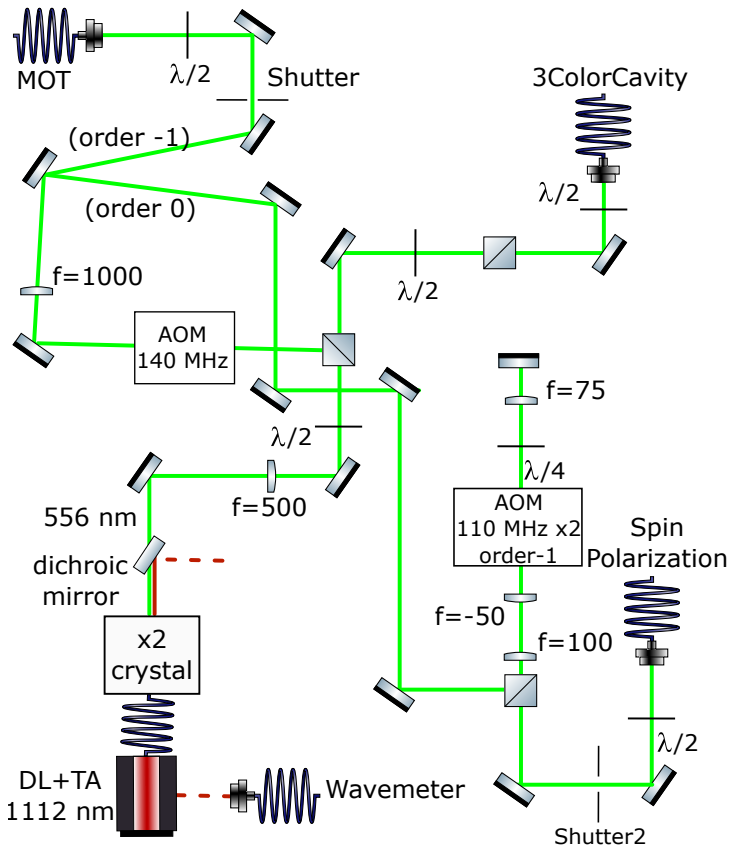

Fig. 2.9 Scheme of the optical table for the generation and the preparation of the green radiation at 556 nm.

the DL is picked up and sent to the multichannel wavemeter. After the SHG, the green light is split on a polarized beam splitter. The transmitted beam is sent via

optical fiber to the 3-colors cavity (see Section 2.3.5). The reflected beam instead enters an AOM. The AOM order -1 is sent to the atomic table to generate the MOT. The order 0 of the AOM double-passes through another AOM and then is sent to the atoms to spin-polarize them (see Section 2.5.2). As for the blue optical setup, also in this scheme the AOMs are utilized as fast switches to control the action times of each laser beam, while the shutters ensure the complete extinction of the beams when they are not needed. The green light for the MOT and the spin polarization is sent to the science chamber (see Fig. 2.2) via optical OZ fiber (QPMJ-3AF-3AF). The typical coupling efficiency is about 75%.
The radiation at 556 nm, resonant with the atomic transition $^1S_0 \rightarrow {}^3P_1$, is employed for the second MOT stage and for preparing the atomic sample (Sec. 2.5.2) in a specific sublevel of the ground state $m_F = \pm 1/2$ (see Fig. 2.1).

2.3.3 Lattice 759 nm laser

The lattice radiation is generated by a commercial Ti:Sa laser (SolsTiS, M squared) pumped with a solid-state laser (Sprout, Lighthouse Photonics) that provides 10 W of 532 nm light. The maximum output power at 759 nm is about 2.4 W.
The lattice laser beam follows the optical path schematized in Fig. 2.10. An optical

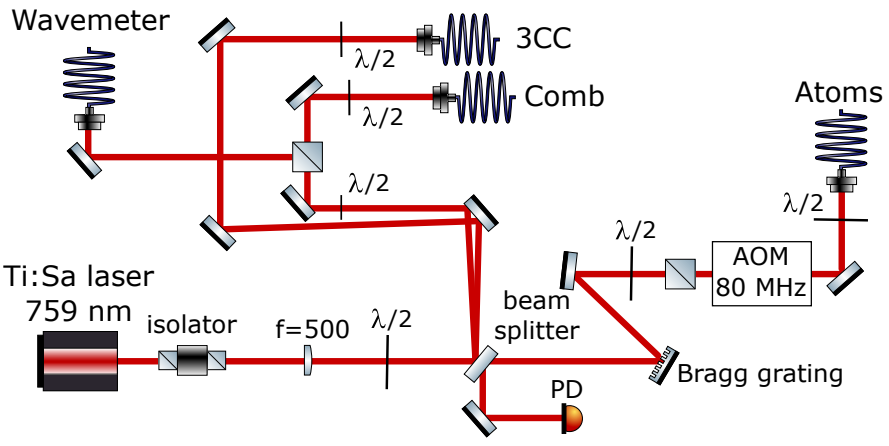

Fig. 2.10 Optical setup for the generation of the lattice radiation.

isolator prevents any potentially damaging reflection from coming back into the laser. A beam splitter produces two reflection beams (one for each surface of the splitter) that are used to send a fraction of the red radiation to the wavemeter, the comb and the 3-colors cavity. As detailed in Section 3.3, it is crucial that a comb continuously

measures the frequency of the 759 nm laser. Indeed, if the lattice does not operate at the magic wavelength, it introduces a relevant shift in the clock transition. Almost all the power of the red beam follows the optical path that leads to the atomic chamber, through an optical fiber (Schäfter+Kirchhoff PMC-E780-APC). The beam mode is filtered at the magic wavelength by a volume Bragg grating (Optigrate TOPBF759 42661-3) with a bandwidth of 20 GHz. The grating also ensures a good spectral purity by filtering possible amplified spontaneous emission (ASE) from the laser that may degrade the accuracy of the clock [77]. The optical fiber is aligned on the zero order of the AOM, which acts as a fast power control. A photodetector (PD) measures the power of the retroreflected lattice beam, thus indicating the goodness of the lattice alignment.

2.3.4 Repumper 1388 nm laser

The radiation at 1389 nm used for the repumper procedure, is generated by a pigtail-distributed feedback diode laser (NKT). Since the repumper laser is not frequency stabilized, we send to the atoms a power of about 2.5 mW to power broaden the transition and to increase the efficiency of the repumper process.

2.3.5 Frequency stabilization: 3-colors cavity

As schematically illustrated in Fig. 2.2, the three lasers at 399 nm, 556 nm and 759 nm are frequency locked on the same multi-wavelength Fabry-Pérot cavity. Since the mirrors forming this cavity are provided with a coating for the three different radiations, we refer to this cavity as "3-colors cavity" (3CC). A detailed description of this cavity can be found in [78], and the setup used for the stabilization of the lasers on the 3CC is schematized in Fig. 2.11.
The lasers are locked through a method similar to the well-known PDH technique: the offset-sideband locking technique [79]. The 3CC is a 10 cm long multi-wavelength Fabry-Pérot cavity, manufactured by Advanced Thin Films, made of silica mirror and ULE spacer. The cavity FSR is 10 GHz. The 3CC is contained in a vacuum housing kept at a pressure of 6×10^{-8} mbar by an ion pump. The cavity is provided with an active temperature control system that maintains the temperature at the zero-CTE point. Despite the fact that the 399 nm light can be directly stabilized on the cavity, it introduces a significant drift from absorption in the mirrors. It is thus preferable

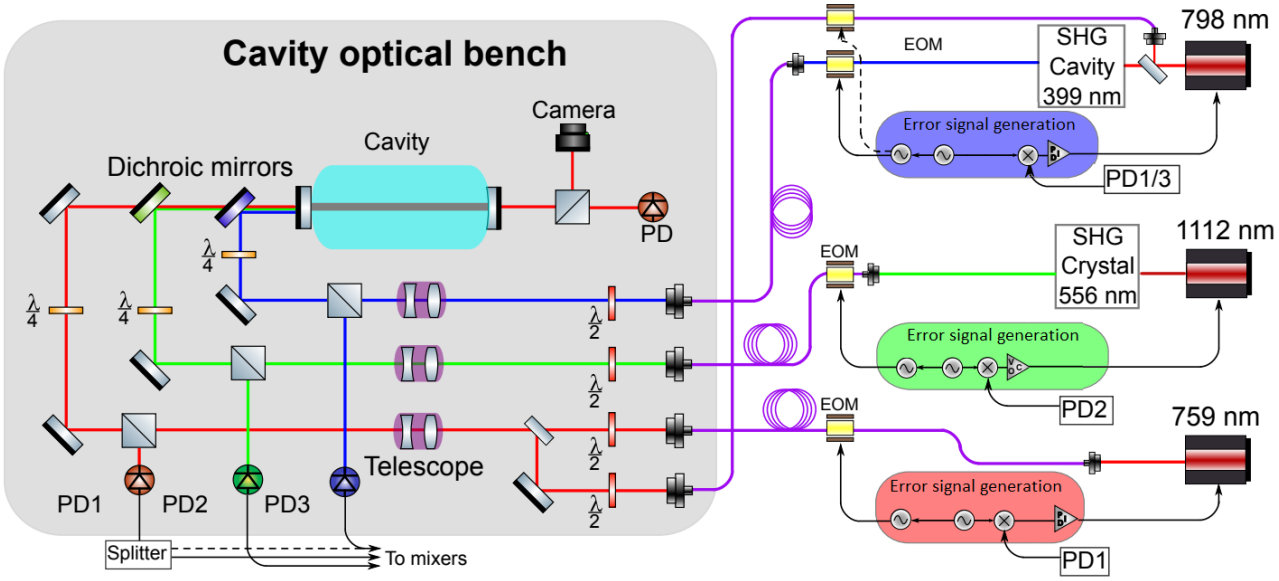

Fig. 2.11 Optical setup of the 3CC, adapted from [78]. The radiation at 399 nm can be directly stabilized to the cavity. However, in this case, the 3CC drift hugely increases, and it is thus preferable to stabilize the radiation at 798 nm. In the scheme, both alternatives are shown.

to stabilize the radiation at 798 nm, as shown in Fig. 2.8. Three photodiodes (PD) measure the light power reflected by the cavity. Each laser is modulated at a different frequency, and the PD signals are filtered by narrow band-pass filters, to distinguish among the different wavelengths. The signal error used to lock each laser frequency is generated starting from the PD signal.

To produce an efficient MOT, it is necessary to have a daily frequency drift of less than 1 MHz and 100 kHz for the blue and green lasers, respectively. Moreover, the daily lattice frequency drift must be less than 120 kHz to keep the lattice shift less than 1×10^{-18} (more details in Section 3.3). When all the lasers are locked to the 3CC, we can observe a linewidth of 300 Hz for the 556 nm radiation, which is the most limiting requirement. Additionally, when all the lasers are locked, the observed drift is less than 2 kHz/h.

2.4 Physical package

A solid sample of Yb atoms sublimates into an atomic oven at a temperature of about 390 °C and gaseous atoms are emitted in a collimated beam. The picture on the left

side of Fig. 2.12 shows the oven currently utilized in our experiment. It is a custom

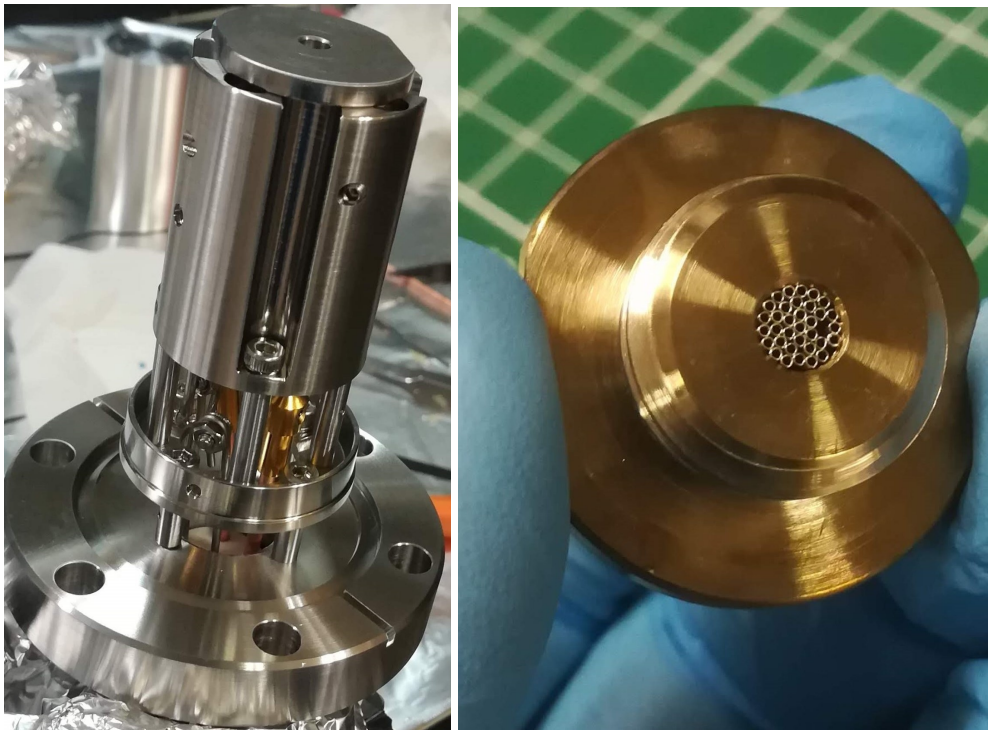

Fig. 2.12 IT-Yb1 new oven. Left: picture of the oven. The crucible mounted on a flange ConFlat CF40 is visible. Right: picture of the oven nozzle and the capillaries.

system implemented in 2020, more recent compared to that described in [78], and similar to the apparatus described in [80, 81]. The oven consists of a reservoir of about 7 cm^3, filled with solid Yb. Two cartridge heaters maintain the sublimation temperature, and a thermocouple records the oven temperature. The reservoir is connected to a nozzle of diameter $d = 4.1$ mm which is filled with 37 capillaries made of stainless steel. The capillaries are 11 mm long and have an internal diameter of 400 μm. The picture on the right side of Fig. 2.12 shows the nozzle and the capillaries. The reservoir and the nozzle are placed into a crucible made of stainless steel provided with a polished aluminum shield. The crucible is mounted on a flange ConFlat CF40 (left image of Fig. 2.12).

The whole IT-Yb1 vacuum system is illustrated in Figure 2.13. A vacuum differential tube inserted in a ceramic support connects the oven to the science chamber [82]. The atoms travel a distance of about 20 cm to reach the atomic chamber. This distance is as small as possible to maximize the flux of atoms toward the trapping region.

The proximity of the science chamber to the oven makes the use of a slower beam enough to trap the Yb atoms without the necessity to implement the Zeeman slower technique [83, 84].
Two ion pumps (Agilent VacIon 40 and Saes NexTorr HV 100) maintain the ultra-high vacuum in the science and the oven region, respectively. The Saes pump is provided with a Non-Evaporable Getter (NEG). With this apparatus, the vacuum level in the trapping region is about 10^{-9}mbar, which is enough to ensure an adequate lifetime of the atoms in the lattice. The science chamber is an aluminum

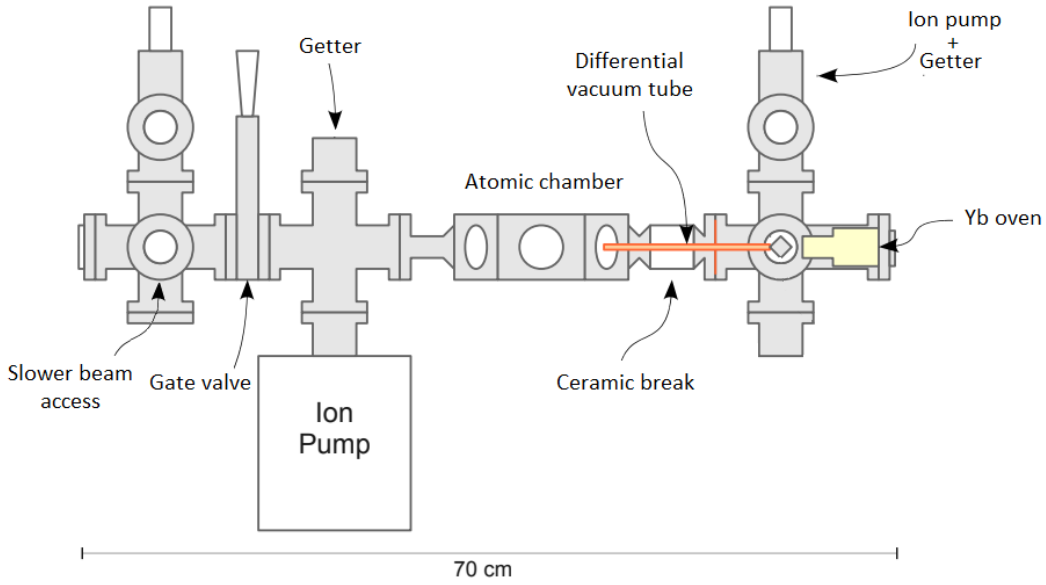

Fig. 2.13 Scheme of the vacuum system of IT-Yb1. The image is adapted from [82]

octagonal-shaped structure provided with silica windows to allow optical access, sealed with an indium wire. The indium seal can be closed with low retaining force, reducing the induced birefringence in the glass. The six lateral (x-y horizontal plane) windows have a diameter of 40 mm, while the two windows along the vertical direction (z-axis) have a diameter of 70 mm. All the windows have a dielectric anti-reflection coating at the relevant wavelength utilized in the experiment. Ten resistance thermometers are distributed all over the aluminum skeleton to monitor the temperature of the atomic chamber and evaluate the consequent blackbody radiation effect.
The atomic beam emitted by the oven is slowed down by a counter-propagating blue slower beam resonant with the $^1S_0 \rightarrow {}^1P_1$ transition. The slower beam accesses the vacuum chamber from a lateral viewport and is reflected against the atoms with

a 45° mirror. It is necessary to periodically replace the 45° mirror because of the deposition of material emitted by the oven. To facilitate this operation, a gate valve is located between the science chamber and the intra-vacuum mirror (see Figure 2.13). It is thus possible to replace the mirror while maintaining the vacuum pressure in the science chamber.
The magnetic gradient for the implementation of the MOT is generated by two magnetic coils in the anti-Helmholtz configuration. The coils are arrayed on the science chamber with the axis along the vertical direction and are rolled around an aluminum support with a hollow core for water cooling. A water-cooling chiller is used to adjust the temperature of the atomic chamber, which may increase during the experiment because of the overheating of the coils. Moreover, three pairs of coils in Helmholtz configuration are used to compensate eventual stray magnetic field in correspondence with the trapping region. The compensation coils are rolled around the chamber viewport.

2.5 Clock sequence

The typical clock sequence of IT-Yb1 is represented in Fig. 2.14.
The different phases of the cycle are indicated at the top of the scheme, and the corresponding letters coincide with the ones used in the previous chapter in Fig. 1.5 to describe the typical lattice clock cycle.
During the whole cycle that lasts about 300 ms, the lattice radiation always interacts with the atoms. The sequence is as short as possible to reduce the instability of the clock due to both the quantum projection noise and the Dick effect (see Sec. 1.2). Let's see the details of each phase of the IT-Yb1 clock sequence.

2.5.1 Experimental implementation of cooling and trapping techniques

The performance of an optical clock improves as the number of interrogated atoms increases. It is thus necessary to trap a large number of atoms in the optical lattice. For this reason, Yb atoms are first slowed down and trapped in a two-stage Magneto-Optical Trap (MOT) to increase the lattice loading efficiency.

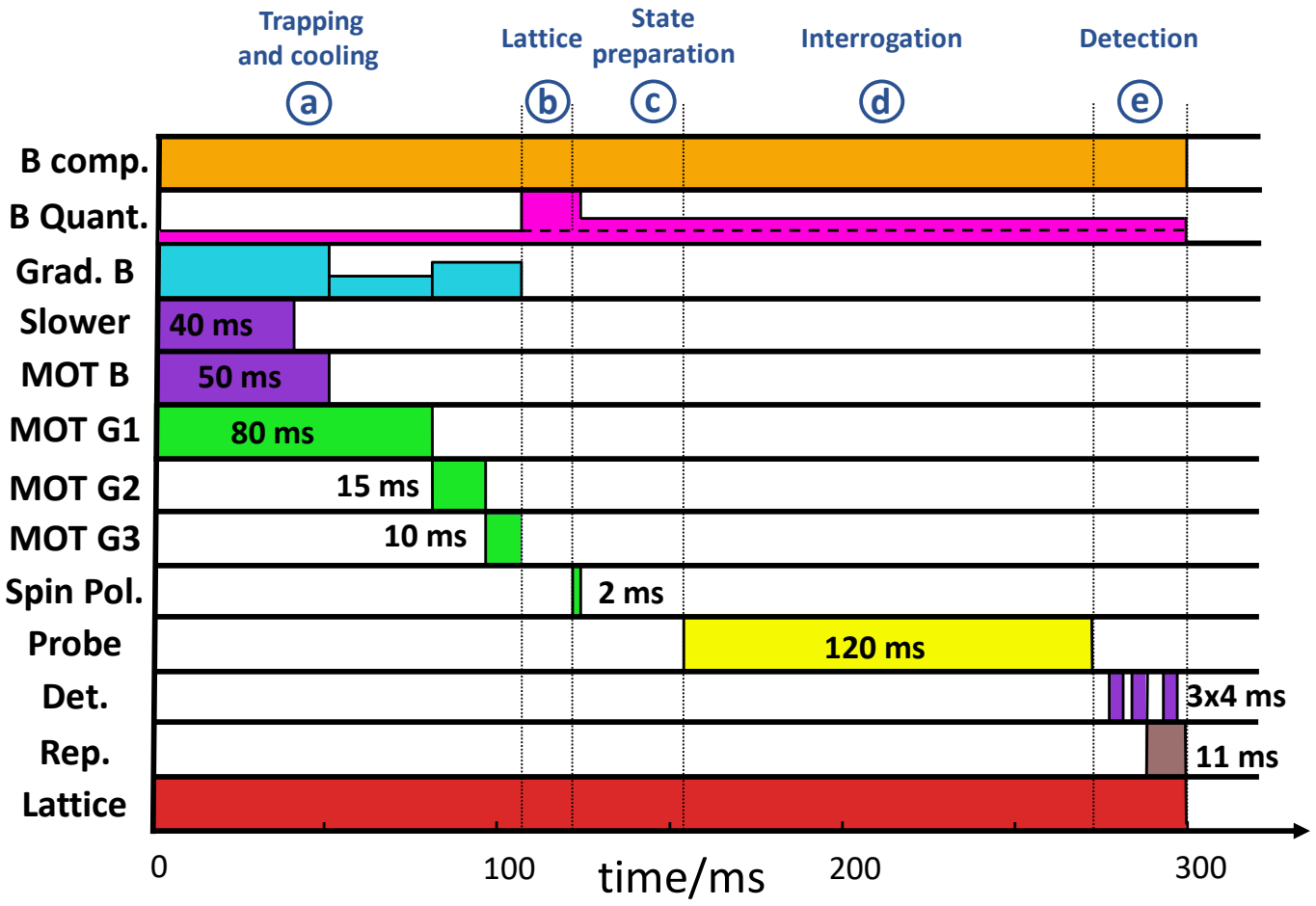

Fig. 2.14 IT-Yb1 cycle sequence. The magnetic fields and the laser radiations are represented with different colors, and the duration of each stage is indicated. The whole clock cycle lasts 300 ms, and the lattice is always present throughout the cycle. The details of the different stages are described in the following sections.

Laser cooling and trapping techniques rely on the interaction between the laser light and the atoms, from which derive the dipole force and the radiation pressure force, which are at the basis of the confinement in the lattice and the MOT, respectively. The theory of laser cooling and trapping is found in many remarkable textbooks [85, 86] and papers [87–90], as well as master and Ph.D. theses [78, 91].

Slower

A slower beam at 399 nm propagates against the atomic beam emitted by the oven.

In correspondence with the center of the atomic chamber, the slower beam interacts with the atoms and slows them down thanks to the radiation pressure [85]. The typical slower beam power we measure before the atomic chamber is 35 mW, and the $1/e^2$ radius beam is about 1 cm. The polarization is circular thanks to a $\lambda/4$ waveplate, and the beam is frequency detuned of -360 MHz to the atomic transition. This high detuning is chosen to compensate for the Doppler effect of rapid atoms and to guarantee a more efficient cooling process [85]. In our experiment, we do not use a Zeeman slower technique, which combines the action of the slower beam with a magnetic field that keeps the atoms resonant with the laser beam during the process of slowing down. However, the magnetic field generated by the MOT coils extends slightly outside the atomic chamber and can be used to increase the effect of the slower beam. The efficacy of the slower beam depends on the loading time. Typically, the slower pulse is 40 ms long, as detailed in Fig. 2.14, and it improves the loading of atoms in the MOT of a factor 6.

Blue MOT

The optical setup for the MOT is simplified and reported in Figure 2.2: three pairs of retroreflected beams, orthogonal to each other, interact with the atomic sample in the center of the chamber. The two beams of each couple have opposite circular polarization σ_+ and σ_-. The polarization of the beams is adjusted with two waveplates $\lambda/4$, placed just before and after the atomic chamber. The three beams for the first MOT stage at 399 nm have altogether a power of about 35 mW and are red-detuned of 20 MHz to the $^1S_0 \rightarrow {}^1P_1$ transition. The blue collimated beams have $1/e^2$ radius of about 1 cm, and usually are switched on for $\sim$50 ms (Fig. 2.14). The magnetic gradient to implement the MOT technique is generated by the coils described in Section 2.4. A digitally-controlled power supply (TDK-LambdaGEN1U-1500W) pilots the current flowing in the coils according to the magnetic field value that is needed at each stage of the cycle (sky blue rectangles in Fig. 2.14). For the blue MOT, the magnetic field gradient is $0.35\,\mathrm{T/m}$.
The lowest atomic temperature attainable with the MOT technique is the Doppler temperature [87]: $k_B T_D = \frac{\hbar\Gamma}{2}$, where k_B is the Boltzmann constant. Since in our experiment, the first MOT stage exploits the blue transition that has a linewidth $\Gamma/2\pi$ of 29 MHz (see Fig. 2.1), the corresponding Doppler temperature is $T_D^{blue} = 700\,\mu$K. After implementing and optimizing the blue MOT stage, a Yb sample of 2×10^5

atoms is trapped at a measured temperature of about 1 mK.

Green MOT

The second green MOT stage exploits the $^1S_0 \rightarrow {}^3P_1$ transition. The three green MOT beams are overlapped with the blue MOT optical paths before entering the atomic chamber. The overall green power is 2 mW, and the beam $1/e^2$ radius is 0.5 cm. As shown in Fig. 2.14, the green MOT procedure consists of three stages, during which the detuning and intensity vary concordantly with the magnetic field gradient. The green radiation is switched on together with the blue radiation, and the entire green MOT lasts 55 ms from when the blue MOT is switched off. The first green stages maximize the transfer from the blue MOT, which has an efficiency of about 70%. During the second stage, the detuning and the intensity of the laser beam decrease to reduce the atomic temperature up to $\sim 10\,\mu K$. The parameters of the third stage are chosen to maximize the atomic loading in the optical lattice.
Having the green transition a linewidth of 182 kHz (see Fig. 2.1), the corresponding Doppler temperature is about $T_D^{green} = 3\,\mu$K.
At the end of the second MOT stage, the blue and the green lasers are switched off, as well as the magnetic field used to generate the MOT. The atoms remain trapped in the optical lattice, which is always present during the clock sequence (see Fig. 2.14).

Optical lattice

The optical lattice is produced by combining the action of two counterpropagating, very out-of-resonance, red-detuned beams. Indeed, the interference between the beams results in a standing wave with spatially modulated intensity along the propagation axis of the lasers. The potential generated by the laser is proportional to the intensity and attractive for red-detuned radiation [90]. As a consequence, the atoms are subject to a periodic potential, that, in correspondence with the lattice minima, can be approximated as harmonic. In this case, for an atom with mass m and a Gaussian beam with wavelength λ_L and waist w_0 that propagates along $\hat{z}$, the axial and the radial trap frequencies are [90] $\omega_z = \frac{\lambda_L}{\pi w_0^2}\sqrt{\frac{2U_0}{m}}$ and $\omega_r = \sqrt{\frac{4U_0}{m w_0^2}}$. U_0 is the trap depth and usually it is expressed in units of energy recoil E_r, which represents the energy gained by a Yb atom that absorbs a lattice photon and is given by $E_r = \frac{\hbar^2 \omega_L^2}{2 m_{\mathrm{Yb}} c^2} = \hbar \times 12.7\,$kHz.

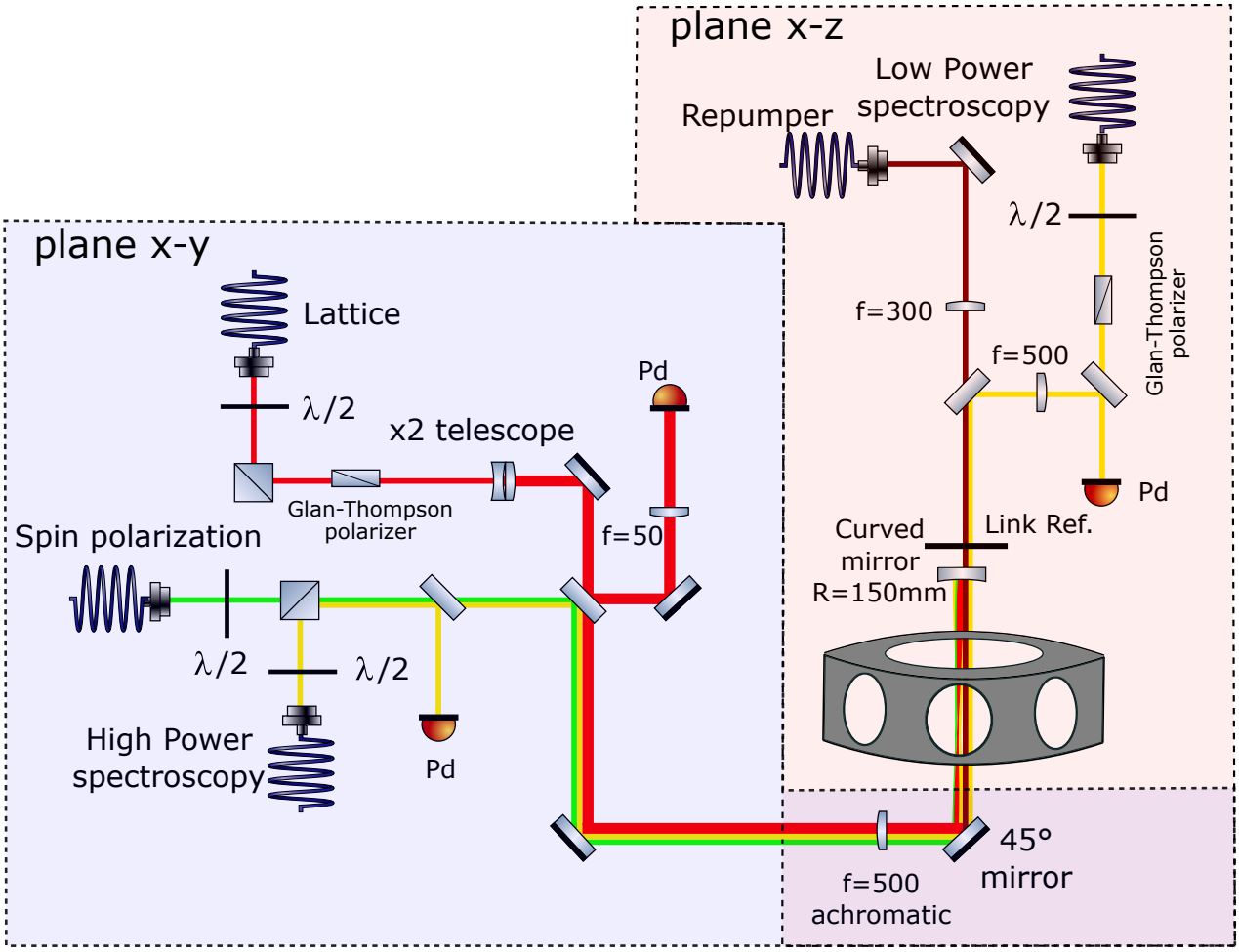

Fig. 2.15 Optical setup for the vertical lattice. The orange-shaded area is the setup portion built on the vertical breadboard. The setup on the optical table in the horizontal (x-y) plane is represented as a violet-shaded area. The optical elements used to produce the vertical beam of the MOT are not reported. In this scheme are also shown the optical paths of the spin-polarization, the repumper, and the two probe beams used for the spectroscopy procedures. Additionally, the reference for the link used to eliminate the fiber phase noise of the Rabi spectroscopy beam is reported, as well as the photodetector (Pd in the scheme) of the Rabi spectroscopy that measures the optical signal for power control.

The lattice path on the optical table that hosts the atomic chamber is shown in Fig. 2.15. This is an upgraded optical setup with a vertical lattice, which we implemented during my Ph.D. The new apparatus allows us to have a vertical optical lattice instead of the horizontal one that was used in the past [68, 92, 71]. The orange-shaded area in Fig. 2.15 represents the optical setup built on a vertical breadboard

(plane x-z). On the contrary, the violet-shaded area is the setup built on the horizontal optical table (x-y plane).
By having the strong axis of the trap contrasting the gravity, a lower lattice power is enough to efficiently trap the atoms. This leads to several benefits in terms of uncertainty budget, as we will discuss in detail in the next Chapter.

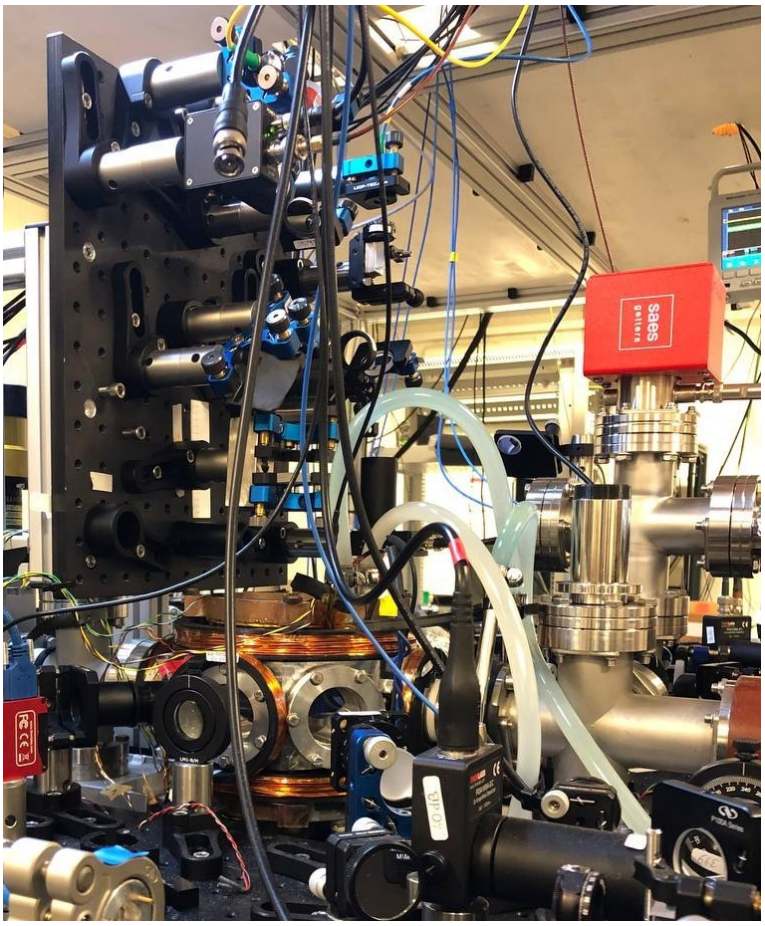

Fig. 2.16 Picture of the vertical lattice setup.

The maximum lattice output power measured after the optical fiber is $P = 1.2\,\mathrm{W}$. The lattice beam is collimated by a SuK collimator (60FC-4-A15-02), and its polarization is cleaned by a Glan-Thompson polarizer. Then, the beam $1/e^2$ radius is doubled by a Thorlabs telescope (GBE02-B-2X) up to $\sim$10 mm. Before being combined with the other beams on a dichroic mirror (Thorlabs DMLP650), a pickup beam is measured by a photodetector to control the power. The beam is then focused on the atomic chamber by an achromatic lens with $f = 500\,\mathrm{mm}$ (Thorlabs LFL100-100)

and a silver mirror placed at 45° to orientate the lattice along the vertical direction. The lattice beam is retro-reflected by a concave mirror. The resulting beam waist in correspondence with the MOT center is 45 μm, and the typical power of the incoming beam measured just before the 45° mirror is 1 W. Consequently, the optical lattice has a maximum depth of about 600 E_r. At the end of the loading sequence, we managed to trap up to 10^4 atoms at a temperature of a few μK.
A picture of the vertical breadboard is shown in Fig. 2.16.

2.5.2 State preparation

Once Yb atoms are loaded in the optical lattice, a 556 nm pulse optically pumps them into a single sublevel of the ground state $\left|{}^1S_0, m_F = \pm 1/2\right\rangle$ (see Fig. 2.1). This procedure is called "spin polarization" or "state preparation". For the correct operation of the optical clock, this step is crucial. Indeed, a non-balanced atomic distribution between the two Zeeman sublevels $m_F = \pm 1/2$ leads to an asymmetric line shape, that can broaden in the presence of a non-zero magnetic field. In addition, it is important to note that the spin polarization process also reduces the clock frequency shift due to the line-pulling effect and the atomic collisions, which are suppressed for fermionic atoms in identical states (see detail in Section 3.12).
To implement the spin polarization process, a bias magnetic field is applied through a couple of compensation coils on the horizontal plane to break the degeneracy of the m_F substate. This magnetic field defines the quantization axis and is represented in Fig. 2.14 as the pink big rectangular labeled "B Quant.". The applied field is 0.03 mT, big enough to make the separation of the Zeeman sublevels larger than the clock transition linewidth.
The preparation of the spin polarization beam is shown in Fig. 2.9: the laser double-passes an AOM and, by changing its frequency, transitions starting from different sublevels $\left(\left|{}^1S_0, m_F = \pm 1/2\right\rangle \rightarrow \left|{}^3P_1\right\rangle\right)$ are excited. In this way, by appropriately choosing the light polarization, atoms can be optically pumped in the Zeeman sublevel that is not resonant with the spin-polarization radiation [71].
The beam path of the spin polarization radiation toward the atomic chamber is described in Fig. 2.15. In the trapping region, the spin polarization beam propagates along the vertical direction, and it is aligned with the axis of the bias magnetic field. The power of the green laser after the fiber is about 5 μW. After a spin polarization pulse of 2 ms (see Fig. 2.14), 98% of the atoms are in the desired sublevel and the

atomic sample is ready to be interrogated by the clock laser. Before sending the clock pulse, it is crucial to wait a time long enough to ensure that the magnetic field used for the atomic cooling and trapping decays. As illustrated in Fig. 2.14, in our experiment, we wait for 30 ms before starting the interrogation process. However, a small magnetic field is still present during the interrogation and the detection processes (represented in pink in Figure 2.14) to have a defined quantization axis and select only the π transitions. In addition, during the whole clock sequence, the bias magnetic field along the three spatial directions is set to constant values through the compensation coils (see Section 2.4), to compensate for any residual magnetic field. The compensation fields are represented in Figure 2.14 as the constant pink rectangular bordered with the dashed line and the orange rectangular labeled "B Comp." for the direction orthogonal to the quantization axis. The three components of the compensation magnetic field are periodically (about every month) checked and when necessary adjusted to properly suppress the σ transitions.

2.5.3 Atomic interrogation

The clock interrogation occurs by applying a yellow pulse of 578 nm wavelength: the local oscillator of a Yb clock. In our experiment, two different spectroscopic techniques are implemented to measure the clock transition frequency: the Rabi spectroscopy and the sidebands spectroscopy.
In both cases, the radiations used for the interrogation are prepared as shown in Fig. 2.4 and, once on the atomic breadboard, follow the optical path represented in Fig. 2.15. To guarantee the Lamb-Dicke regime (described in more detail below) the probe pulse must propagate along the lattice axis. The sidebands spectroscopy beam is delivered to the atomic chamber from the bottom window, while the Rabi spectroscopy beam arrives from the top window. The power of the two radiations is controlled on a photodetector, and the Rabi spectroscopy beam is provided with a power stabilization system. The beam polarization of the Rabi pulse is made linear by a Glan-Thompson polarizer and aligned along the quantization axis, as well as the lattice beam. This way, the interrogation pulse induces only the π transitions ($\Delta m_F = 0$) and suppresses the σ transitions.

Spectroscopic techniques

Rabi spectroscopy

During the clock operation, the clock transition is interrogated using the Rabi spectroscopy. The Rabi spectroscopy is a well-known technique used to measure the

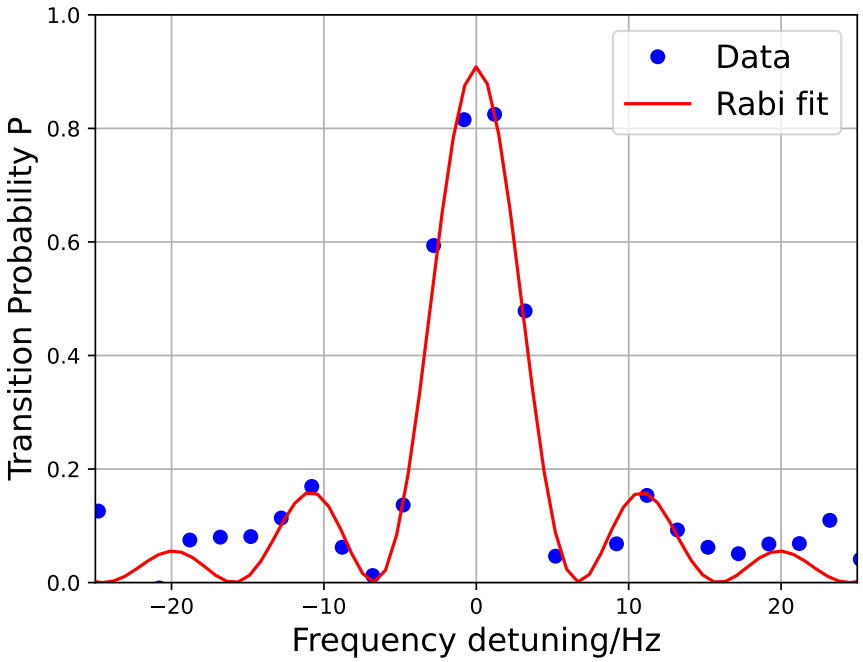

Fig. 2.17 Transition probability in the clock excited state, obtained with the Rabi spectroscopy. The blue dots are experimental data, while the red line represents the fit performed with Eq. 2.1 adapted to our specific case (see main text). The probe pulse is 120 ms long, and the consequent Fourier-limited linewidth is 6.6 Hz.

transition frequency of a two-level system, through a resonant probe laser pulse of duration t. In this case, if the laser probe has a frequency detuning δ, the probability of finding the atom in the excited state is given by [85, 86]:

$$P = \frac{\Omega^2}{\Omega^2 + \delta^2} \sin^2\left(\frac{\sqrt{\Omega^2 + \delta^2}\, t}{2}\right) \tag{2.1}$$

Since the Rabi frequency depends on the intensity of the probe ($\Omega \propto \sqrt{I}$), by adjusting the clock pulse parameter I and t, it is possible to obtain the so-called "π-pulse": a probe pulse such that $\Omega t = \pi$. When the atomic sample interacts with a π-pulse,

all the atoms in the ground state are excited and occupy the upper level of the clock transition. In this case, the excitation probability is maximized for $\delta = 0$, where it assumes value $P \simeq 1$. Moreover, the line shape has a Fourier-limited linewidth that depends on the probe pulse duration as $\gamma \sim 0.8/t$. To reduce the linewidth, it is thus necessary to use an interrogation pulse as long as possible according to the coherent time of the clock laser. Figure 2.17 shows the IT-Yb1 clock signal we obtain with the Rabi spectroscopy and a probe pulse 120 ms long. The resulting linewidth is about 7 Hz, evaluated by fitting the signal with Eq. 2.1, adapted to the case of harmonic trapping potential and a Boltzmann distribution between the vibrational energy levels [93].

Sidebands spectroscopy

When an atom is trapped into an optical lattice, its electronic energy structure presents a vibrational splitting that, in the harmonic approximation, is $E_{vib} = U_0 + \hbar\omega_z(n+\frac{1}{2})$. The deeper the lattice, the more the vibrational sublevels will be separated. If the vibrational splitting is much larger than the probe energy recoil that an atom can gain by absorbing and re-emitting a photon during the clock interrogation, the atom is in the so-called Lamb-Dicke regime: $\eta = \sqrt{\frac{E_r^{Yb}}{\hbar\omega_z}} \ll 1$, where η is the Lamb-Dicke parameter. Therefore, in the Lamb-Dicke regime, if the clock transition is sufficiently narrow ($\Gamma/\omega_z \ll 1$), it is possible to distinguish among different atomic transitions occurring between different vibrational sublevels $|n\rangle$.
The Sideband spectroscopy is a probing technique that allows to distinguish between atomic transitions involving different vibrational states $|n\rangle$. In particular, if the interrogation pulse has enough power, a detuning sufficiently large and a duration smaller than the radial oscillation period, the atomic signal obtained with the sideband spectroscopy assumes the profile shown in Fig. 2.18. The central peak is the carrier ($\Delta n = 0$) and is power broadened by a pulse such that $\Omega t \gg \pi$ and thus the maximum excitation probability at zero-detuning is about 0.5. The lateral sidebands account for the transitions $\Delta n = \pm 1$. In particular, the red sideband at a lower frequency with respect to the carrier is formed by atoms that occupy a final vibrational state lower than the starting one. On the contrary, the blue sideband signal is composed of the contributions of atoms that make a transition with a higher final vibrational state than the initial one.
The Sidebands spectroscopy is a powerful technique to measure the lattice properties.

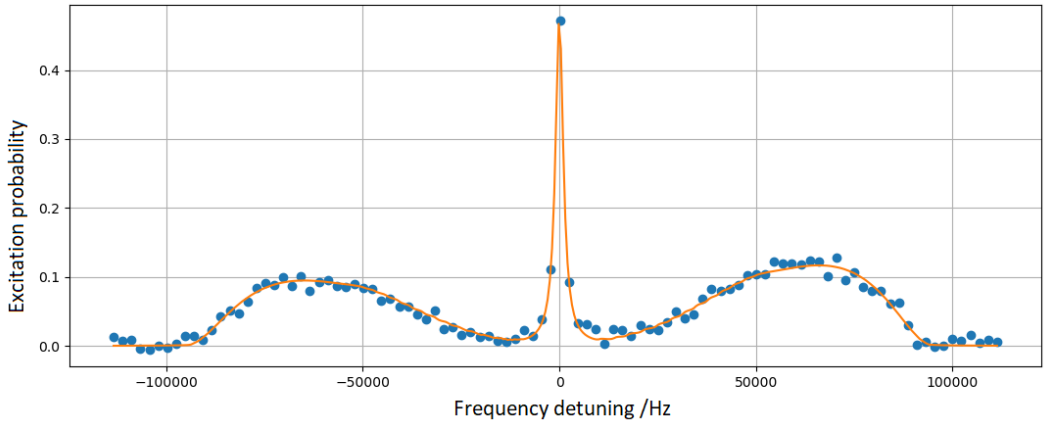

Fig. 2.18 Sideband spectroscopy signal. The blue dots represent the excitation probability at different detuning, while the orange line is the fit. The central peak is the carrier, and it is formed by atoms that make a transition without changing their vibrational state. The lateral sidebands arise from atoms that change their vibrational state by one unit.

Indeed the sideband shape depends on the atomic radial motion within the lattice well and the lattice depth [93]. Moreover, since the atoms that occupy the $|n = 0\rangle$ vibrational state do not contribute to the red sideband, it is possible to evaluate the axial temperature by measuring the asymmetry in the sideband height. By fitting the sideband signal, it is thus possible to evaluate the lattice depth and the temperature (both radial and axial) of the trapped atoms [93]. For example, from the fit of the sideband signal in Fig. 2.18, we obtain a lattice depth of $570(7)\,E_r$, a radial temperature of $16(2)\,\mu$K and an axial temperature of $12(2)\,\mu$K.

2.5.4 Repumper and detection

Once the clock transition ${}^1S_0 \rightarrow {}^3P_0$ has been interrogated, the detection process occurs. It consists in measuring the fraction of atoms that populate the excited state ${}^3P_0$ after the clock pulse. The detection procedure is composed of three 4 ms long light pulses at 399 nm (see Fig. 2.14). The detection beam has a stabilized power of about 0.7 mW and a beam $1/e^2$ radius of 0.5 mm. The propagation axis of the detection pulses is on the horizontal plane (see Fig. 2.2), thus orthogonal to the clock pulse. The fluorescence signal is collected by a photomultiplier tube (PMT). The first pulse is applied just after the interrogation process and measures the number of atoms N_g that have not interacted with the clock laser and occupy the ground state ${}^1S_0$. After the first pulse, the ground state is empty and a second pulse quantifies

the background signal N_{bkg}. Finally, the third pulse is used to evaluate the fraction of atoms that have populated the excited state after the clock interrogation N_{e}. To do this, it is necessary to optically repump the excited atoms into the ground state. For this purpose, we use a repumper laser at 1389 nm, resonant to the transition $^3\mathrm{P}_0 \rightarrow {}^3\mathrm{D}_1$. The atomic levels involved in the repumper scheme are sketched in Fig. 2.1. Once in the $^3\mathrm{D}_1$ state, atoms spontaneously decay first in the $^3\mathrm{P}_1$ state and then in the ground state, with an efficiency of about 90%. At this point, the fluorescence of the repumped atoms is measured by the third detection pulse.
The excitation probability P is then evaluated as:

$$P = \frac{N_{\mathrm{e}} - N_{\mathrm{bkg}}}{(N_{\mathrm{g}} - N_{\mathrm{bkg}}) + (N_{\mathrm{e}} - N_{\mathrm{bkg}})} \tag{2.2}$$

By measuring the excitation probability as a function of the clock laser frequency, it is possible to obtain the profile shown in Fig. 2.17 and 2.18. This line shape has a derivative that presents its maximum and minimum values in correspondence with the line half-height points that are frequency detuned from the atomic transition by $\gamma/2$. Consequently, close to these values, the sensitivity to the LO frequency is thus maximized: a shift in the LO frequency generates the biggest variation in the excitation probability. Therefore, during the clock operation, we modulate the LO interleaving cycles with frequency detuning of $\pm\gamma/2$. For these frequency values, the expected fraction probability is $P = 0.5$, but when the LO frequency presents any frequency fluctuations, the excitation probability is different from the expected value. A digital correction is then applied to the clock AOM (see Fig. 2.2) to guarantee the resonance of the LO to the atomic reference.
As described in the first chapter (Sec. 1.3), the frequency of the LO is continuously measured by a frequency comb. The frequency value read by the comb can be compared to a Cs clock frequency to evaluate the absolute frequency of Yb.

2.6 IT-Yb1 instability

As anticipated in Section 1.2 the stability of an atomic clock is expressed in terms of the Allan deviation $\sigma_y(\tau)$. This quantity evaluates the level of frequency fluctuations introduced by statistical noise in the clock system. By observing the behavior of the Allan deviation as a function of the averaging time τ, it is possible to identify the

dominant noise sources. When only the white frequency noise is considered, the Allan deviation assumes the form of Eq. 1.1 and is proportional to $\tau^{-1/2}$.
Figure 2.19 shows the Allan deviation of an interleaved measurement of IT-Yb1. Data are acquired by alternating the clock in two different operating conditions in

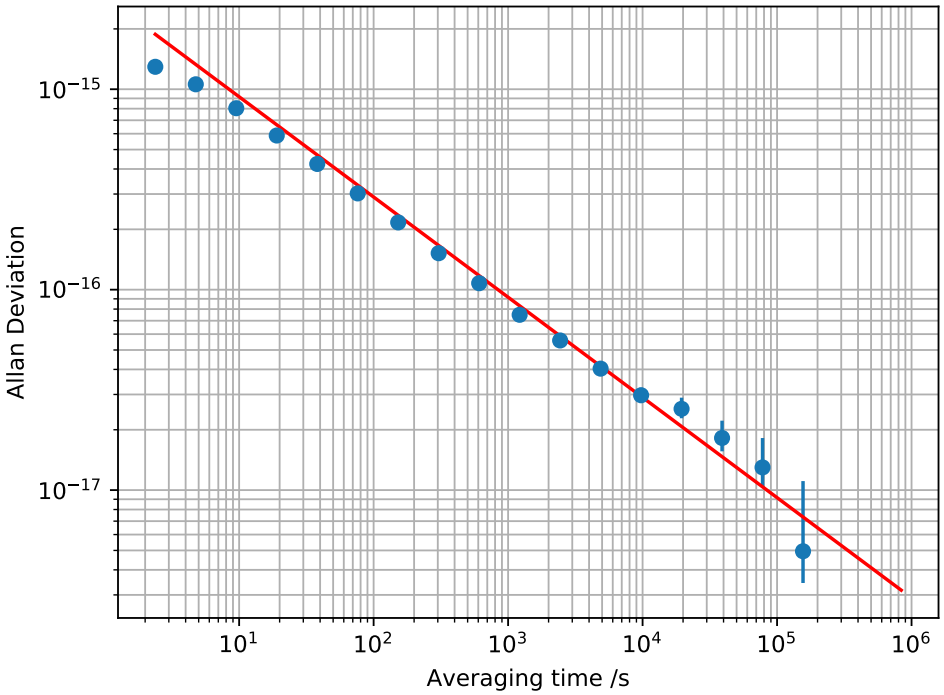

Fig. 2.19 IT-Yb1 instability of an interleaved density shift measurement. Data in terms of Allan deviation are shown as blue dots and their trend as a function of the averaging time is well described by a white frequency noise that is represented by the solid red line. The clock stability resulting from the fit is about $2.9 \times 10^{-15}/\sqrt{\tau/s}$.

terms of atomic density. The data shown in the Figure have been collected from January 2023 to March 2023 over about 40 days, for a total effective time of more than 230 h. The experimental data show the typical trend of white frequency noise, which corresponds to an instability of about 2.9×10^{-15} at 1 s of averaging time. The current stability of IT-Yb1 is limited by the Dick effect (see Sec. 1.2) associated with the ultrastable laser.

Chapter 3

Evaluation of systematic shift affecting IT-Yb1: uncertainty budget

The evaluation of systematic effects acting on the atomic clock is crucial to measure the unperturbed frequency of the clock transition. Indeed, the environment may perturb the clock and introduce an alteration in the clock energy levels. The accuracy of a frequency reference strongly depends on how well these systematic shifts are characterized. There are numerous sources of systematic shifts, such as inhomogeneity in the temperature, the presence of stray magnetic or electric fields, the interaction between atoms and the laser photons, atomic collisions and so on. Nevertheless, in the last decades, the knowledge of optical clocks and the development of strategies to cancel or determine these frequency shifts have led to a total systematic uncertainty $\delta\nu/\nu$ at the level of 10^{-18} [29, 8, 9, 94, 40, 7].
Table 3.1 reports the typical uncertainty budget of IT-Yb1. The major contributions to the relative uncertainty are the lattice shift and the blackbody radiation, which are caused by the presence of the lattice radiation and the non-zero temperature of the environment. The implementation of the new vertical lattice discussed in Section 2.5.1 allows us to reduce the lattice power during the clock operation and leads to benefits in terms of density shift, lattice shift and tunneling.

In this chapter, I will discuss in detail the contributions to the uncertainty budget I have characterized during my Ph.D. In particular, in Section 3.1, I present the analysis of the density shift, in Section 3.2 the DC Stark shift contribution, in Sections 3.3 and 3.4 the light shift introduced by the lattice and the probe lasers. In

Effect	Rel. Shift/10^{-17}	Rel. Unc./10^{-17}
Density shift	-0.5	0.2
Static Stark shift	-1.7	0.2
Fiber links	0.05	0.10
Lattice shift	1.5	1.2
Probe light shift	0.04	0.03
Zeeman shift	-3.12	0.02
Blackbody radiation shift (room)	-234.9	1.2
Blackbody radiation shift (oven)	-1.3	0.6
Background gas shift	-0.5	0.2
Servo error	-	0.3
AOM switching	-	0.1
Line pulling	-	0.02
Gravitational redshift	2599.5	0.3
Total	2359.1	1.9

Table 3.1 Uncertainty budget Yb optical lattice clock at INRiM.

Section 3.5, I describe the phase noise shift introduced by the propagation of the probe laser toward the fiber. Afterward, I briefly discuss the other contributions to the uncertainty budget in the following order: the Zeeman shift in Section 3.6, the blackbody radiation shift in Section 3.7, the background gas shift in Section 3.8, the tunneling shift in Section 3.9, the servo error shift in Section 3.10, the AOM switching shift in Section 3.11, the line pulling shift in Section 3.12 and finally the gravitational redshift in Section 3.13.

3.1 Density shift

The density shift is a perturbation in the clock frequency caused by the collisions between the atoms trapped in the potential well of the optical lattice [95–97]. The scattering theory, handled with a quantum mechanical approach and combined with the partial wave expansion approximation, describes the physics of atomic collisions. If we consider a low-energy collision, i.e., an interaction between sufficiently cold atoms, only the first two terms of the expansion are relevant. These lead to the so-called s-wave and p-wave collisions. Since ^{171}Yb is a fermionic isotope, the s-wave interactions between identical atoms are suppressed thanks to the Pauli exclusion principle [98]. In addition, the p-wave collision should be negligible for atoms colder

than 30 μK, a condition usually fulfilled in optical lattice clocks [99]. As a result, the density shift is expected to be negligible in a ^{171}Yb optical lattice clock. Despite this, the non-ideal experimental conditions make the density shift significant. Indeed, the clock pulse coherently excites all the atoms from the ground state $|g\rangle$ to the excited state $|e\rangle$ only if the probe pulse is π. As described in Section 2.5.3, this happens if the intensity and the duration of the probe pulse are such that $t\Omega = \pi$. In this case, all the atoms are described by the same wave function and can not interact in s-wave. However, in the non-ideal case, the atomic cloud is probed by a clock pulse with a Gaussian intensity and a finite size. Therefore, atoms experience an inhomogeneous Rabi frequency $\Delta\Omega$. When an atom interacts with a clock pulse $t\Omega \neq \pi$, its wave function is a linear combination of $|g\rangle$ and $|e\rangle$. As a consequence, atoms that interact with a pulse characterized by a different local intensity will not have identical final wave functions, and the s-wave collisions are not suppressed [93, 100].
Furthermore, s-wave collisions also arise if the spin-polarization process is not optimized. Indeed, in this case, the atoms may populate different sublevels $m_F = \pm 1/2$ of the ground state (see Fig. 2.1), and they are distinguishable.
Besides the s-wave collisions, also the p-wave interaction may be relevant in optical lattice clocks, even if the atomic temperature is lower than 30 μK [95].
The theoretical treatment of the density shift is particularly challenging. Indeed, it depends on several experimental parameters related both to the interrogation pulse (duration, intensity and frequency [93, 101, 95]) and to the trapping conditions [71, 102, 96]. However, in the typical experimental conditions of optical lattice clocks, each lattice site is occupied by a single atom or a couple of atoms. In this case, the frequency shift is linear in the atomic density [103, 102].
In an optical lattice clock, one of the experimental parameters on which the density shift depends is the lattice depth U [96]. From a theoretical point of view, by considering two colliding atoms and their interaction parameters, it is possible to predict how the density shift $\delta\nu_{\text{density}}$ depends on the lattice intensity and, consequently, on the lattice depth. In particular, if only s-wave collisions are considered $\delta\nu_{\text{density}}^{\text{s-wave}} \propto U^{3/4}$. On the other hand, if p-wave collisions are taken into account, the density shift is $\delta\nu_{\text{density}}^{\text{p-wave}} \propto U^{5/4}$.

Evaluation of IT-Yb1 density shift

During the clock operation, we measured the density shift of IT-Yb1 every day

in the working conditions. The density shift is evaluated by interleaving two clock cycles with different atomic densities. To do that, we change the duration of the slower pulse while maintaining the total clock cycle time unchanged. The result is scaled to a constant number of atoms trapped in the lattice of about 150. Figure 3.1

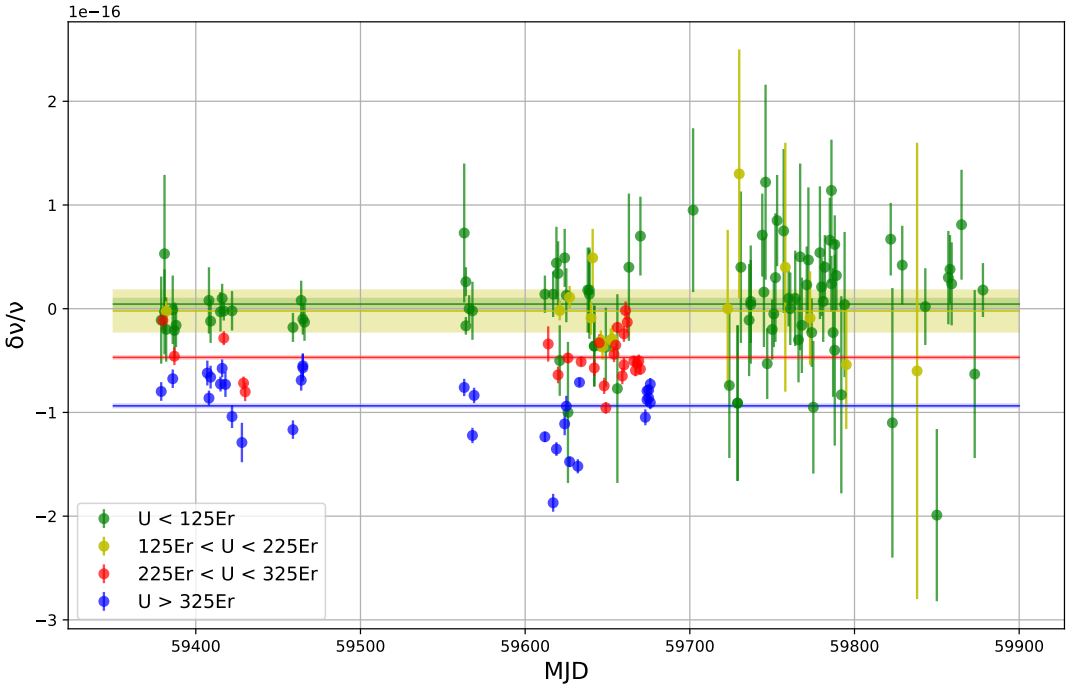

Fig. 3.1 Daily density shift measurements reported as a function of MJD. Different colors correspond to different lattice depths, as illustrated in the legend.

shows the result of the daily density shift measurements we performed from June 2021 to October 2022 as a function of the Modified Julian Date (MJD). The different colors correspond to different lattice depths, as reported in the legend. As expected [96], the density shift increases with the lattice depth. The solid lines represent the mean value for each data set, and the shaded area is the relative uncertainty. From this characterization, we evaluate the density shift for each lattice depth interval and the results are reported in Table 3.2. The progressive increment in the uncertainty associated with each measurement is likely due to a gradual worsening of experimental conditions which results in a reduction of the number of trapped atoms.

The contribution of the density shift to the IT-Yb1 uncertainty budget is evaluated by

Lattice depth/E_r	Rel. Density shift/10^{-17}	Rel. Uncertainty/10^{-17}
$U < 125$	0.4	0.5
$125 < U < 225$	-0.2	20
$225 < U < 325$	-4.6	0.2
$U > 325$	-9.3	0.2

Table 3.2 Results of the density shift analysis evaluated for several lattice depth ranges.

considering only the measurements performed at the usual operation condition, i.e., with a lattice depth of 100(10) E_r and the resulting relative frequency shift and its uncertainty are $\frac{\delta\nu_{\text{density}}}{\nu} = -5(2) \times 10^{-18}$.

Moreover, during this characterization, the density shift has been evaluated for

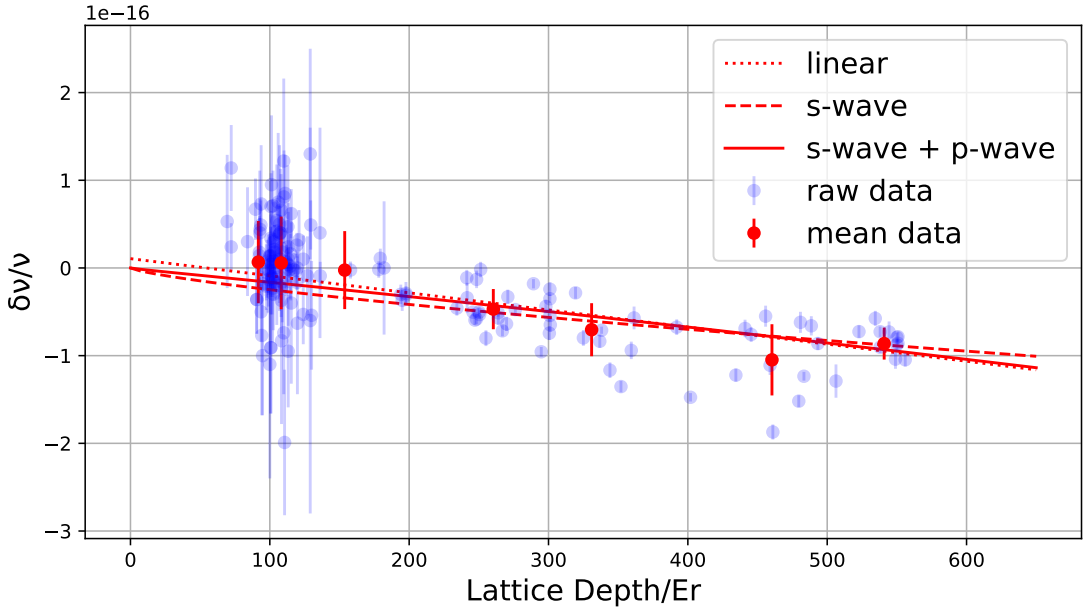

Fig. 3.2 Relative frequency shift $\delta\nu_{\text{density}}/\nu$ as a function of the lattice depth. Sky blue data are the single measures, evaluated typically in one day of measurement. Red data are the mean value calculated by considering different ranges of lattice depth (60-100E_r; 100-120E_r; 120-200E_r; 200-300E_r; 300-400E_r; 400-500E_r; 500-600E_r). The mean data are fitted with three different functions: the dotted red line represents a linear fit, the dashed red line is a power law fit considering only the s-wave contribution, and the solid red line is a power law fit considering both the s-wave and the p-wave contributions. All the fits well reproduce the experimental data.

different lattice depths ranging from 90 E_r to 550 E_r. It is thus possible to observe

the behavior of the density shift as a function of the lattice depth, and the results are reported in Fig. 3.2. The sky blue data represent the row daily measures, while red data are the mean shift values by considering different ranges of lattice depth. The uncertainty is calculated as $\sigma = \sum_{i=1}^{N} \frac{x_i - \bar{x}}{\sqrt{N}}$, where x_i is the single value, $\bar{x}$ is the mean value and N is the number of measurements. The experimental data are fitted with several functions: a linear function, and two power low functions, one for the s-wave contribution ($\frac{\delta \nu_{\text{density}}}{\nu} \propto U^{3/4}$) and the other to consider also the contribution of p-waves ($\frac{\delta \nu_{\text{density}}}{\nu} \propto U^{3/4} + U^{5/4}$). All the fit functions we used describe well the experimental data. Indeed, the data are too scattered to distinguish among the different functions. The scatter of the data is due to daily changes in the working conditions and in experimental parameters to which the density shift is very sensitive, such as the frequency of the green radiation and the power used to interrogate the atoms [71].

It is important to note that since the density shift increases with the lattice depth [96], it is crucial to trap the atoms at the lowest possible lattice depth. For this reason, the implementation of the vertical lattice has been fundamental to reducing the density shift. Indeed, it allowed us to decrease the clock working point from about $220\,\mathrm{E_r}$ [68, 92] to $100\,\mathrm{E_r}$ [33].

To further reduce the density shift, it is necessary to increase the lattice waist and reduce the lattice depth U, to minimize the interaction between the trapped atoms. In the coming years, we plan to develop a new optical lattice clock (IT-Yb2) provided with a cavity-enhanced optical lattice that will ensure the experimental trapping conditions required to reduce the density shift. Moreover, the density shift could be better characterized if we increased the stability of our measurements. To do that, it is necessary to have a more performing ultrastable cavity to stabilize the Yb clock laser. A new ultrastable cavity has been purchased by the INRiM frequency standard group and will be installed in the next few years. Another possible strategy to reduce the density shift is the implementation of a gravity-tilted shallow lattice where atoms are described by partially delocalized Wannier-Stark states. Indeed, in this case, it is possible to define a "magic" lattice depth that suppresses the density shift [104].

3.2 DC Stark shift

A stray electric field in the trapping region induces the so-called DC Stark shift or Static Stark shift [105–107]: a frequency shift in the clock transition. Considering an electric field E, the DC Stark shift is given by [105, 106]:

$$\delta\nu_{\text{StarkDC}} = -\frac{1}{2}\Delta\alpha(\delta E)^2 \tag{3.1}$$

where $\Delta\alpha$ is the difference between the static polarizabilities of the two states forming the clock transition.
The strategy to measure the DC Stark shift involves the application of a controlled electric field in the trapping region. The consequent shift experienced by the atoms is schematized in Figure 3.3. In the absence of a stray field δE, the application of an

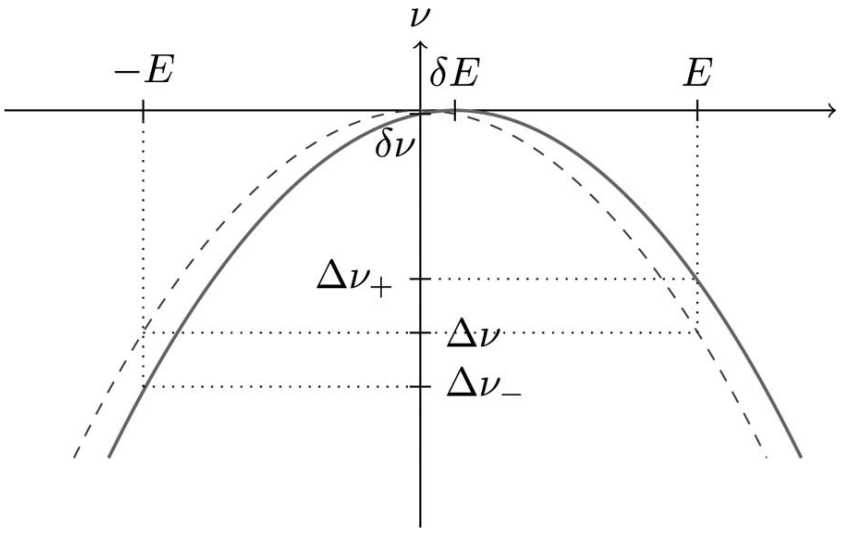

Fig. 3.3 Frequency shift behavior as a function of the external electric field magnitude, adapted from [105]. The two parabolas describe the frequency shift produced by the external field in the absence (dashed line) or in the presence (solid line) of a stray electric field δE.

external electric field will introduce a variation in the clock frequency described by the dashed parabola, and two electric fields equal and opposite will generate the same frequency shift. On the contrary, if $\delta E \neq 0$ the clock frequency will be described by the solid parabola. In this case, the application of two opposite electric fields will result in two different frequency shifts $\Delta\nu_+$ and $\Delta\nu_-$.

By following this approach, it is possible to calculate the DC Stark shift as [105]:

$$\delta\nu_{\mathrm{StarkDC}} = \frac{(\Delta\nu_{+} - \Delta\nu_{-})^2}{16\Delta\nu} \tag{3.2}$$

where $\Delta\nu$ is the average DC Stark shift.

Evaluation of IT-Yb1 DC Stark shift

In our setup, the aluminum vacuum chamber partially acts as a Faraday cage and shields the atoms from any external field. However, electrical charges may deposit on the insulating surface of the silica windows inside the vacuum chamber. Since the vertical windows are larger and closer (about 25 mm) to the atomic cloud than the lateral ones, it is expected that charges accumulating on these would contribute more to a possible stray electric field.

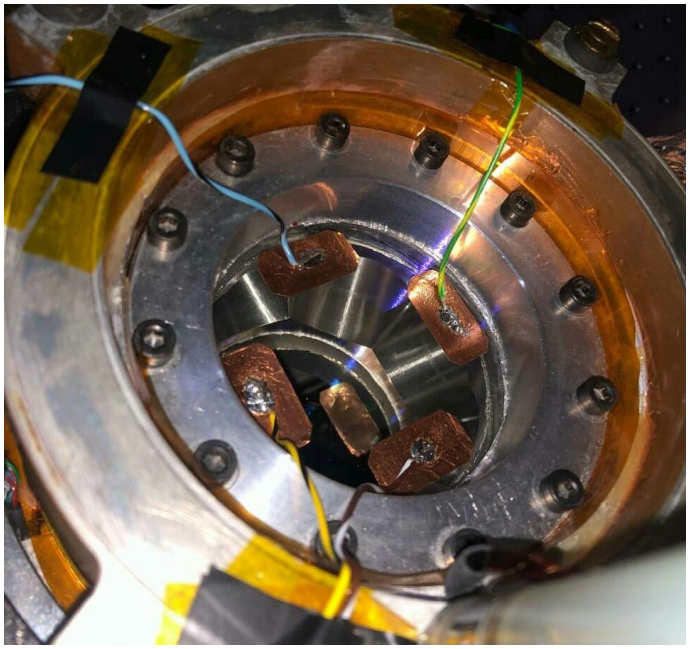

Fig. 3.4 Picture of the experimental setup to characterize the Stark shift along the three directions. This Figure shows the upper vertical window, provided with four electrodes.

In 2019 a first evaluation of the DC Stark shift affecting IT-Yb1 was performed [92]. In that case, two ring electrodes were placed on the surfaces of the vertical windows to generate an electric field in the vertical direction. During my Ph.D., we implemented a more complex setup to execute a more exhaustive characterization of this

shift along the three spatial axes. It consists of eight independent electrodes, four on each vertical window. A picture of the setup for the DC Stark shift characterization is shown in Fig. 3.4. With a custom programmable High Voltage Switchboard Driver (HVSD), we can apply a voltage ranging from $-150\,\mathrm{V}$ to $150\,\mathrm{V}$ independently to each electrode. The typical rising and falling times are of the order of $10\,\mu\mathrm{s}$, and the applied voltage accuracy is at the level of few mV. By properly applying different voltage configurations to the electrode is possible to generate external electric fields and measure the DC Stark shift along the three directions.

Figure3.5 schematically illustrates the different configurations of the applied voltage

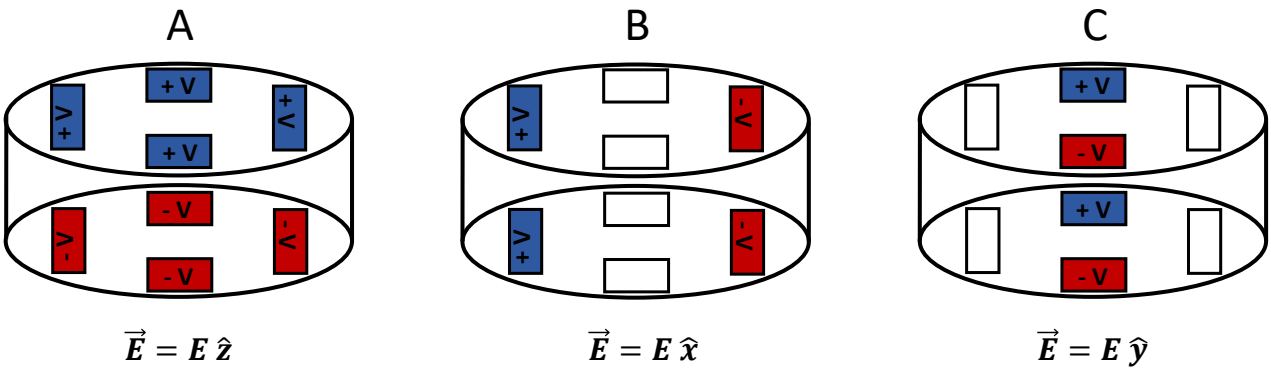

Fig. 3.5 Scheme of different applied voltage configurations allowing the generation of an electric field along three orthogonal directions. In particular, the configurations illustrated in sketches A, B and C produce an electric field along the $\hat{z}$, $\hat{x}$ and $\hat{y}$ axes, respectively.

to the electrodes that allow us to characterize the DC Stark shift along the three directions $\hat{z}$, $\hat{x}$ and $\hat{y}$.

Results and analysis

Figure 3.6 shows the frequency shift induced by the application of a voltage along the vertical direction (scheme A of Figure 3.5). The experimental data are obtained with an interleaved measurement alternating the configurations with and without the external electric field. The data are fitted with a parabola, as expected from Eq. 3.2. By repeating this analysis with external fields orientated along the three axes, it is possible to calculate $\Delta\nu$ associated with each direction [106, 105, 107].

Then, to obtain the value of $\Delta\nu_+ - \Delta\nu_-$, we perform interleaved clock measurements alternating opposite configurations of applied voltage on the electrode. For each spatial direction ($\hat{z}$, $\hat{x}$ and $\hat{y}$), we alternate opposite configurations of each case (A, B

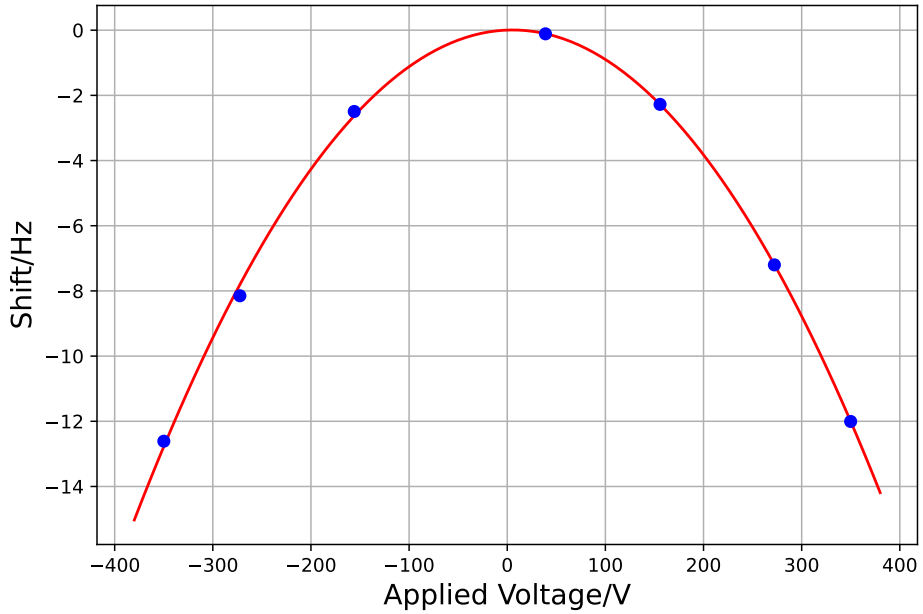

Fig. 3.6 Parabolic behavior of the DC Stark shift induced by applying a voltage to the electrodes along the vertical direction. Blue data are obtained by interleaving measurements alternating the applied voltage with the zero-voltage configuration. The red line is the fit performed with Eq. 3.2. The uncertainties associated with experimental data are too small to be visible on the scale of the plot, but typically their value is of the order of 5×10^{-2} Hz.

and C) sketched in Fig. 3.5.

Finally, since the DC Stark shift is proportional to the square of this quantity (Eq. 3.2), we use Monte Carlo methods [108] to propagate the probability distribution associated with the measured value and calculate the frequency shift and its uncertainty.

From this 3D characterization, an unexpected stray electric field has been detected on the horizontal plane. This field is orientated along the oven-slower direction (see Fig. 2.2), hereafter called the x direction. The stray field slightly changes from day to day, but it does not decay over a long time. Figure 3.7 reports the x component of the DC Stark shift (green dots) daily measured as a function of MJD. As we can see, the frequency shift is at the level of 10^{-16} and corresponds to a stray electric field of about $1\,\mathrm{V/cm}$.

We performed several tests to understand the source and the nature of the stray field and to eliminate it. At first, the silica windows were illuminated with a commercial UV source. Indeed, the UV light should extract the charges from the dielectric surfaces thanks to the photoelectric effect [105, 109–111]. However, although the

UV application had an effect in the short term, this method was not successful over a long period, as the stray field returned after a few days. Moreover, we also tried to eliminate any possible charge deposits on the windows by employing an ionizer (Zero Volt Ionizer Desco Emit Model 80670). However, this method was not successful either. In addition, to exclude a possible effect of the slower beam or charges on the in-vacuum slower mirror, interleaved measurements were performed by closing the gate valve (see Section 2.4), thus blocking the radiation. We also tried to reveal an influence associated with the ion pumps by temporarily turning them off during the measurement, but we did not obtain a relevant result.
The direction of the field, aligned with the atomic beam, suggests that it is induced by the oven, which may emit some ionized particles that deposit on the silica windows. However, even an effect due to the blue MOT beams is not to be excluded [112, 113].

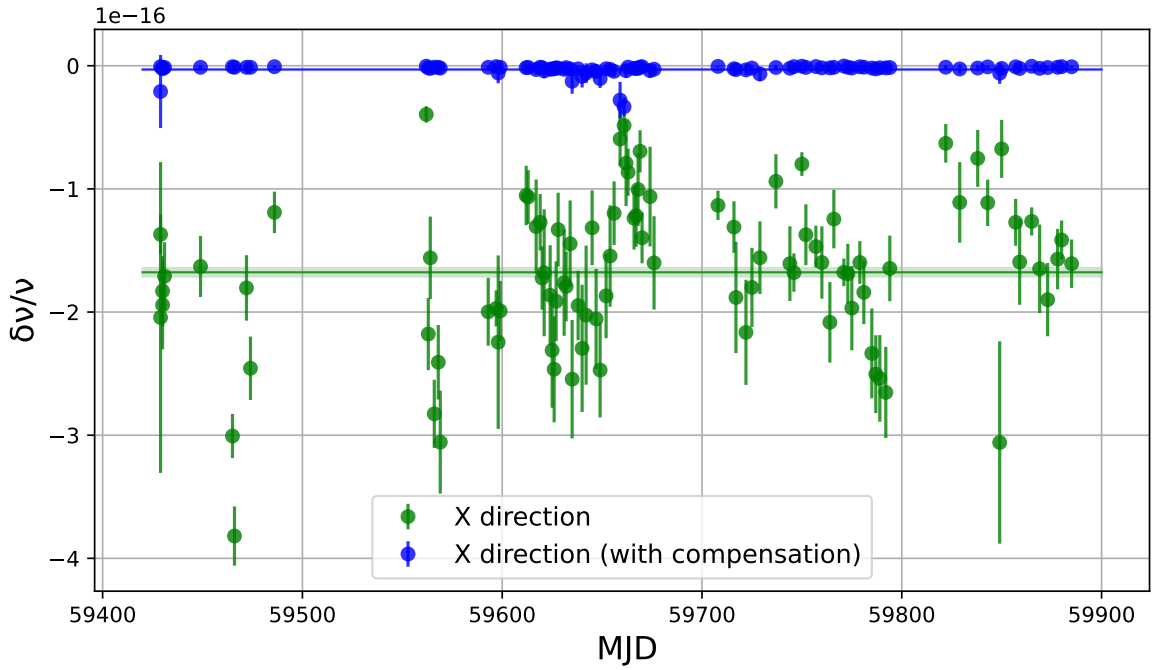

Fig. 3.7 Daily DC Stark shift along the x direction measured from August 2021 to October 2022 reported as a function of MJD. Experimental data obtained with and without compensation are shown as blue and green dots, respectively. For each data set, the mean is reported as a solid line, while the dashed areas represent the uncertainty. The final results of this analysis are provided in the main text.

Since we could not eliminate the stray field, we implemented a compensation scheme

to eliminate the consequent frequency shift. Each day we measured the DC Stark shift along the x direction, and we applied a voltage to the electrodes to generate an opposite field. The results of the compensation in terms of frequency shift are shown in Fig. 3.7. The daily results of the measured frequency shift along the x direction (green dots) are compared to the compensated values (blue dots). For each data set, the solid line and the dashed areas represent the mean and the relative error. This analysis provides a DC Stark shift value along the x direction of

$$\frac{\delta\nu^{x}_{\text{StarkDC}}}{\nu} = -1.68(4)\times 10^{-16} \qquad \text{without compensation}$$
$$\frac{\delta\nu^{x,comp}_{\text{StarkDC}}}{\nu} = -3.1(5)\times 10^{-18} \qquad \text{with compensation}$$

Despite the presence of the stray field, the compensation scheme allows us to reduce the DC Stark shift along the x direction below the 10^{-17} level.

The DC Stark shift for each direction is usually measured at least two or three times a week. Its trend over time is shown in Fig. 3.8. Each panel refers to a specific axis, as indicated in the legends. For the x-axis, I report only the compensated data.

Combining the three DC Stark shift values, it is possible to calculate the total DC Stark shift, which is reported in Fig. 3.9 as a function of MJD. The solid red line and the dashed region are the mean and uncertainty of the total DC Stark shift: $\delta\nu^{tot}_{\text{StarkDC}}\nu = -1.66(13)\times 10^{-17}$.

To complete the evaluation of the DC Stark shift, some systematic effects have to be considered.
Even though the technical specifications of the High Voltage Switchboard Driver ensure an accuracy of a few mV, we attribute to the applied voltage an uncertainty of 2 V. The consequent uncertainty on the DC Stark shift is 0.7×10^{-18}.
Another source of systematic uncertainty derives from a possible misalignment of the electrodes. If the electric fields generated by the electrodes are not perfectly aligned, the measurement axes are not orthogonal, and the resulting uncertainty is given by:

$$\Delta\delta\nu_{\text{non-orthogonal}} = 2E_xE_y\cos\theta_{xy} + 2E_xE_z\cos\theta_{xz} + 2E_yE_z\cos\theta_{yz} \qquad (3.3)$$

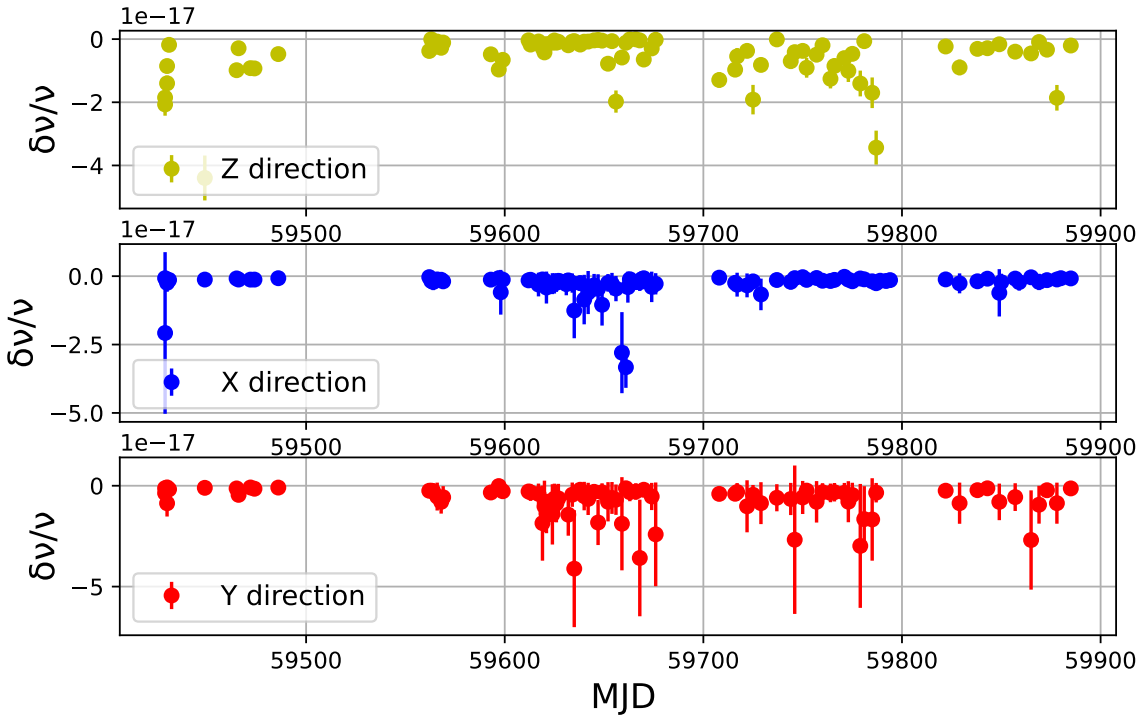

Fig. 3.8 3D characterization of the DC Stark shift over more than a year. Shift data along the z direction are shown in the top panel as yellow dots, while the middle and bottom panels report the shift along the x and y directions as blue and red dots, respectively. For the x-axis, only compensated data are shown.

Assuming a deviation from the orthogonal configuration of 5%, that corresponds to a misalignment of almost 5 degrees, the uncertainty on the DC Stark shift is $\frac{\Delta\delta\nu_{\text{non-orthogonal}}}{\nu} = 1.1 \times 10^{-18}$.

Table 3.3 summarizes the sources of uncertainty that characterize the DC Stark shift and their contribution. From this analysis, the DC Stark shift results to be $\frac{\delta\nu_{\text{StarkDC}}}{\nu} = -1.66(19) \times 10^{-17}$.

Effect	DC Stark shift relative uncertainty/10^{-18}
Statistical	1.3
Systematic V applied	1.1
Systematic non-orthogonality	0.8
Total	1.9

Table 3.3 Contributions to the uncertainty of the DC Stark shift evaluation. The Table reports both the statistical and systematic uncertainties.

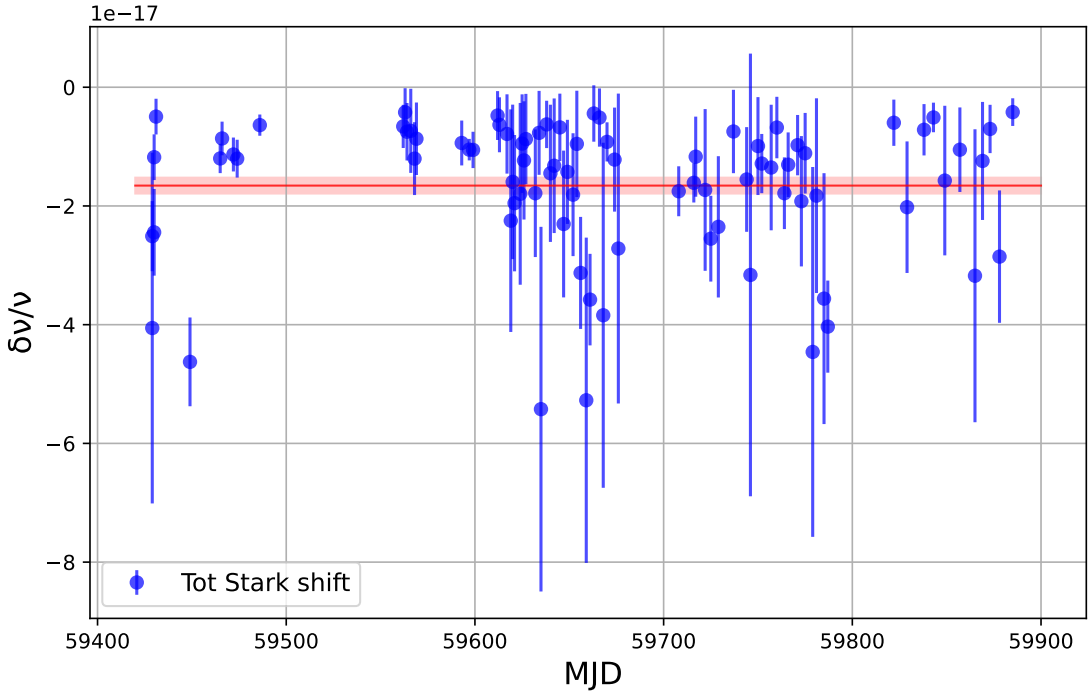

Fig. 3.9 Daily total DC Stark shift as a function of MJD. The solid line and the dashed areas represent the mean and the relative error.

Despite the presence of the stray field, thanks to the compensation scheme, the final shift introduced by the DC Stark effect is below the 10^{-18} level. However, to make the compensation process efficient, it is essential to measure the DC Stark shift at least twice a week.
A possible strategy to delete the stray field and reduce the DC Stark shift is to replace the atomic chamber with a new one that acts better as a Faraday cage. For example, a possible solution is to provide the windows of the atomic chamber with a coating of Indium Tin Oxide (ITO), a conductive and highly transparent material.

3.3 AC Stark shift: lattice shift

The AC Stark shift arises from the interaction of the atoms with the laser light during the clock interrogation. This interaction has an impact on the clock transition both in terms of frequency shift and line broadening. In a Yb clock, only the lattice and

the probe laser interact with the atomic ensemble during the interrogation. In this section, I will discuss the AC Stark shift introduced by the lattice laser, and I will refer to the AC Stark shift as "lattice shift" or simply "light shift". Instead, the probe light shift, i.e., the AC Stark shift generated by the probe laser is briefly discussed in the next section.

Theory

The interaction between an atom and a laser electric field of magnitude E and frequency ν_L leads to a frequency shift of the atomic transition described by [69]:

$$\hbar\nu = \hbar\nu_0 - \frac{1}{4}\Delta\alpha(\nu_L)E^2 - \frac{1}{64}\Delta\beta(\nu_L)E^4 \tag{3.4}$$

where ν_0 is the unperturbed transition frequency and the first- and second-order corrections depend on $\Delta\alpha$ and $\Delta\beta$, the difference between the polarizabilities and hyperpolarizabilities of the two states. The second-order term accounts for two-photon transition processes and it is negligible in a first approximation.
The polarizability is composed of several contributions: the electric dipole (E1), the electric quadrupole (E2), the magnetic dipole (M1) [69]

$$\alpha(\nu_L) = \alpha_{E1}(\nu_L) + \alpha_{E2}(\nu_L) + \alpha_{M1}(\nu_L) \tag{3.5}$$

In the first order, only the contribution of α_{E1} is relevant [69, 114]. In particular, for an electric field oscillating in time, α_{E1} is a dynamic quantity composed of a scalar, a vector and a tensor term [115]. In our case, the tensor component vanishes thanks to the spectroscopic properties of the Yb clock transition ($F = 1/2$ and $m_F = \pm 1/2$) [115]. Moreover, the vector contribution is negligible when the external magnetic field is perpendicular to the laser wavevector, as in our setup. Therefore, the dynamic electric dipole polarizability is approximated to its scalar contribution α_{E1}^S, which is sufficient to introduce a light shift of the order of 1 MHz [114, 116].
By following the approach suggested by Katori *et al.* [69], it is possible to eliminate the AC Stark shift introduced by the electric dipole polarizability α_{E1} by operating the laser at the so-called magic wavelength. Indeed, if the lattice laser operates at this wavelength, it modifies the two levels of the clock transition of the same amount, and the light shift of the whole transition is zero.

Once corrected for the electric dipole contribution, the higher-order effects due to multipolar interaction α_{E2}, α_{M1} and the higher-order term of Eq. 3.4 depending on the hyperpolarizability $\Delta\beta$ become relevant for an accurate evaluation of the light shift.

By considering an ensemble of atoms trapped in an optical lattice, approximating the trapping potential as harmonic and assuming that the lattice wavelength is close to the magic wavelength, it is possible to calculate the lattice shift as a Taylor expansion. Therefore, the frequency shift induced by two counterpropagating plane waves with the same intensity is [117–120, 96]:

$$\begin{aligned}\delta\nu_{LS} = &-\left(\tilde{\alpha}\Delta\nu + \frac{3}{4}\tilde{\beta}(2n_z^2+2n_z+1)\right)\frac{U_e}{E_r} - \tilde{\beta}\left(\frac{U_e}{E_r}\right)^2 + \\ &+ (\tilde{\alpha}\Delta\nu - \tilde{\alpha}_{QM})\left(n_z+\frac{1}{2}\right)\left(\frac{U_e}{E_r}\right)^{1/2} + \tilde{\beta}(2n_z+1)\left(\frac{U_e}{E_r}\right)^{3/2}\end{aligned} \tag{3.6}$$

where $\Delta\nu$ is the laser detuning from the magic frequency that cancels the electric dipole contribution, $\tilde{\alpha}$ is the slope between the differential polarizability and the lattice frequency, $\tilde{\beta}$ is the hyperpolarizability, and $\tilde{\alpha}_{QM} = \frac{1}{h}\alpha_{QM,|e\rangle} - \alpha_{QM,|g\rangle}$ accounts for the combined polarizability α_{E2} and α_{M1}. In this model, n_z is the average atomic longitudinal vibrational state and $U_e = \xi U_0$ is the effective longitudinal lattice depth. Indeed, due to their radial motion, the trapped atoms may experience a lower lattice depth [118, 71].

In the past few years, Beloy *et al.* proposed a new theoretical approach, which permits a simplification of the lattice shift treatment [121, 122]. In this approach, the longitudinal and radial motions of atoms trapped in the lattice potential are evaluated following the Born-Oppenheimer (BO) approximation [122]. Indeed, since the axial and radial atomic motion dynamics evolve in very different timescales, it is possible to treat them separately. In particular, by combining the BO approximation and the WKB (Wentzel Kramers Brillouin) approximation, the energy shift caused by the lattice is written as:

$$\Delta E = -U_0\frac{\Delta\alpha_{E1}}{\alpha_{E1}}X - U_0\frac{\Delta\alpha_{QM}}{\alpha_{E1}}Y - U_0^2\frac{\Delta\beta}{\alpha_{E1}^2}Z \tag{3.7}$$

where X, Y and Z are dimensionless factors that describe the ensemble averages motional states and depend on the specific atomic distribution. It is important to note that these factors assume the role of different effective trap depths and

their introduction allows a description of the AC Stark shift simply in terms of the maximum lattice depth U_0 instead of the term used in Eq. 3.6 $U_e = \xi U_0$. The quantities X, Y and Z depend on the lattice depth and the temperature T of the trapped atoms, and it is possible to demonstrate that if $T \propto U_0$, then X, Y and Z are constant (k_X, k_Y, and k_Z) [122]. A simulation of the X, Y and Z parameters as a function of the lattice depth is shown in Fig. 3.12. The red solid lines represent the constant trend that X, Y and Z assume when the atomic temperature is proportional to the lattice depth. Therefore, when this condition is satisfied, the lattice shift can be approximated as:

$$\frac{\delta \nu_{LS}}{\nu} = -\alpha^* U_0 - \beta^* U_0^2 \tag{3.8}$$

where α^* and β^* are U-independent polarizability and hyperpolarizability.
In the following, I will refer to the lattice frequency that zeroes the linear shift contribution as the true magic frequency.
In past years, the evaluation of the IT-Yb1 lattice shift has been performed by using Equation 3.6 [68, 92] and by attributing the known value of $\tilde{\beta}$ and $\tilde{\alpha}_{QM}$ for Yb [118, 123, 121]. More recently [33], we adopted the method proposed by Beloy *et al.*, and therefore we calculate the lattice shift through Equation 3.8.

Analysis

To follow the approach described by Beloy *et al.*, it is necessary to first analyze the behavior of the atomic temperature as a function of the lattice depth and confirm a linear scaling. To do so, we performed a series of clock measurements employing the sidebands spectroscopy. Indeed, as described in section 2.5.3, from the sideband spectrum it is possible to evaluate both the atomic temperatures (axial and radial) and the lattice depth. For each measurement, we varied the lattice depth by changing the lattice power. We note that the radial temperature is expected to be linear with the lattice depth, only if the atoms are loaded in the lattice directly in the experimental conditions used during the interrogation. Indeed, if the lattice power adiabatically changes after the atomic loading, the radial temperature is expected to show a square root scaling $T_r \propto \sqrt{U}$ [122, 120]. In this context, it was essential to have implemented the new vertical lattice that allows us to load the atoms directly in the optical lattice at the desired depth ranging from $90\,\mathrm{E_r}$ up to $550\,\mathrm{E_r}$. With the previous horizontal lattice setup instead, the atoms were always loaded at the same trap depth, which was then modified [68, 92].

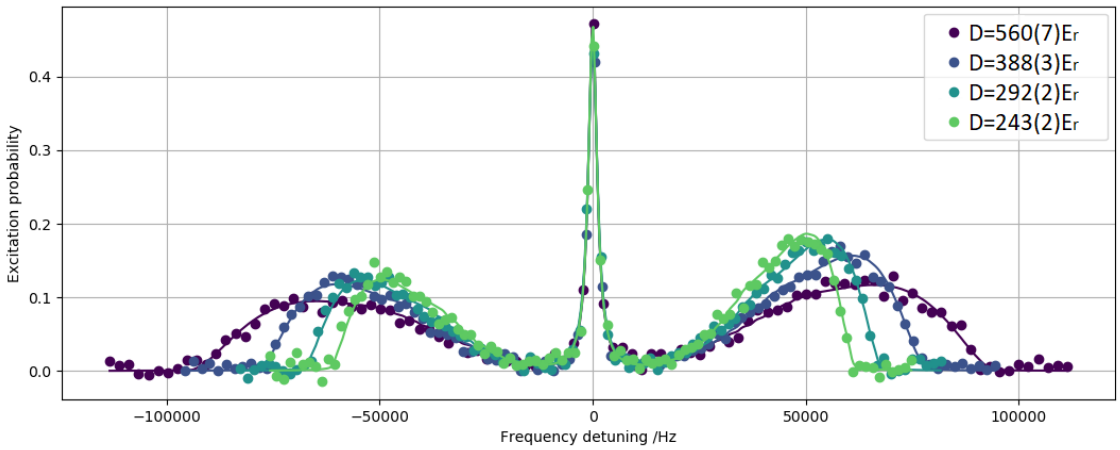

Fig. 3.10 Excitation probability as a function of the probe frequency detuning measured through sideband spectroscopy. Different colors represent measurements performed at different lattice depths. The carrier is well described by a Lorentzian fit, while the sidebands account for all the possible transitions between vibrational states $|n\rangle \rightarrow |n \pm 1\rangle$ [93, 96]. The legend shows the lattice depth calculated from the fit.

Figure 3.10 shows the spectra obtained performing sideband spectroscopy experiments at different lattice depths. From the fit, we can extract the temperature of the atoms at each lattice depth and analyze their dependency.
During the clock operation, the sideband measurement is performed daily, to monitor the stability of the experimental conditions. The resulting atomic temperature is shown in Figure 3.11, where the light blue dots and pink dots represent the axial and radial temperature measured each day. Instead, the blue and the red dots correspond to the average temperature in a certain range of lattice depth. The uncertainty is evaluated as $\sigma = \sum_{i=1}^{N} \frac{x_i - \bar{x}}{\sqrt{N}}$. The solid lines in Figure 3.11 confirm, in first approximation, a linear scaling of the axial and radial atomic temperature with the lattice depth. We note that the temperature dependence seems to match data better if a quadratic component is added to the fit function (dashed line in Figure 3.11). We can calculate the effect of this quadratic behavior on the parameters X, Y and Z of Eq. 3.7. The trend of X, Y and Z is shown in Figure 3.12 as a function of the lattice depth. We note that Y is not affected by the quadratic component of the temperature dependence, while X and Z are affected by a small correction that we assume to be linear in the lattice depth. In this case equation 3.7 becomes:

$$\Delta E = -U_0 \frac{\Delta\alpha_{E1}}{\alpha_{E1}}(k_X + k_X^* U_0) - U_0 \frac{\Delta\alpha_{QM}}{\alpha_{E1}} k_Y U_0 - U_0^2 \frac{\Delta\beta}{\alpha_{E1}^2}(k_Z + k_Z^* U_0) \qquad (3.9)$$

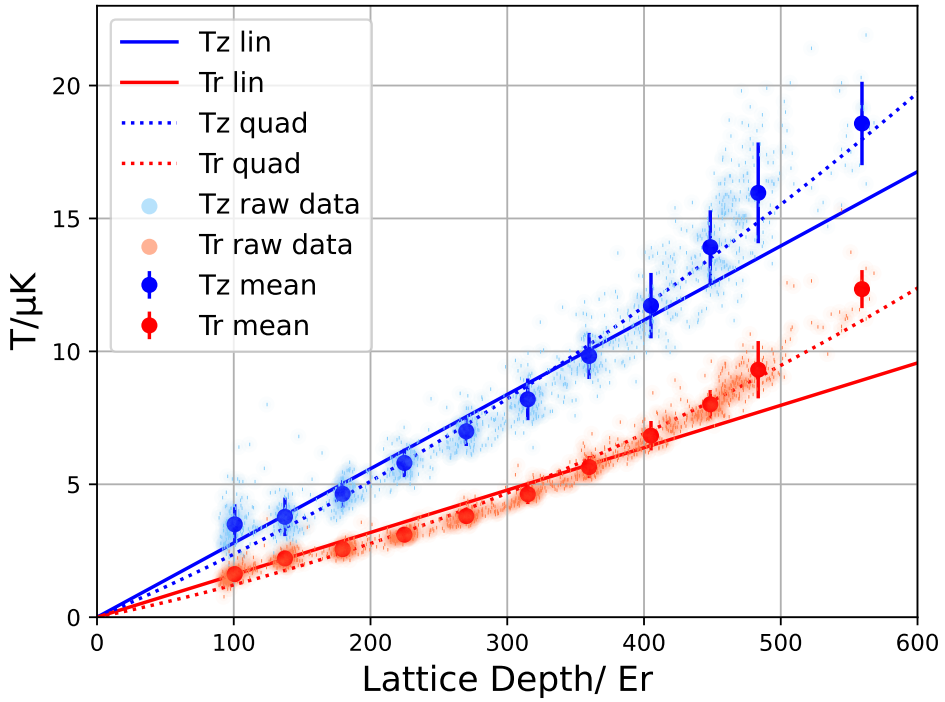

Fig. 3.11 Atomic axial (blue) and radial (red) temperature as a function of the lattice depth. Sky blue and pink dots represent row daily data, while blue and red dots are the average data. Solid lines correspond to a linear fit that, in first approximation, well describes experimental data. Instead, the dashed lines represent the result of a fit with also a quadratic component.

where k_X, k_Y and k_Z are the constant values that X, Y and Z assume if the temperature scales linearly with the lattice depth, while k_X^* and k_Z^* are the correction factors. We note that the contribution of k_X^* introduces a shift proportional to U_0^2, and its effect is thus included in β^*. The correction derived from k_Z^* is instead proportional to U_0^3, and its contribution is not taken into account in the characterization of the lattice shift performed with Eq. 3.8. However, considering the value of $\frac{\Delta\beta}{\alpha_{E1}^2}$ measured by Nemitz *et al.* [96] and $k_Z^* = 2\times10^{-4}\frac{U_0}{E_r}$ evaluated through the simulations, we can estimate the contribution of k_Z^* to the lattice shift, that in our operational condition ($U_0 = 100E_r$), is 5×10^{-19}. Therefore, even though the atomic temperature is not perfectly linear with the lattice depth, the consequent impact on the trend of X, Y and Z is small enough to allow us to analyze the lattice shift by applying the model of Eq. 3.8 to the experimental data.

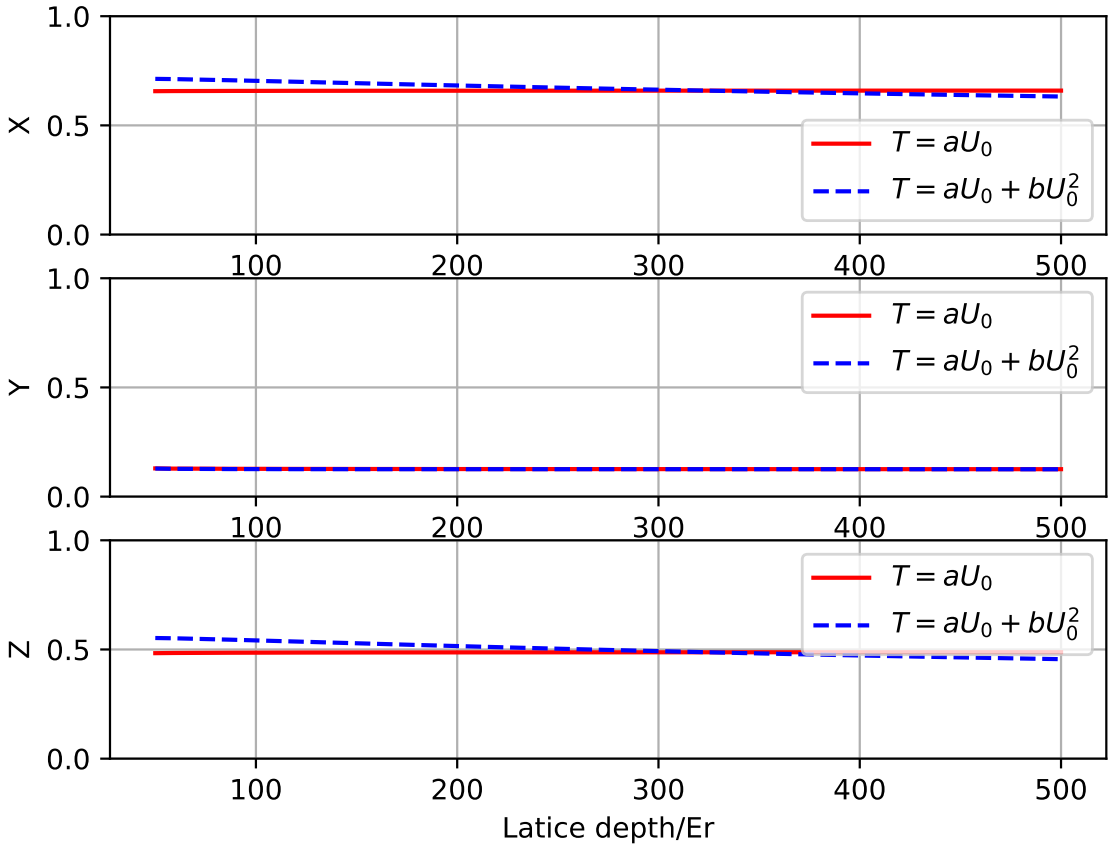

Fig. 3.12 X, Y and Z parameters (see Eq. 3.7) as a function of the lattice depth. The constant trend that these quantities follow when $T \propto U_0$ is reported as red solid lines, while blue dashed lines represent the trend when is added the quadratic component to the temperature dependence calculated through the fit function shown of Fig. 3.11.

The evaluation of the lattice shift occurs by interleaving clock measurements with different lattice depths. The differential data are corrected for the density shift, and the resulting values are shown in Figure 3.13. Solid lines correspond to the fit, performed with Eq. 3.8. This measurement is repeated for different lattice frequencies, as illustrated in the legend. The frequency values are reported as detunings evaluated with respect to 394 798 267 MHz, which is our working point.
From the fit, we can extrapolate the parameters α^* and β^* of Eq. 3.8 corresponding to our frequency working point, and we can evaluate the resulting lattice shift and its uncertainty. We note that since the shift increases with the lattice depth, the realization of the vertical lattice and the consequent reduction of the clock working

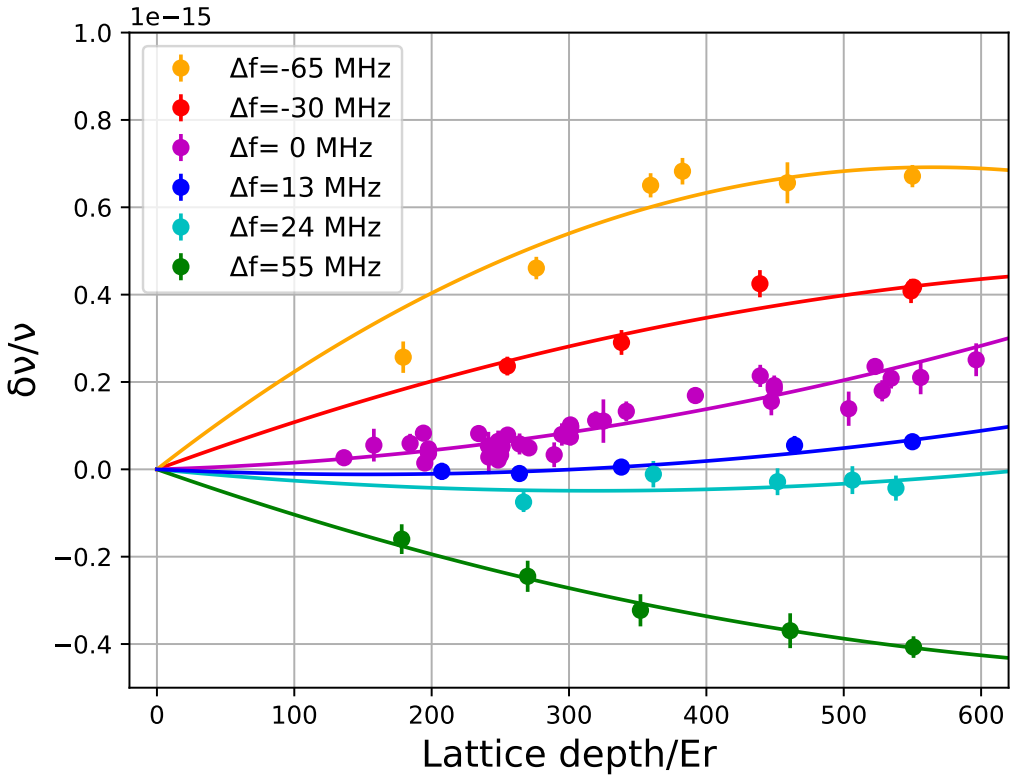

Fig. 3.13 Evaluation of the lattice shift as a function of the lattice depth and the lattice frequency. The legend reports the lattice frequency detuning from the true magic frequency calculated by Brown *et al.* [121]. The experimental data shown are corrected for the density shift.

point at 100 Er is expected to improve the clock performance with respect to previous evaluations [92]. From this analysis, the IT-Yb1 lattice shift at a lattice depth of 100 Er results to be $1.5(2) \times 10^{-17}$. We add to this value an uncertainty that we conservatively estimate to be 1×10^{-17}. This uncertainty derives from the deviation from the linear temperature dependence with the lattice depth, which is a requirement for the application of the theoretical model introduced by Beloy *et al.* that leads to Eq. 3.8.

To monitor the lattice frequency and manually correct for eventual drifts, a small portion of the lattice radiation is sent to an optical frequency comb (see Figures 2.2 and 2.10).

As we note from the accuracy budget of IT-Yb1 (see Table 3.1), the lattice shift

is one of the major contributions to the systematic fractional uncertainty of the clock. In the next few years, we will develop a new optical lattice clock with an accuracy budget characterized by an uncertainty below the 10^{-18} level. In the new apparatus, in order to reduce the lattice shift contribution, we plan to implement a cavity-enhanced lattice which will allow us to operate the clock at much higher lattice depths, enabling a more accurate characterization of the lattice shift and thus reducing its uncertainty.

3.4 Probe light shift

In the approximation of a two-level atom, the probe laser, being resonant, would not introduce any light shift to the clock transition. However, we have to calculate the light shift contribution that arose by considering all the Yb transitions involving one of the two clock states.
During the clock operation, the probe laser interacts with the atoms through a Rabi π pulse. Since for a π pulse, the required probe intensity scales as $1/t^2$, where t is the duration of the pulse, and given that the probe light shift induced on the clock transition depends on the probe intensity, it is convenient to operate the clock with the longer pulse duration possible. In our case, the Rabi pulse lasts 120 ms. We evaluate the probe light shift of IT-Yb1 starting from the value measured by McGrew *et al.* [9] rescaled for the duration of our Rabi pulse. The resulting light shift introduced by the probe laser for IT-Yb1 is thus conservatively evaluated as $\delta\nu_{\text{LS, probe}}/\nu = 4(3) \times 10^{-19}$.

3.5 Fiber links

As shown in Figure 2.2, the LO is distributed to different parts of the experiment through a polarization-maintaining fiber. Despite this, any variation in the path length caused by temperature fluctuations or mechanical stress can introduce a phase noise in the probe light that induces a shift in the clock frequency.
IT-Yb1 is provided with an active system for phase noise compensation [124, 125]. The setup allowing the compensation is schematized in Figure 3.14. The cancellation system consists of an interferometer that compares the signal propagating toward

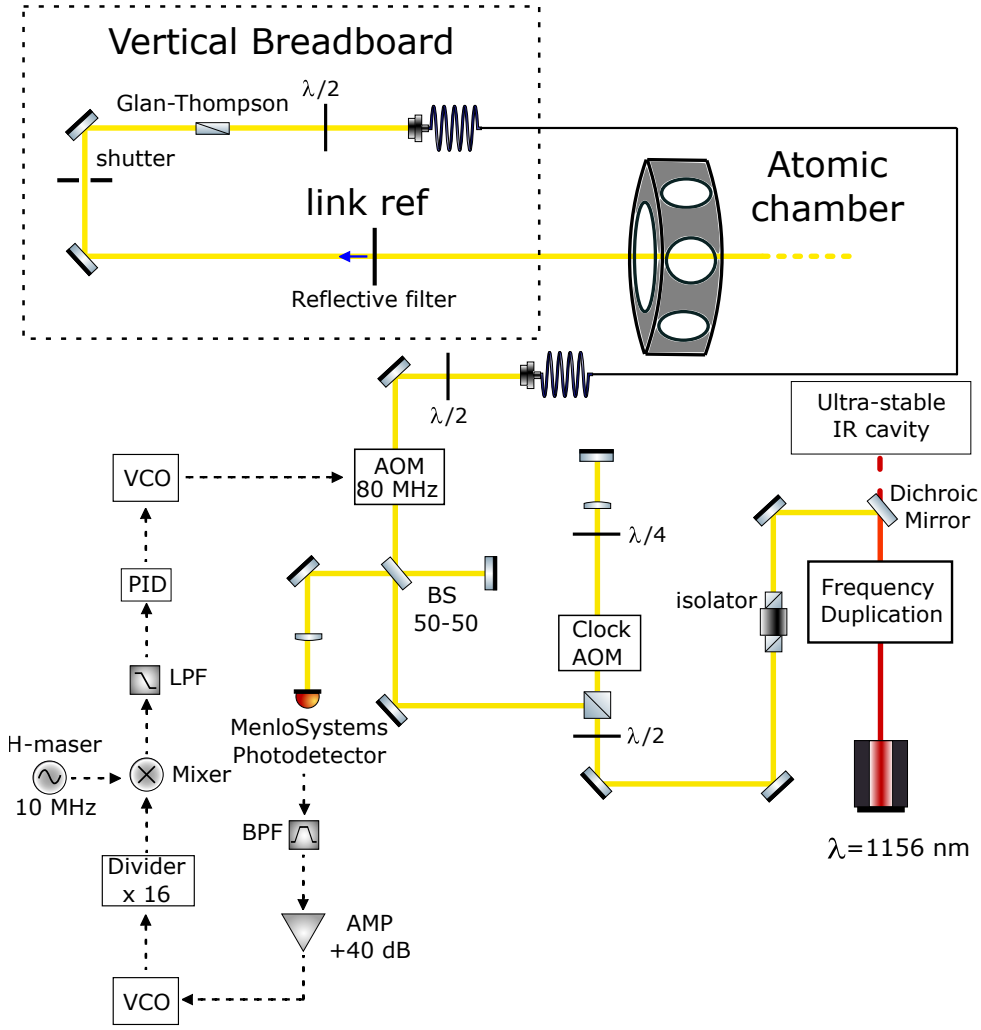

Fig. 3.14 Setup for the fiber noise cancellation. A portion of the probe light is collected on a fast photodiode before passing through an AOM and being coupled in the fiber. The remaining light propagates on the vertical breadboard toward the trapping region. A reflective filter that acts as a reference for the link retroreflects a small fraction of the probe power. The retroreflected light is then coupled back into the fiber and is collected on the photodiode. The resulting beat note signal is manipulated to obtain an error signal used to tune the AOM modulation and compensate for the fiber phase noise.

the atomic chamber with a reference signal collected before the fiber. A reflective filter is placed as close as possible to the atoms and retroreflects a small portion of the probe light that follows the same optical path in reverse and recombines with the reference signal. The light propagating along the long path double-passes an AOM modulated at 80 MHz, and the resulting beat note at 160 MHz is measured by the PD. The signal is then amplified, locked to the beat note input signal with a VCO to

avoid other noise sources, divided by a factor 16 and compared with a referenced signal at 10 MHz through a frequency mixer. The mixer output is thus proportional to the phase noise and is utilized as an error signal by a PID. The PID output is then used to tune the RF signal generated by a VCO that corrects the AOM modulation to compensate for the phase noise.
The fiber noise cancellation system has been tested for different positions of the link reference and by intentionally adding noise sources to the system. For example, mechanical vibrations are induced by a shutter located on the vertical breadboard.
By positioning the link reference on the vertical breadboard as close as possible to the atoms and considering a probe pulse of 120 ms, the cancellation system exhibits a shift consistent with zero, with an uncertainty of 1×10^{-18}.

3.6 Zeeman shift

An external magnetic field B induces an energy shift in the clock levels thanks to the well-known Zeeman effect. If the energy levels composing the clock transition are modified by a different amount, the clock frequency is affected by a systematic shift. The Zeeman shift can be described using the stationary perturbation theory and, in the weak coupling regime, i.e., for small magnetic fields, only the linear and the quadratic Zeeman effects are relevant.
The first-order term is the linear Zeeman effect and introduces an energy shift proportional to m_F. Consequently, in a Yb clock, the two π clock transitions $\left|m_F = \pm 1/2\right\rangle \rightarrow \left|m_F = \pm 1/2\right\rangle$ are shifted by the same quantity but with opposite signs. In particular, the linear Zeeman effect induces a shift in the two π transitions of $\Delta\nu_{\text{lin}} = \pm a_L B$ from the center. The coefficient a_L is the linear Zeeman coefficient, and for the Yb clock transition is $a_L = 1995.16(2)\,\text{Hz/mT}$ [9]. This coefficient is exploited to estimate the magnetic field at the atoms' position.
During the clock operation, the linear Zeeman shift is canceled by applying an external magnetic field to resolve the hyperfine structure, iteratively interrogating the two different π clock transitions and averaging the results [126, 9].
On the contrary, the second-order term has the same sign for both the π transitions and its contribution can not be canceled by the same procedure. Indeed, the quadratic Zeeman shift is $\Delta\nu_{\text{quad}} = a_{\text{Q}} B^2$, where the quadratic coefficient is $a_Q = -6.095(7)\,\text{Hz}/(\text{mT})^2$ [9]. Experimentally, it is more convenient to express

the quadratic coefficient as $a'_Q = a_Q/a_L^2$. For the Yb clock transition, a'_Q has been measured at RIKEN [127], NIST [9] and NMIJ [128]. Their results are in agreement, and we traditionally use the NIST value $a'_Q = -1.5311(18)\,\mu\text{Hz/Hz}^2$.
To correctly calibrate the magnetic field value in correspondence with the atomic sample position, it is necessary to take into account the lattice vector light shift [129]. The vector light shift is caused by a non-perfectly linear polarization of the optical lattice and depends on the lattice depth U. Its theoretical treatment is complex, but it can be described as an apparent magnetic field that introduces a frequency shift $\Delta\nu_{\text{vls}} \approx k_{\text{v}} cos(\theta) U$ [71], where θ is the angle between the external magnetic field B and the lattice propagation axis, and k_{v} is a factor that depends on the degree of the lattice elliptical polarization [130]. To reduce the vector light shift, it is necessary to operate the clock with a linear polarization of the lattice and to align the external magnetic field orthogonally to the lattice axis. However, the vector light shift introduces a systematic uncertainty in the splitting of the clock transitions, that for IT-Yb1 we conservatively estimate to be 0.4 Hz [92].
From these considerations, the typical Zeeman shift affecting IT-Yb1, for a bias magnetic field of about 5×10^{-5} T, is $-3.12(2) \times 10^{-17}$.

3.7 Blackbody radiation shift

Since IT-Yb1 operates at room temperature, the environment produces a thermal radiation called black-body radiation (BBR) that perturbs the clock transition. For an optical clock, it is possible to approximate the BBR shift as a static electric dipolar interaction corrected for a dynamic contribution η [106, 131]:

$$\delta\nu_{BBR} = -\frac{1}{2}\frac{\Delta\alpha^{(S)}}{h}\langle E^2\rangle_T (1+\eta(T)) \tag{3.10}$$

where h is the Plank constant, $\Delta\alpha^{(S)}$ is the differential scalar polarizability, and $\langle E^2\rangle_T$ is the time-averaged electric field generated by a black body at temperature T. For ^{171}Yb, $\Delta\alpha^{(S)} = h\times 3.626\,12(7) \times 10^{-6}\,\text{Hz}/(\text{V/m})^2$ [106] and $\eta(T = 300K) = 0.0180(4)$ [131]. Moreover, the average thermal electric field of a BBR environment at T is $\langle E^2\rangle_T = [8.319430(15)\text{V/cm}]^2 (T/300\text{K})^4$.
In our experiment, the two major sources of BRR are the vacuum package and the

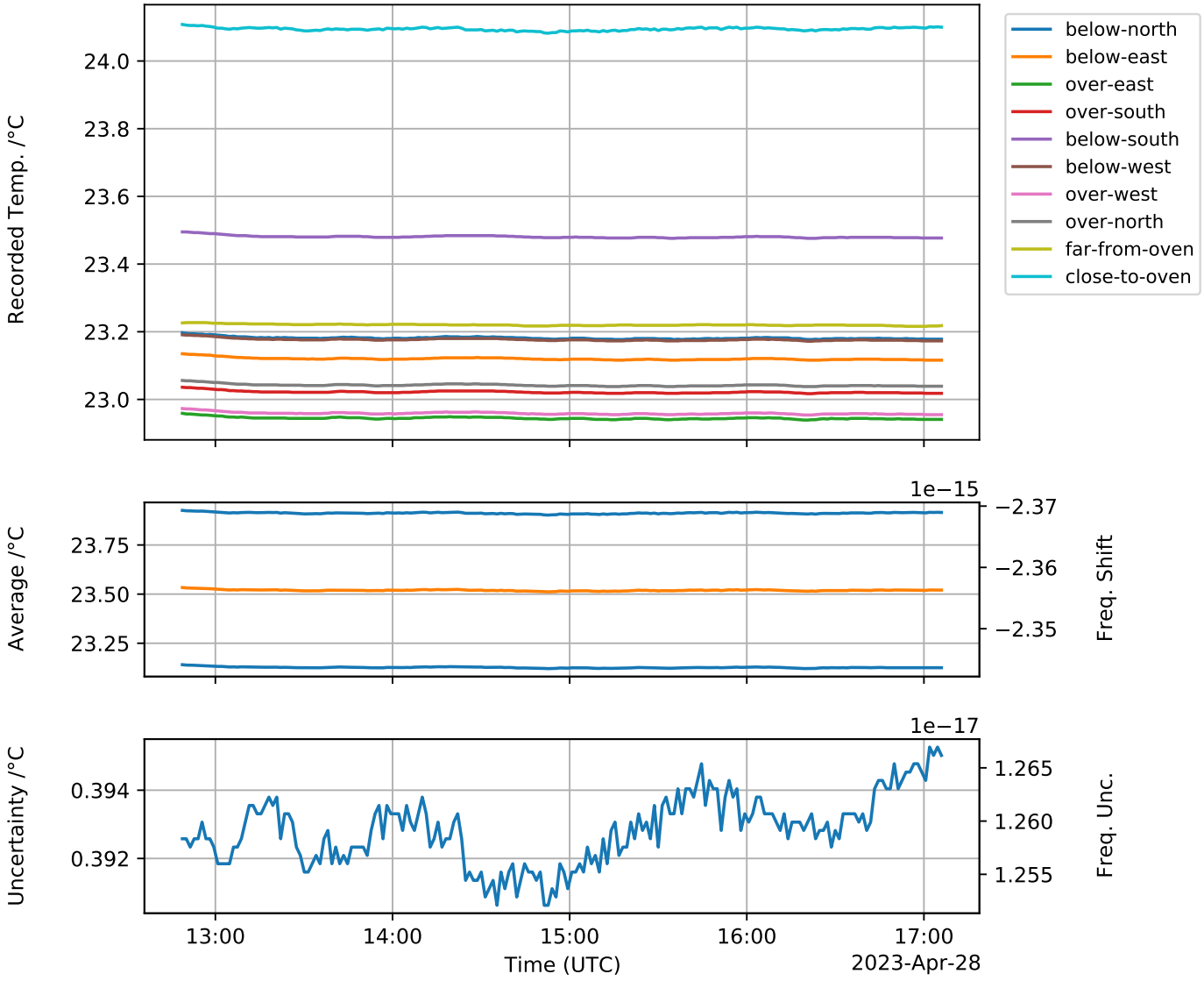

Fig. 3.15 Blackbody radiation monitor. The temperature of the atomic chamber is measured by 10 thermometers and plotted in the first panel as a function of time. The position of each sensor is reported in the legend. The second panel shows the average temperature and the corresponding BBR frequency shift. Finally, the third panel shows the temperature uncertainty and the relative frequency shift in units of 10^{-17}.

atomic oven.

BBR shift caused by environment

Ten platinum-resistance thermometers measure the temperature of the vacuum apparatus to evaluate its contribution to the BBR. Eight of them surround the main chamber, while the other two are placed near the atomic oven and very far from it. The temperature measured by the thermometers is shown in the first panel of Figure 3.15. The temperature is recorded every 80 s and the average temperature is evaluated for each clock data as $T = (T_{max} + T_{min}/2)$ where $T_{max/min}$ are the maximum and minimum temperatures recorded by the sensors. The uncertainty is $\sigma_T = (T_{max} - T_{min})/\sqrt{12}$, evaluated assuming a rectangular probability distribution between T_{max} and T_{min}. The average temperature and its uncertainty are shown in the second and third panels of Fig. 3.15, respectively. The BBR shift associated with a clock measure caused by the environment is then calculated by averaging the temperature associated with each data and its value typically is $\delta\nu_{room}/\nu = -234.9(12) \times 10^{-17}$.

BBR shift caused by the oven

A thermocouple (Thermocoax NiAl) is placed inside the oven package on the surface of the Yb reservoir to calculate the BBR shift caused by the oven. Its contribution to the BBR shift is then calculated through Eq. 3.10 rescaled by the effective solid angle of the oven radiation in the trapping region $\Theta/4\pi$. Given the geometry of our apparatus (the nozzle radius is about 2.5 mm and the distance from the atoms is about 20 cm), and considering a maximum of 3 reflections of the BBR radiation emitted by the oven before reaching the atoms, the solid angle measures $\Theta = 2.7(13) \times 10^{-3}$ sr. Therefore, by considering an oven temperature of 395 °C, the corresponding BBR shift is $\delta\nu_{oven}/\nu = -1.3(6) \times 10^{-17}$. The uncertainty is evaluated by considering the uncertainty associated with the solid angle Θ and with the oven temperature.

Considerations on the BB model: evaluation of systematic uncertainty

So far, we have considered that the atomic chamber acts as a perfect blackbody. However, it is possible to evaluate the uncertainty introduced by this model, by assuming that the atomic chamber is not a perfect blackbody with emissivity $\varepsilon \neq 1$. In this case, the effective temperature seen by the atoms T_{a} is [132, 133]:

$$T_{\mathrm{a}}^4 = \frac{\Theta T_{\mathrm{oven}}^4 + \varepsilon(4\pi - \Theta) T_{\mathrm{r}}^4}{\Theta + \varepsilon(4\pi - \Theta)} \tag{3.11}$$

where T_{oven} is the temperature of the oven seen by the atoms and T_{r} is the temperature of the atomic chamber that is at room temperature (about 23 °C). The first term of the numerator accounts for the radiation emitted by the oven, and the second term for the radiation emitted by the atomic chamber. The denominator is composed of both the radiation lost by the atoms and the atomic radiation reflected by the chamber and reabsorbed. The contribution of the radiation emitted by the oven and reflected by the atomic chamber is negligible given the geometry of the atomic chamber. Figure 3.16 shows the increment in the effective temperature seen by the atoms with respect to the perfect BB case, as a function of the emissivity of the atomic chamber ε. For this calculation, the oven temperature is $T_{\mathrm{oven}} = 400\,^{\circ}\mathrm{C}$. From this simple simulation we can note that even considering a very low emissivity of the atomic chamber $\varepsilon = 0.1$, the temperature seen by the atoms increases only by about 0.45 °C, which corresponds to a variation of the BBR shift of about -1.4×10^{-17}, a value comparable with the uncertainty associated with $\delta\nu_{room}/\nu$. In addition, given the geometry of the atomic chamber and the presence of several windows that can be approximated to a blackbody, the emissivity of the atomic chamber is higher than the value here considered $\varepsilon = 0.1$. In particular, for emissivity $\varepsilon > 0.5$, the systematic uncertainty arising from considering the atomic chamber a perfect blackbody is lower than 1×10^{-18}, and it is negligible.

For IT-Yb1, the BBR shift generated by the environment and the oven represents the greatest contribution to the systematic uncertainty of the accuracy budget (see Table 3.1). To avoid this source of uncertainty in the next optical lattice clock we are designing, we plan to increase the thermal uniformity of the atomic chamber. In particular, the atomic chamber will be painted with a black matte coating [134] to increase its emissivity. Moreover, the thermal sensors will be finely calibrated to

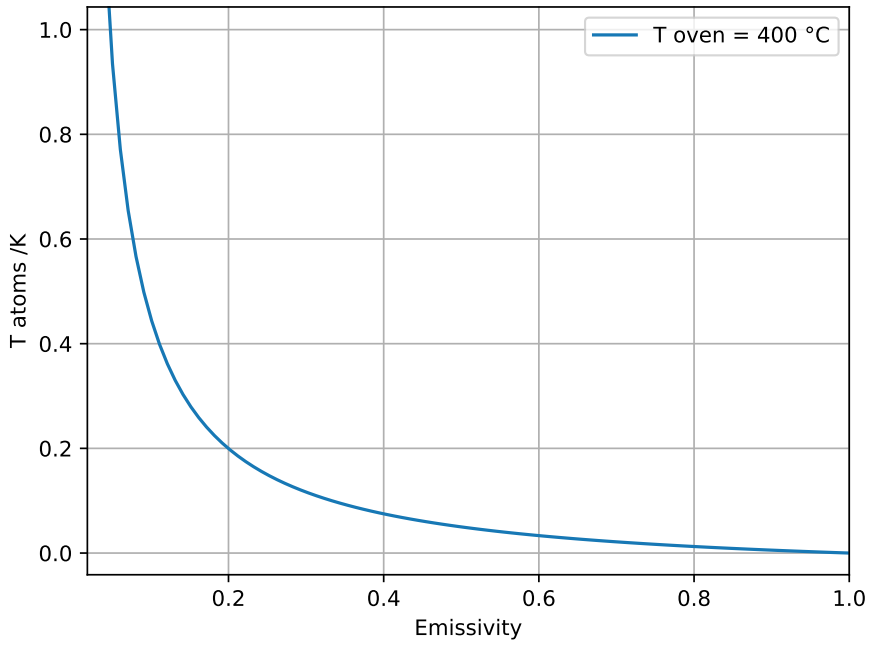

Fig. 3.16 Increase in the temperature in correspondence of the atomic sample as a function of the emissivity ε of the atomic chamber. In this simulation, the oven temperature is $T_{\text{oven}} = 400\,^{\circ}\text{C}$ and the solid angle $\Theta = 2.7 \times 10^{-3}$ sr.

reduce the uncertainty associated with the temperature measurement. Finally, we will implement a new vacuum system apparatus provided with two atomic chambers [135, 136]. The first one will be used for the initial stage of atomic cooling, while the second one will host the atomic loading in the lattice and the clock interrogation. In this way, the atomic oven will not be in line-of-sight of the probing region, and the BBR shift caused by the oven will be suppressed.

3.8 Background gas shift

The background gas is a residual gas in the vacuum chamber composed of hot Yb atoms that are not trapped in the lattice and of H_2 molecules released by the inner surface of the atomic chamber. The background gas particles may interact with the cold Yb atoms pushing them out of the lattice. If a trapped atom is not ejected from the lattice after a collision with the background gas, it induces a shift in the

clock frequency. The background gas shift is inversely proportional to the atomic lifetime in the lattice [137, 9]: $\delta\nu_{bkg}/\nu = a/\tau$. The proportional coefficient a we utilized to evaluate the shift is derived by combining the long-range interaction coefficients C_6 [137, 138] theoretically calculated for Yb-Yb interactions [139] and Yb-H_2 interactions [78]. It results to be $a = -1.6(3) \times 10^{-17}$ s.

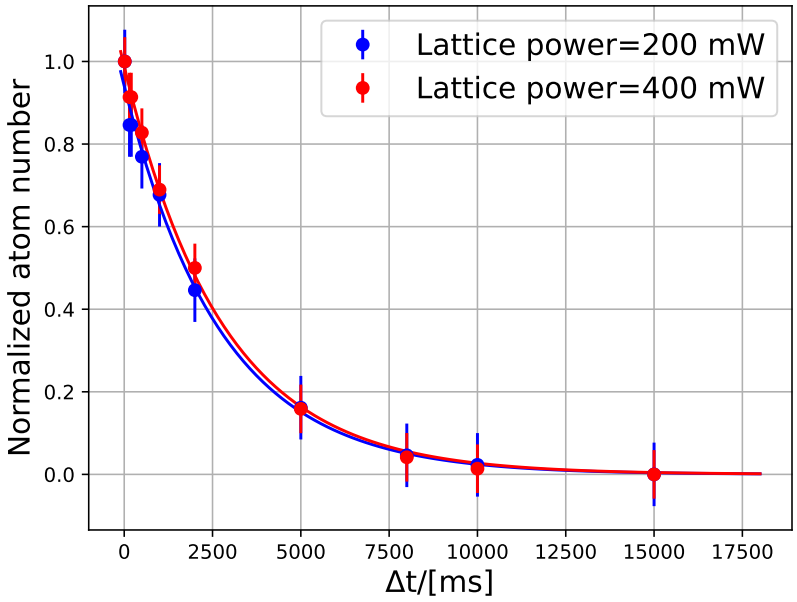

Fig. 3.17 Measurement of the ground state atomic lifetime in the lattice. Red dots represent experimental data taken with a lattice power of 200 mW that corresponds to the usual working point of the clock. The blue data instead are measured with a lattice power of 400 mW. Data are fitted with an exponential decay function (solid lines), and the lattice lifetime for the two data sets is consistent and results to be $\tau = 2.7(5)$ s.

The lifetime of ground state Yb atoms in the lattice is evaluated by loading the atoms in the lattice and measuring the ground state population with a detection pulse after a variable holding time Δt. The result of this experiment is shown in Figure 3.17 and corresponds to an atomic lifetime of $2.7(5)$ s. By combining the lifetime value and the proportional coefficient a, we calculate the background gas shift as $\delta\nu_{bkggas}/\nu = -0.5(2) \times 10^{-17}$.

A possible strategy to reduce the background gas shift and increase the atomic lifetime in the lattice would be to modify the whole vacuum setup to not have the oven in line-of-sight of the interrogation region. This is possible in a configuration with two vacuum chambers [135, 140, 141, 136], where the first one is used to trap

the atoms in a first-stage blue MOT, and the second one is used for the atomic loading in the lattice and the clock interrogation.

3.9 Tunneling

The atoms trapped in an optical lattice can move from one lattice site to the adjacent one thanks to the quantum tunneling effect. This process occurs when the energy structure of the two sites is the same. The tunneling effect results in a broadening of the lattice band structure [142] that can worsen the clock accuracy. However, the tunneling effect is suppressed by orienting the lattice along the vertical direction [142]. Indeed, in this case, the total external potential is the combination of the lattice potential and the gravitational potential. The eigenstates of such accelerated lattice potential are the Wannier-Stark states [143], and the presence of the gravitational potential lifts the degeneracy between energy levels of two neighboring sites. It is possible to demonstrate that for typical lattice depths and timescale of the interrogation duration utilized in optical lattice clocks, the gravitational potential strongly inhibits the tunneling effect [142]. Since the lattice of IT-Yb1 is vertical, the tunneling shift is negligible and is not taken into account in the evaluation of the clock uncertainty budget.

3.10 Servo error

During the clock operation, the LO frequency is locked to the half-maximum points of the Rabi line (see Section 2.5.4), which are frequency detuned from the resonance value ν_0 by $\nu_{lock} = \pm\gamma/2$. After each clock cycle, the stabilization control loop applies a correction $\Delta\nu_{corr}$ to the LO frequency to keep it resonant with the atomic reference. The servo error shift is the average LO frequency detuning from the atomic resonance: $\Delta\nu_{servo} = \langle\nu_{LO}\rangle - \nu_0 = \langle\nu_0 \pm \nu_{lock} + \Delta\nu_{corr}\rangle - \nu_0 \simeq \langle\Delta\nu_{corr}\rangle$. Thanks to a slow control loop that compensates for LO ultrastable cavity drifts, the servo error shift is consistent with zero with a relative uncertainty of 3×10^{-18}.

3.11 AOM switching

The AOM switching shift arises from the inhomogeneity in the probe frequency induced by clock AOM (see Fig. 2.2). If the clock AOM is switched on and off by changing the RF power, it induces in the AOM crystal a thermal gradient that causes a phase shift in the probe light. To avoid this effect, we keep the clock AOM always on and we change the RF frequency instead. Indeed, the clock AOM receives an RF signal that keeps the probe light resonant (ν_0) with the clock transition during the interrogation and off-resonant (ν_1) otherwise. The frequency switching introduces a smaller phase shift in the probe light than the power switching, and the consequent systematic frequency shift is at the level of 10^{-18}. However, since the probe radiation then propagates through the fiber noise cancellation system (Sec. 3.5), the AOM frequency switching results in a phase jump [144]. Indeed, the phase variation occurs in shorter times than required for the light to propagate in the long branch of the optical setup for the phase compensation (see Figure 3.14). As a consequence, the detected phase difference is compensated even though it is not due to real phase noise.
In IT-Yb1, also this later effect is suppressed by alternating two different values $\nu_1 \pm \delta\nu_1$ with respect to resonance. The resulting frequency shift is thus null, with an uncertainty of 1×10^{-18}.

3.12 Line pulling

The line pulling is an effect due to the presence of atomic transitions close to the clock frequency. Indeed, the convolution of nearby transitions and the clock transition results in a shift of the clock line. Considering a Yb clock, the contributions to the line pulling arise from transitions between different hyperfine states of the clock levels or from lattice sidebands transitions. The line pulling shift generated by the hyperfine structure is suppressed by making the probe polarization linear with a Glan-Thompson polarizer and by optimizing the spin-polarization process. Indeed, in this way, only one sublevel of the clock ground state is populated, and only the π transition is allowed.
Moreover, since the lattice sidebands are symmetric, their contribution to the line

pulling is opposite [145] and the net shift is strongly suppressed. The resulting line pulling shift for IT-Yb1 is thus zero, with an uncertainty lower than 2×10^{-19}.

3.13 Gravitational redshift

As we all know, a gravitational potential affects the frequency of a clock [146]. This effect is called gravitational redshift and has to be considered in a clock frequency measurement. Indeed the gravitational potential of the Earth is sufficient to introduce a frequency shift of the order of $1 \times 10^{-16}\,\mathrm{m}^{-1}$ that depends on the height Δh between the clocks and the geoid.
In 2018 the General Conference on Weights and Measures (CGPM) conventionally adopted as equipotential the value $W_0 = 62\,636\,856.0\,\mathrm{m}^2/\mathrm{s}^2$ [147]. Therefore, to characterize a clock, it is necessary to evaluate the gravitational redshift with respect to this reference. Moreover, when comparing two optical clocks, it is crucial to evaluate the gravitational redshift at the level of 10^{-18} to not deteriorate the accuracy achieved by optical frequency standards. This is possible by measuring the difference in gravitational potential between the positions of the atoms in the two experiments with an uncertainty of $0.1\,\mathrm{m}^2/\mathrm{s}^2$, that corresponds to an uncertainty in Δh at the cm level [45].
The gravitational potential of the laboratory hosting IT-Yb1 (W_{IT-Yb1}) has been measured as part of the International Timescales with Optical Clocks (ITOC) project through the Global Navigation Satellite System (GNSS)/geoid method. This approach combines geoid field modeling with GNSS techniques for measuring the clock position. The corresponding gravitational redshift affecting IT-Yb1, calculated with respect to the equipotential W_0, is $\delta\nu/\nu_{redshift} = 2599.5(3) \times 10^{-17}$ [92].

Chapter 4

Measurement campaigns: local and remote absolute frequency measurements

Once an atomic clock is operating and characterized, its frequency can be measured against other clocks. In particular, the absolute frequency measurement of a clock is obtained through a comparison with the frequency of a Cs primary standard. Otherwise, it is possible to measure the frequency ratio of two optical clocks.
The absolute frequency of an optical transition is usually measured by direct comparison with a Cs fountain. In this case, the frequencies of the optical clock LO and that of the H-maser calibrated by the Cs clock are measured by the same frequency comb. This method is feasible only when the optical clock and the Cs fountain are simultaneously available and operative. An alternative method to measure the absolute frequency of an optical transition does not require a Cs clock and is based on the measured frequency of the SI second through a link to the International Atomic Time (TAI) [148]. Indeed, the optical frequency can be measured by a frequency comb relative to the signal of a local H-maser that is continuously compared with TAI via GNSS or other microwave techniques.
Since the performances of an optical clock are nowadays orders of magnitude better than those of a primary standard, the results of an absolute frequency measurement are usually limited by the uncertainty associated with Cs clocks. For this reason, optical frequency ratios represent a more effective experiment to assess the real performance of an optical frequency standard in terms of accuracy.

Another important distinction in clock comparisons is between local and remote measurements. Different techniques can be implemented to perform a ratio measurement between two atomic clocks that may be located in different places very far apart or even on different continents. The most performing comparison technique is a direct link via optical fiber. This method typically introduces an uncertainty in the frequency measurement at the level of 10^{-19}, one order of magnitude better than that associated with the best optical clocks [149–152]. Unfortunately, clock comparisons via fiber link are practicable only for intracontinental distances. For intercontinental distances, a clock comparison usually occurs via GNSS (Global navigation satellite system) [153, 154] techniques, but more recently intercontinental comparisons of optical clocks using the radioastronomy technique of VLBI (Very Long Baseline Interferometry) have been realized [155, 52]. However, both these two techniques are characterized by a larger uncertainty of about 10^{-16}.
Frequency comparisons are thus a powerful tool to assess the performance of a clock and determine its reliability. In fact, by comparing the absolute or ratio frequency results of several clocks based on the same atomic species, it is possible to evaluate their consistency and assess the robustness of such frequency standards.
Moreover, as explained in Section 1.1, frequency comparisons represent a fundamental step towards the redefinition of the SI second. Indeed the redefinition requires both absolute frequency measurements of optical standards against Cs fountain with a fractional uncertainty $\Delta\nu/\nu < 3 \times 10^{-16}$ and optical frequency ratio with a better agreement than $\Delta\nu/\nu < 5 \times 10^{-18}$ [14].

The absolute frequency of the Yb clock transition has been realized by several metrological institutes worldwide in the last year: in particular, by NIST [156, 9], NMIJ [157–159], KRISS [160–162] and ECNU [163]. Moreover, at INRiM the absolute frequency of IT-Yb1 has been measured in 2016 against the Italian primary frequency standard IT-CsF2 [68] and via TAI [92] from October 2018 to February 2019. Furthermore, in 2016 an optical frequency ratio was also performed between ^{171}Yb and ^{87}Sr with a transportable optical Sr clock developed at PTB [46] and via VLBI in collaboration with NICT INAF and BIPM [164].
During the years of my Ph.D., IT-Yb1 participated in two important international projects. First, in December 2021, our clock has been measured against the Yb clock developed at KRISS via VLBI. Second, in March 2022, IT-Yb1 participated in the ROCIT campaign: an international comparison involving 11 optical clocks in 7

countries in Europe and Japan. The results of these two campaigns are still under analysis, and I will briefly present them in the conclusive Chapter of this thesis.
In this Chapter, I describe the measurement campaigns we performed and finalized during my Ph.D. and I present their results. In particular, Section 4.1 describes the local absolute frequency measurement of IT-Yb1 against IT-CsF2. After that, in Section 4.2, I illustrate the results obtained through a remote comparison between IT-Yb1 and the French Cs fountain developed at SYRTE.

4.1 Local absolute frequency measurements: IT-Yb1 vs IT-CsF2

In the last two years, and more precisely from June 2021 to September 2022, we performed an absolute frequency measurement of IT-Yb1. The result of this local absolute frequency measurement has been recently published on Metrologia [33].
In this campaign, the frequency of our Yb clock has been measured against the cryogenic Cs fountain IT-CsF2, the primary standard developed in INRiM that is into operation since 2013. The details of IT-CsF2 have been described by Levi *et al.* in [4]. A picture of IT-CsF2 is shown in Figure 4.1.

During the measurement campaign, IT-Yb1 has shown a typical instability of $2 \times 10^{-15}/\sqrt{\tau/s}$ and a systematic uncertainty of $\delta\nu/\nu = 1.9 \times 10^{-17}$ given by systematic effects summarized in the accuracy budget described in the previous Chapter of this work and summarized in Table 3.1.
In the same time period, IT-CsF2 has been characterized by an instability of about $2.6 \times 10^{-13}/\sqrt{\tau/s}$ and an uncertainty budget with a total relative shift of $\delta\nu/\nu = 2.3 \times 10^{-16}$ (see [33] for details).
The frequency of the two clocks is compared through an optical frequency comb, also located in our research institute, that added to the uncertainty of the frequency measurement a contribution of the order of 10^{-17}.

Measurement chain

During this campaign, the frequency of IT-Yb1 has been measured with two different techniques that are schematically represented in Figure 4.2.

Fig. 4.1 Picture of IT-CsF2: the Italian cryogenic Cs fountain.

The measurement chain indicated with blue arrows represents the method usually implemented when a clock frequency is measured against a Cs primary standard. In the following, I will refer to this technique as the "H-maser chain". The Yb clock transition is interrogated with the radiation at 1156 nm that is frequency stabilized to the ultrastable cavity and frequency doubled to be resonant with the atomic transition. A fraction of this radiation is sent to a fiber frequency comb (Comb 2 in Figure 4.2), which is stabilized to the H-maser system utilized to interrogate the Cs transition. The frequency comb thus measures and compares the frequency of the local oscillator of the two clocks, and it is possible to obtain the IT-Yb1/IT-CsF2 ratio.
On the contrary, the paths illustrated in Figure 4.2 with orange arrows is the "Optical Microwave chain": a new measurement technique tested during this campaign. Similarly to the H-maser chain, in the Optical Microwave chain, the Yb clock transition is probed with a stabilized radiation at 1156 nm that is measured by an optical frequency comb. But in this case, the frequency comb (Comb 1 in Figure 4.2) is referenced to the radiation at 1156 nm and the spectral properties of the ultrastable

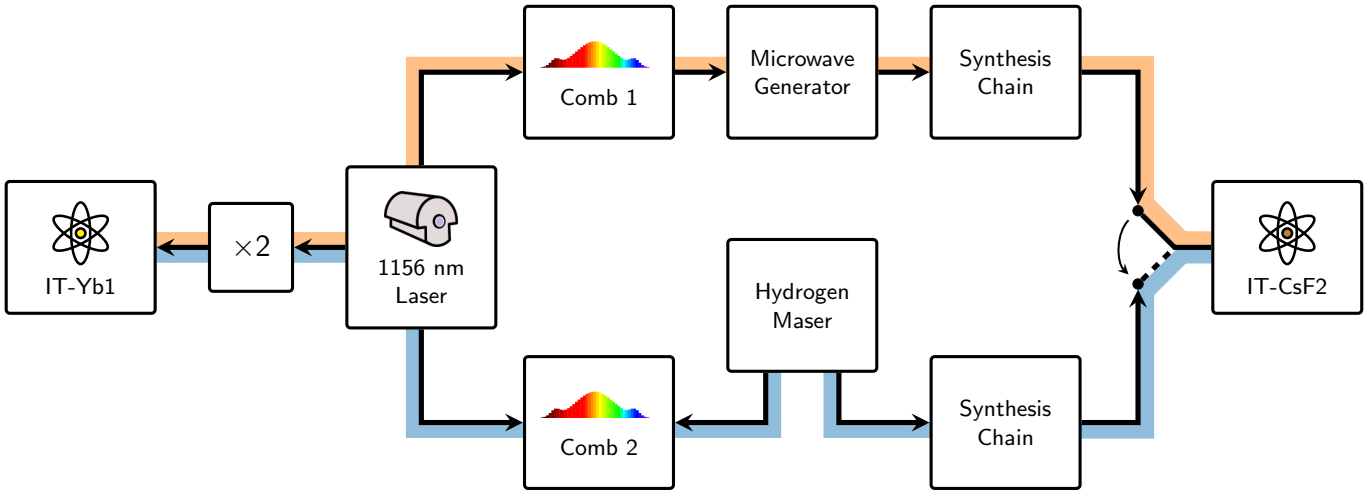

Fig. 4.2 Scheme of the experimental setup utilized to measure the absolute frequency of IT-Yb1 during the campaign, adapted from [33]. Both techniques implemented to carry out this measurement are illustrated: the blue path represents the H-maser chain, while orange arrows show the Optical Microwave chain (see main text for details).

laser are transferred to the frequency comb by a phase-locking scheme similar to that introduced by Millo *et al.* in Ref. [165]. Then, the pulse train generated by Comb 1 is used to obtain a microwave radiation [165, 166] resonant with the Cs clock transition. In particular, by selecting and amplifying the 40th harmonic of the repetition rate of the comb, a signal at 10 GHz is obtained. After that, a microwave of 9.2 GHz is produced by mixing the input 10 GHz signal with a second RF signal at 800 MHz, obtained in turn by downscaling the initial signal at 10 GHz. Finally, the 9.2 GHz signal is kept resonant with the Cs transition by mixing to a DDS (direct digital synthesis) at about 7.4 MHz. The DDS frequency is adjusted every clock cycle to guarantee the resonance of the microwave with the atomic transition. The process of microwave generation, as well as the synthesis chain, is characterized by a flicker phase noise at the level of $-105\,\mathrm{dBc/Hz}$ and $-106\,\mathrm{dBc/Hz}$, respectively. These two contributions result in an instability of 5×10^{-16}.

Results

For this measurement campaign, we collected IT-Yb1 and IT-CsF2 data from June 2021 to September 2022 for a total common uptime between the two clocks of 32 days and 6.9 days using the H-maser chain and the Optical Microwave chain, respec-

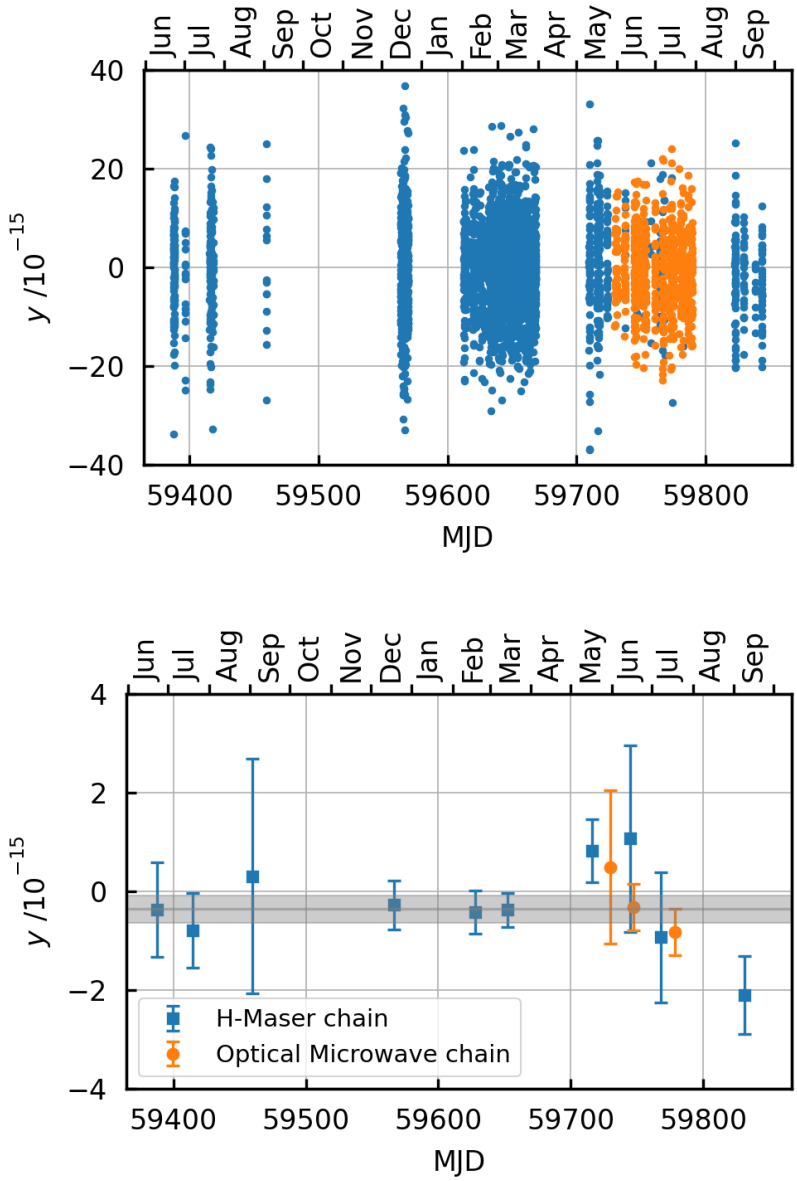

Fig. 4.3 Experimental data of the fractional frequency ratio between IT-Yb1 and IT-CsF2 calculated as $y = r/r_0 - 1$ as a function of time expressed in MJD. The acquisition period lasts from June 2021 to September 2022. Data acquired by using the H-maser chain are reported in blue, while data collected with the Optical Microwave chain are shown in orange. The top panel shows averaged data in 864 s bins, while the bottom panel shows the same data averaged monthly. The uncertainty associated with each data includes the contribution of the systematic uncertainty of the two clocks. The shaded grey area represents the average fractional frequency ratio evaluated over the entire campaign.

tively. The data from the combs and the Yb clocks are recorded with a sampling time of 1 s, while the Cs clock is sampled at 864 s, independently from the measurement chain (H-maser or Optical Microwave) used. For this reason, to combine the data from the two clocks, the data from IT-Yb1 and optical combs are previously averaged in bins with a duration of 864 s. The top panel of Figure 4.3 shows the data collected in 864 s bins reported as fractional frequencies $y = r/r_0 - 1$, where r is the measured frequency and r_0 is a reference frequency that, for this analysis, we choose to be the recommended value for the secondary representation of the SI second for the Yb transition established by CCTF in 2021 [167], i.e., $r_0 = 518\,295\,836\,590\,863.63\,\text{Hz}$, with an uncertainty of 1.9×10^{-16}. The introduction of the fractional frequency ratio y allows the linearization of equations and avoids computational problems due to numbers with many digits [168]. The bottom panel of Figure 4.3 shows the same data but averaged monthly, and the shaded area represents the average fractional frequency ratio between Yb and Cs and its uncertainty evaluated over the entire campaign. The average fractional frequency ratio between IT-Yb1 and IT-CsF2 measured with the two measurement chains is:

$$y(\text{IT-Yb1/IT-CsF2, H-maser chain}) = -3.8(2.9) \times 10^{-16}$$
$$y(\text{IT-Yb1/IT-CsF2, Optical Microwave chain}) = -3.2(3.7) \times 10^{-16}$$

The weighted average of the measurement is:

$$y(\text{IT-Yb1/IT-CsF2}) = -3.6(2.7) \times 10^{-16}$$

that corresponds to an absolute frequency of Yb:

$$f(\text{IT-Yb1}) = 518\,295\,836\,590\,863.44(14)\,\text{Hz}$$

It is important to note that, with its fractional uncertainty of 2.7×10^{-16}, this is the absolute frequency measurement of the Yb transition with the lowest fractional uncertainty ever achieved.

This frequency comparison instability over the entire campaign is shown in Figure 4.4 as the overlapped Allan deviation. In particular, blue squares represent the instability of the comparison between IT-Yb1 and IT-CsF2 measured with the H-maser chain, which results to be $2.7 \times 10^{-13}/\sqrt{\tau/s}$. On the contrary, the insta-

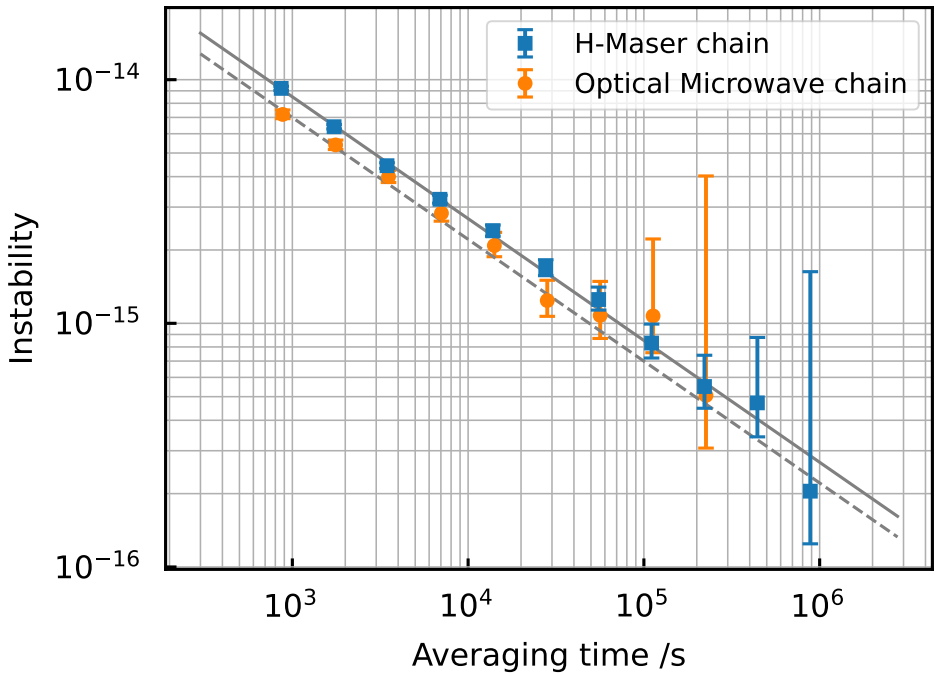

Fig. 4.4 Instability of the comparison over the full campaign expressed as Overlapping Allan deviation. The blue squares represent the instability of the comparison measured with the H-maser chain, while the orange circles describe the instability of the measurement performed with the Optical Microwave chain. The solid and dashed lines show the instabilities calculated as white frequency noise at $2.7 \times 10^{-13}/\sqrt{\tau/s}$ and $2.1 \times 10^{-13}/\sqrt{\tau/s}$, respectively.

bility of the comparison measured with the Optical Microwave chain is shown in orange circles and it is $2.1 \times 10^{-13}/\sqrt{\tau/s}$. The improvement in the stability of the comparison achieved with the Optical Microwave chain is due to the lower phase noise of the optically-generated microwave compared to that associated with the H-maser system. Indeed, as anticipated in Section 1.2, one of the major limitations of the clock stability is the Dick effect of the LO. In the case under discussion, the Dick effect of the LO produced with the H-maser system is $1.6 \times 10^{-13}/\sqrt{\tau/s}$, while we estimated a contribution of the Dick effect of the optically-generated microwave at the level of $3 \times 10^{-15}/\sqrt{\tau/s}$. However, by observing Figure 4.4 we note that the improvement in the comparison instability is not as significant as expected. This is due to the atomic background noise of the Cs fountain, an effect that deteriorates the measurement stability.

From Figure 4.4 and considering the total measurement uptime achieved with the two different techniques, it is possible to evaluate the statistical contribution of the com-

parison uncertainty, which is 2.8×10^{-16} for the Optical Microwave measurement and 1.6×10^{-16} for the H-maser chain. As a consequence, we can conclude that, with more than one year of data, the statistical uncertainty limited by the Cs fountain instability is lower than the systematic uncertainty of IT-CsF2 at 2.3×10^{-16}, that is the limiting contribution to this absolute frequency measurement of Yb. The systematic uncertainty of IT-Yb1 is 1.9×10^{-17} and is negligible, as well as the uncertainty associated with the optical combs and microwave generation.

4.2 Remote frequency measurements: IT-YB1 vs FO2

In December 2021, the frequency of IT-Yb1 has been measured against the microwave fountain FO2 developed at SYRTE, the national metrology institute of France, located in Paris. This clock comparison was possible thanks to the optical fiber link that connects INRiM and SYRTE, the two metrological institutes involved in this measurement campaign. A detailed description of the optical fiber link and its characterization is reported in a paper, published last year in Phys. Rev. Applied [150].
The atomic clock FO2 is a dual microwave fountain that can operate with both Cs and Rb atoms simultaneously [1, 169]. FO2 has thus a twofold nature: it is a primary frequency standard (FO2-Cs) and a secondary representation of the second based on ^{87}Rb atoms (FO2-Rb). The local oscillator of this fountain is a cryogenic sapphire oscillator phase-locked to an H-maser, and it provides a stability of $3.2 \times 10^{-14}/\sqrt{\tau/s}$ for FO2-Cs and of $2.9 \times 10^{-14}/\sqrt{\tau/s}$ for FO2-Rb. Both these two fountains have a systematic uncertainty between 2×10^{-16} and 3×10^{-16}. As a consequence, the systematic uncertainty becomes dominant after about 3 days of measurement.
In addition, also the Italian primary frequency standard IT-CsF2 (already introduced in the previous Section) took part in this measurement campaign. During the period of operation of IT-Yb1, IT-CsF2 has shown an instability at the level of $3.2 \times 10^{-13}/\sqrt{\tau/s}$ and a systematic uncertainty of 2.4×10^{-16}.

Italy-France fiber optical link

A schematic representation of the optical fiber link connecting INRIM in Torino and

SYRTE in Paris is shown in Figure 4.5.

Fig. 4.5 Sketch of the European network of optical fiber links, adapted from [150]. The SYRTE-INRIM branch is highlighted as a thick line. In blue is illustrated the French REFIMEVE network, while in red is represented the Italian Quantum Backbone (IQB) network. The scheme also shows the branches connecting SYRTE to two other European metrology institutes: NPL in the UK and PTB in Germany, indicated as yellow and green lines, respectively. White empty circles represent intermediate link terminals provided with a repeater laser station (RLS) or a multi-branch laser station (MLS).

It is a 1023 km long cascaded link, provided with an active stabilization system that utilizes the Doppler noise cancellation technique [125] similar to the one discussed in Section 3.5. The link between Paris and Torino is divided into 6 segments, with intermediate terminals provided with a repeater or multi-branch laser station (RLS or MLS) and represented in Figure 4.5 as white circles. Moreover, to compensate

for signal attenuation and to ensure a good signal-to-noise ratio, 11 bidirectional Erbium-doped fiber amplifiers are installed along the link.
The SYRTE-INRIM optical fiber link has been characterized over about 4 months, from 27th October 2021 to 24th February 2022. Over this entire period, the average uptime of the full link was 57%, with a maximum monthly uptime of 72% reached in January 2022. This high level of uptime is attainable since every intermediate station is provided with automated polarization controls and relock algorithms.
The uncertainty associated with the full link is below the 1×10^{-18} level [150], the same order of magnitude as state-of-the-art optical clocks, making this technique a powerful tool for optical clock comparisons.
This new link is located in a thriving European context. Indeed, the French National Research Infrastructure (REFIMEVE) is connected to both NPL and PTB [149] (yellow and green branches in Figure 4.5), thus making possible a totally optical comparison between optical clocks developed in these 4 NMIs. In addition, Torino is connected via the Italian Quantum backbone (IQB) fiber link to other institutes in Italy and reaches both the Matera Geodesy Centre and the Medicina radio-telescope, a part of the International Very Long Baseline Interferometry (VLBI) network.

Measurement chain

A scheme of the measurement chain utilized for this comparison is shown in Figure 4.6.
At SYRTE, a diode laser at 1542 nm is stabilized on a high-finesse optical cavity. Its frequency is continuously measured and steered to the local cryogenic sapphire oscillator by an optical frequency comb. Then the 1542 nm radiation is distributed through the stabilized fiber to INRiM, where the laser frequency is measured against the local H-maser by another optical frequency comb. The sapphire oscillator at SYRTE and the H-maser at INRiM also serve as local oscillators for FO2 and IT-CsF2, respectively.
The clock frequency of IT-Yb1 is interrogated by an ultrastable laser at 1156 nm that is frequency doubled to be resonant with the atomic transition. The LO frequency is continuously measured by the local frequency comb and compared to the 1542 nm signal disseminated by SYRTE via fiber link. Since the frequency comb can operate in a single branch configuration to measure both the 1156 nm and the 1542 nm radiation, its contribution to the measurement uncertainty is below 1×10^{-18}.

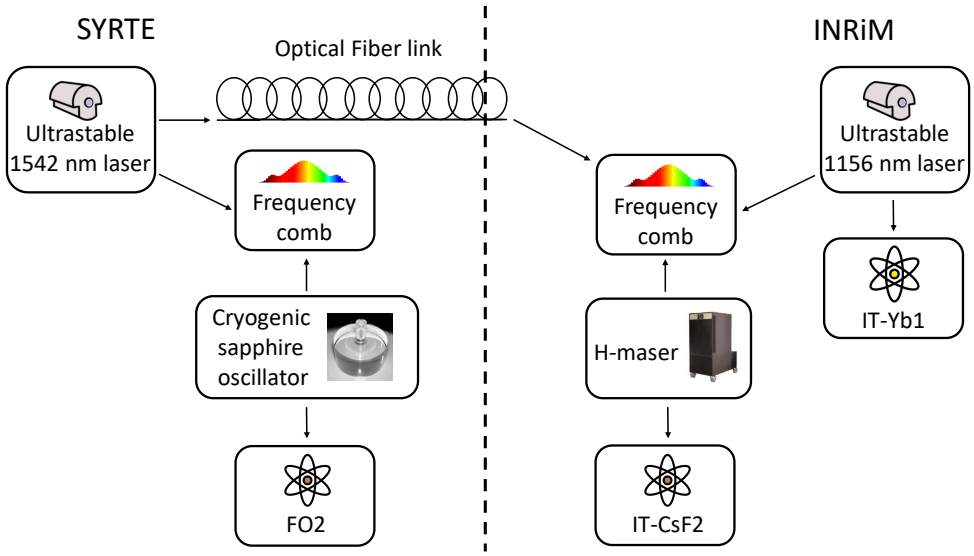

Fig. 4.6 Scheme representing the measurement chain for the clock comparison between SYRTE and INRiM. On the left side, the elements located at SYRTE are reported, while on the right side is shown the experimental setup developed at INRiM. The ultrastable laser at 1156 nm produced at SYRTE is disseminated toward Italy via the optical frequency comb.

Data collected in the two metrological institutes are analyzed by following the procedure described in [168]. First, to validate the fiber link, the frequency ratio of the two remote H-masers is evaluated by comparing the frequency measured by the two remote combs via the fiber link. It is thus possible to remove data affected by cycle slips or characterized by anomalous values. At this stage, the data acquisitions in different terminals are synchronized to better than 1 s. Then, validated data are averaged in bins of 864 s and are combined with the data of the fountain, which are sampled at 864 s. Finally, the comparison between two clocks is evaluated as fractional frequency ratio $y = r/r_0 - 1$ [168].

Results

For this comparison, IT-Yb1 operated for 7 days, from 15th to 21st December 2021. During this week, the optical clock showed an instability of $2 \times 10^{-15}/\sqrt{\tau/s}$ and a systematic uncertainty of 2.1×10^{-17}.
The instabilities of the two remote ratio measurements IT-Yb1/FO2-Cs and IT-Yb1/FO2-Rb, as well as that of the local frequency measurement IT-Yb1/IT-CsF2, are shown in Figure 4.7. The instabilities are dominated by the microwave fountains:

$4 \times 10^{-14}/\sqrt{\tau/s}$ for FO2-Cs and FO2-Rb, and $3.2 \times 10^{-13}/\sqrt{\tau/s}$ for IT-CsF2. The French fountain is characterized by a better instability than IT-CsF2 since its local oscillator is a cryogenic sapphire oscillator with a short-term instability almost one order of magnitude lower than that of the BVA quartz oscillator used for the local oscillator of IT-CsF2 [4]. The instability of IT-Yb1, calculated through an interleaved measurement, is $2 \times 10^{-15}/\sqrt{\tau/s}$ and results negligible. The Yb contribution to the instability is represented in Figure 4.7 as a red solid line.

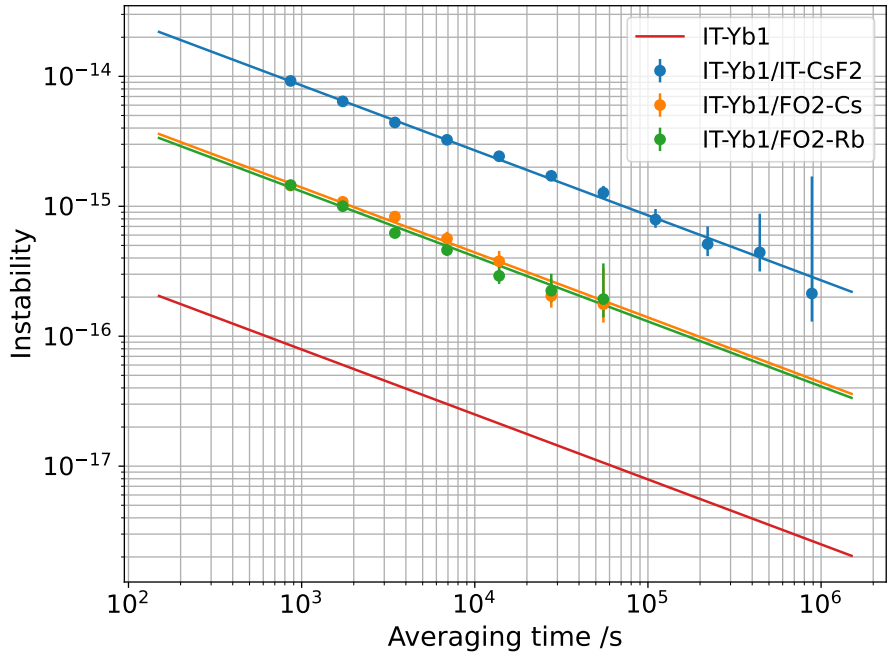

Fig. 4.7 Instabilities of the frequency ratio measurement between IT-Yb1 and IT-CsF2 (blue dots), FO2-Cs (yellow dots) and FO2-Rb (green dots), obtained as an overlapping Allan deviation. The solid lines represent the white noise contributions of the microwave fountains, which is $4 \times 10^{-14}/\sqrt{\tau/s}$ for FO2-Cs and FO2-Rb, and $3.2 \times 10^{-13}/\sqrt{\tau/s}$ for IT-CsF2. The red solid line represents the instability of IT-Yb1, calculated through an interleaved measurement.

The results of the frequency ratio measurement are calculated as $y = r/r_0 - 1$, where the reference ratios r_0 are calculated with the recommended values for the frequency of Rb and Yb established by CCTF in 2021 [167]. The results of ratios involving IT-Yb1 are summarized in Table 4.1, together with the different contributions (both statistical and systematic) to the total uncertainty u and the measurement time expressed in hours.

	$y/10^{-16}$	$u/10^{-16}$	$u_A/10^{-16}$	$u_{B,Yb}/10^{-16}$	$u_{B,mw}/10^{-16}$	Meas. time/h
IT-Yb1/FO2-Cs	-0.4	3.0	2.1	0.2	2.1	95
IT-Yb1/FO2-Rb	-4.2	3.2	1.9	0.2	2.5	95
IT-Yb1/IT-CsF2	-4.9	5.9	5.3	0.2	2.4	103

Table 4.1 Remote and local frequency ratio results expressed as y. u is the total uncertainty associated with the measurement, u_A is the statistical uncertainty, derived from the measured instability and dominated by the contribution of the microwave fountains, $u_{B,Yb}$ is the systematic uncertainty of IT-Yb1 and $u_{B,mw}$ is the systematic uncertainty of the microwave clock involved in the comparison. In the last column is indicated the total measurement time.

The corresponding absolute frequency measurement of Yb and ratio Yb/Rb are:

$$f(IT-Yb1)_{FO2-Cs} = 518\,295\,836\,590\,863.61(17)\,\text{Hz}$$
$$f(IT-Yb1)/f(FO2-Rb) = 75833.197545114168(24)$$
$$f(IT-Yb1)_{IT-CsF2} = 518\,295\,836\,590\,863.38(31)\,\text{Hz}$$

All these measurements are in agreement with the recommended values for the secondary representation of the second and with previous measurements of Yb [9, 33, 68, 92, 150, 156–163, 170], Rb [169] and their ratios [171, 159]. Moreover, this is the first ratio between Yb and Rb obtained with direct measurement and not through a link to TAI.

Notably, the remote frequency ratio measurements are characterized by a total uncertainty lower than the local one of about a factor 2, even though the systematic uncertainties are comparable and the measurement time is higher. This is due to the fact that the instability of the remote fountain is better than the one of IT-CsF2.

4.3 IT-Yb1 results in the international context

The two results of the Yb absolute frequency discussed in this chapter are reported in Figure 4.8 as red diamonds together with all the other Yb measurements ever performed in several institutes worldwide [9, 33, 68, 92, 150, 156–163, 170] represented as yellow or blue circles. It is worth noting that both the results of IT-Yb1

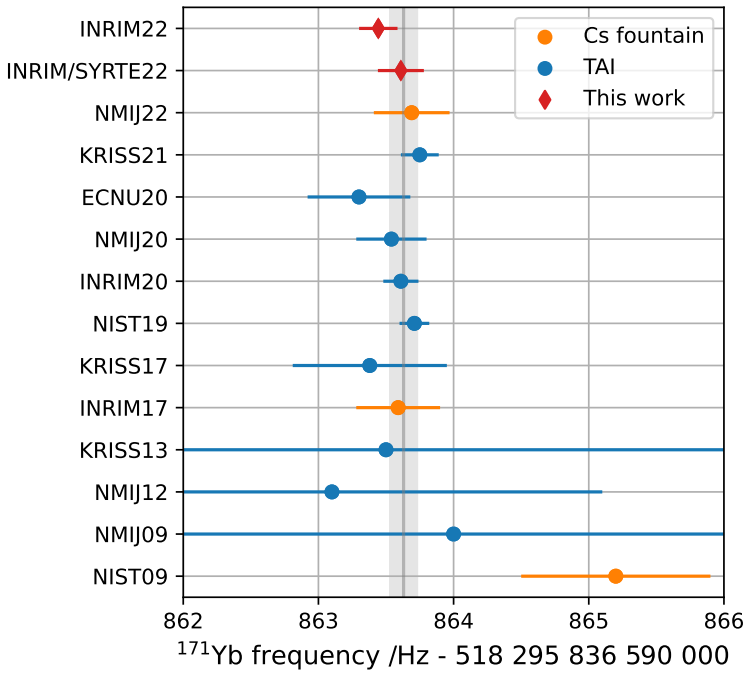

Fig. 4.8 Representation of all the absolute frequency measurements of the Yb clock transition performed in several metrological institutes and reported on the BIPM website [6]. Yellow circles represent the measure of Yb against a Cs fountain, while blue circles are the results of Yb frequency measurements obtained with a link to TAI. The results obtained in the last years with IT-Yb1 are shown with red diamonds. The grey solid line and the shaded area represent the recommended value of the Yb frequency and its uncertainty, respectively, both established by CCTF in 2021 [167]. The uncertainties here reported correspond to one standard deviation.

are in agreement with the recommended value of the Yb frequency given by CCTF and shown in Figure 4.8 as a grey solid line. Moreover, the absolute frequency performed at INRiM during the last year (INRIM22 in the vertical axis of Figure 4.8) is characterized by a lower uncertainty than the previous local measurement performed in 2017. It is also significant to observe that in the last 10 years, the uncertainty associated with Yb frequency measurements has been strongly reduced and that all the results are consistent with each other. This is a strong demonstration of the improvements achieved in the field of optical clocks and of the reliability of Yb as a frequency standard.

Chapter 5

IT-Yb1 contributions to TAI

As anticipated in the first chapter of this thesis, and in particular in Section 1.1, one of the requirements indicated by the CCTF for the realization of a new definition of the SI second based on an optical transition is the regular contribution of optical clocks to the steering of the International Atomic Time (TAI). As illustrated in Figure 1.7, TAI is produced by steering EAL (Échelle Atomique Libre) with the primary and secondary frequency standards (PSFS) of the contributing laboratories. The ten optical transitions that can contribute to TAI are those designed by the CCTF as a secondary representation of the second (SRS), represented in Section 1.1 and more precisely in Figure 1.3. It is important to recall that from TAI, the BIPM calculates UTC (Universal Time Coordinated), the most common time scale for everyday applications.
This chapter is organized as follows: in Section 5.1, I present the procedure for data submission to BIPM and for participating in the steering of TAI. Then, in Section 5.2, I provide an overview of IT-Yb1 contributions and finally in Section 5.3, I describe the improvement of optical clocks contributions to TAI over the past few years.

5.1 Frequency measurements for BIPM submission

To contribute to TAI, an optical clock has to submit to the BIPM the data of its frequency measurements against a clock that participates in the realization of EAL, such as a hydrogen maser. PSFS frequency data are sampled in intervals of 5 days, and the monthly computation may last 25, 30 or 35 days, depending on when the last

sampled interval ends. For real-time contribution to the steering of TAI, the PSFS data collected throughout the month have to be submitted to the BIPM within the 4th day of the following month. Then, at the beginning of each month, the BIPM calculates TAI and UTC using the data of PSFS collected over the previous month and submitted by the contributing labs.

It is interesting to point out that, before contributing to TAI, a frequency standard has to be approved by the Frequency Standard Working Group (WGFS) of the CCTF. To this purpose, it is necessary to provide at least one peer-reviewed publication with a description of the clock experimental setup and uncertainty budget, together with at least three initial measurements of the clock frequency against the referenced clock used for the computation of EAL. Once the performances of the clock are positively evaluated and if the results of these three measurements are consistent with TAI, the PSFS can contribute to the steering of the time scale. IT-Yb1 has been approved by the WGFS of CCTF in November 2019.

To participate in the computation of time scales, the frequency of the ultrastable clock laser of IT-Yb1 is measured against a local H-maser (IT-HM4) via a fiber frequency comb. The fractional frequency deviation y(IT-HM4/IT-Yb1) is calculated by considering as a reference the Yb frequency value recommended by CCTF in 2021. An example of the IT-Yb1 data submitted to the BIPM for the period MJD 59999-60034 (24 February 2023 - 31 March 2023) is shown in Figure 5.1. The data of the frequency comparison between the Yb clock and the H-maser are reported as blue dots, and the green regions in the bottom panel represent the uptime. Since IT-Yb1 operates intermittently, when the optical clock data are not available, it is necessary to use the H-maser as a flywheel for extrapolation [172, 173].

If the PSFS is considered reliable, the BIPM utilizes the submitted data to the computation of TAI and the results are reported in the Circular T. The Circular T is a monthly publication that contains the value of UTC and information about all the clocks that contributed to its evaluation. The Circular T is published on the BIPM website and is available to the public (https://www.bipm.org/en/time-ftp/circular-t). An example of the section of Circular T that reports the PSFS contribution for the steering of TAI is shown in Figure 5.2. Besides the code of the PSFS and the period of evaluation (MJD 59634-59669 for the Circular T in Figure 5.2), the value d is reported: the fractional deviation of the single clock measurement and the value of TAI for that month. In addition, the circular T provides the total uncertainty u as the quadratic sum of the five uncertainties u_A (the statistical uncertainty of the PSFS,

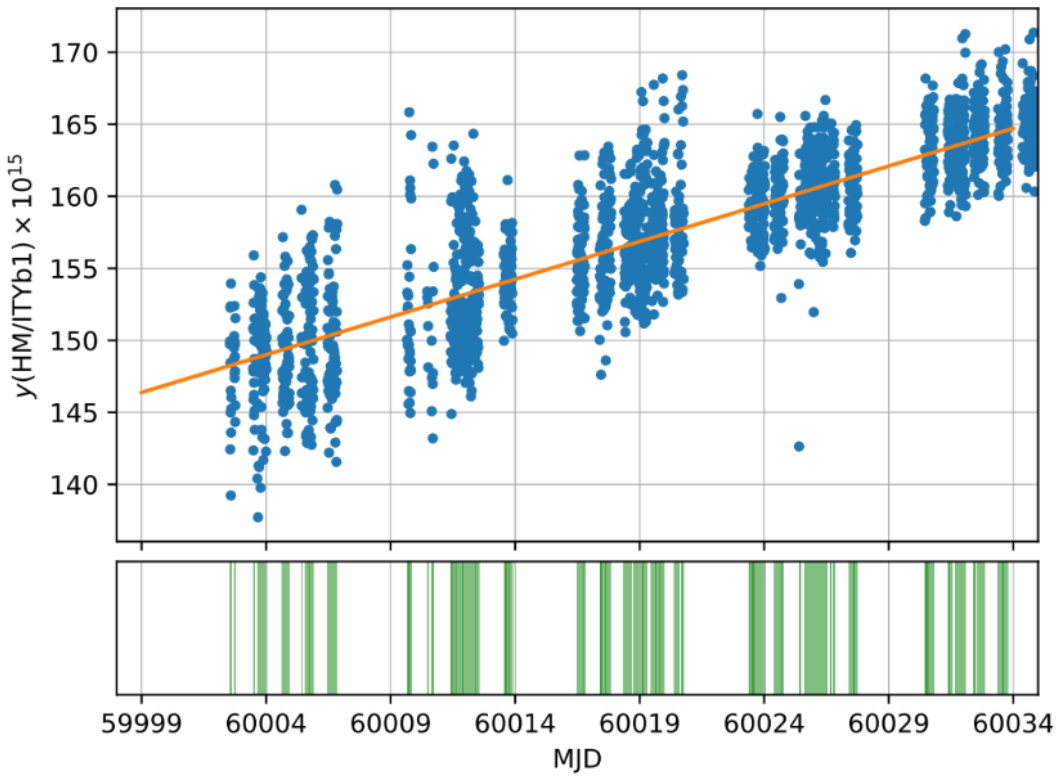

Fig. 5.1 Fractional frequency deviation y(IT-HM4/IT-Yb1) for the period MJD 59999-60034. The measured data are represented as blue dots, and the orange solid line indicates the maser drift calculated from the fit: $5.24(9) \times 10^{-16}$/d. The green shaded areas in the bottom plot represent the uptime of IT-Yb1 over this period, which for this month is 27.6%.

evaluated as its short-term stability extrapolated to the effective measurement time), u_B (the systematic uncertainty of the PSFS, calculated as its uncertainty budget), $u_{A/Lab}$ (the statistical uncertainty linked to dead time [174] of PSFS and frequency extrapolation), $u_{B/Lab}$ (the systematic uncertainty of the frequency comb, evaluated from comparison with a second optical frequency comb) and $u_{l/TAI}$ (the uncertainty calculated by BIPM of the link between the participating laboratory and the pivot of TAI, i.e., the PTB institute in Germany). The total uncertainty u does not include the uncertainty of the recommended value of the SRS u_{Srep}. Finally, the Circular T reports the monthly uptime of the PSFS and a flag indicating whether the PSFS has been approved and used for the steering of TAI ("Steer" column in Circular T).

3 - Duration of the TAI scale interval d.

Table 1: Estimate of d by individual PSFS measurements and corresponding uncertainty.
All values are expressed in 10**-15 and are valid only for the stated period of estimation.

Standard	Period of Estimation	d	uA	uB	uA/Lab	uB/Lab	ul/Tai	u	uSrep	Ref(uS)	Ref(uB)	uB(Ref)	Uptime %	LastRep	Nrep3y	Steer	Note
PTB-CS1	59634 59669	-18.88	8.00	8.00	0.00	0.00	0.06	11.31	PFS/NA		T148	8.00	100.0	T410	34	Y	(1)
PTB-CS2	59634 59669	-8.50	5.00	12.00	0.00	0.00	0.06	13.00	PFS/NA		T148	12.00	100.0	T410	35	Y	(1)
METAS-FOC2	59639 59669	-0.82	0.07	1.48	0.25	0.05	0.20	1.52	PFS/NA		T371	1.99	74.0	T410	10	Y	(2)
IT-CsF2	59634 59669	0.10	0.15	0.23	0.12	0.01	0.17	0.34	PFS/NA		T318	0.19	88.2	T410	23	Y	(3)
IT-Yb1	59634 59669	-0.51	0.00	0.02	0.08	0.02	0.17	0.19	0.5	[1]	T383	0.03	45.8	T410	10	Y	(4)
KRISS-Yb1	59634 59669	0.10	0.00	0.04	0.17	0.07	0.17	0.25	0.5	[1]	T405	0.03	21.8	T410	16	Y	(5)
NICT-Sr1	59634 59669	0.11	0.02	0.07	0.14	0.02	0.17	0.23	0.4	[1]	T371	0.06	5.5	T410	10	Y	(6)
NIM5	59634 59669	-0.03	0.32	0.90	0.10	0.01	0.17	0.98	PFS/NA		T340	1.40	99.5	T410	18	Y	(7)
NMIJ-Yb1	59634 59654	-0.03	0.01	0.12	0.04	0.10	0.28	0.33	0.5	[1]	T392	0.36	97.0	T410	18	Y	(8)
NMIJ-Yb1	59659 59669	-0.03	0.01	0.12	0.15	0.10	0.53	0.57	0.5	[1]	T392	0.36	92.4	T410	18	Y	(8)
NPL-CsF2	59639 59669	0.08	0.07	0.62	0.05	0.03	0.20	0.66	PFS/NA		T284	0.23	92.2	T410	25	Y	(9)
NRC-FCs2	59634 59669	-0.18	0.09	0.35	0.11	0.00	0.17	0.41	PFS/NA		T389	0.23	92.2	T410	28	Y	(10)
SYRTE-FO2	59634 59644	-0.07	0.30	0.24	0.08	0.00	0.53	0.66	PFS/NA		T301	0.23	85.6	T410	35	Y	(11)
SYRTE-FORb	59634 59669	0.26	0.20	0.25	0.09	0.00	0.17	0.37	0.6	[1]	T328	0.34	73.8	T410	35	Y	(11)
SYRTE-Sr2	59639 59669	-0.30	0.01	0.02	0.10	0.03	0.20	0.22	0.4	[1]	T350	0.05	56.9	T404	3	Y	(11)
PTB-CSF2	59634 59669	-0.35	0.12	0.17	0.01	0.00	0.06	0.22	PFS/NA		T370	0.17	95.2	T410	40	Y	(12)
SU-CsFO2	59634 59669	-0.34	0.34	0.22	0.13	0.00	0.17	0.46	PFS/NA		T315	0.50	86.3	T410	32	Y	(13)

Fig. 5.2 Primary and secondary frequency standard contribution to the evaluation of TAI in March 2022, taken from https://www.bipm.org/en/time-ftp/circular-t. The yellow shaded area highlights the contribution of IT-Yb1, while green arrows indicate the contribution of other optical clocks.

Green arrows in Figure 5.2 indicate the contributions of 5 optical clocks (IT-Yb1, KRISS-Yb1, NICT-Sr1, NMIJ-Yb1 and SYRTE-Sr2) to the steering of TAI for that period, a record number that evidences the improvements in the field of optical clocks.

5.2 IT-Yb1 contributions to the calibration of TAI

Since February 2022, IT-Yb1 has contributed regularly to the steering of TAI for a total of 14 months (until now).

# Standard IT-Yb1	Period of Estimation	d	uA	uB	ul/Lab	ul/Tai	u	uSrep	Ref(uB)	uB(Ref)	Steer	Year(uS)	YYMM	Uptime
IT-Yb1	58389 58419	0.17	0.01	0.03	0.32	0.26	0.41	0.5	[2]	0.03	Y	2017	1911	
IT-Yb1	58419 58434	0.14	0.01	0.03	0.57	0.49	0.75	0.5	[2]	0.03	Y	2017	1911	
IT-Yb1	58459 58469	-0.10	0.01	0.03	0.59	0.70	0.92	0.5	[2]	0.03	Y	2017	1911	
IT-Yb1	58489 58514	0.65	0.01	0.03	0.39	0.31	0.50	0.5	[2]	0.03	Y	2017	1911	
IT-Yb1	58514 58539	0.75	0.01	0.03	0.26	0.31	0.40	0.5	[2]	0.03	Y	2017	1911	
IT-Yb1	59384 59389	0.82	0.01	0.03	0.37	0.98	1.05	0.5	T383	0.03	Y	2017	2202	13.7
IT-Yb1	59394 59419	1.07	0.01	0.03	0.44	0.23	0.50	0.5	T383	0.03	Y	2017	2202	5.9
IT-Yb1	59459 59464	2.00	0.02	0.04	0.65	0.98	1.18	0.5	T383	0.03	Y	2017	2202	2.4
IT-Yb1	59564 59569	-0.19	0.00	0.02	0.08	0.98	0.99	0.5	T383	0.03	Y	2017	2202	75.7
IT-Yb1	59619 59634	-0.38	0.00	0.04	0.20	0.37	0.42	0.5	T383	0.03	Y	2017	2202	22.2
IT-Yb1	59634 59669	-0.51	0.00	0.02	0.08	0.17	0.19	0.5	T383	0.03	Y	2017	2203	45.8
IT-Yb1	59669 59679	-0.24	0.00	0.02	0.13	0.53	0.54	0.19	T383	0.03	Y	2021	2204	45.6
IT-Yb1	59709 59724	0.94	0.01	0.02	0.19	0.37	0.41	0.19	T383	0.03	Y	2021	2205	16.9
IT-Yb1	59729 59734	-0.30	0.01	0.03	0.45	0.98	1.08	0.19	T383	0.03	Y	2021	2206	10.0
IT-Yb1	59744 59759	-0.15	0.00	0.02	0.22	0.37	0.43	0.19	T383	0.03	Y	2021	2206	23.6
IT-Yb1	59759 59789	0.04	0.00	0.02	0.14	0.20	0.24	0.19	T383	0.03	Y	2021	2207	16.7
IT-Yb1	59789 59799	-0.11	0.01	0.02	0.27	0.53	0.59	0.19	T383	0.03	Y	2021	2208	7.8
IT-Yb1	59829 59844	0.79	0.01	0.03	0.36	0.37	0.51	0.19	T383	0.03	Y	2021	2209	5.0
IT-Yb1	59849 59879	0.16	0.00	0.03	0.21	0.20	0.29	0.19	T383	0.03	Y	2021	2210	12.1
IT-Yb1	59879 59909	0.09	0.00	0.03	0.22	0.27	0.35	0.19	T383	0.03	Y	2021	2211	9.3
IT-Yb1	59914 59939	-0.57	0.00	0.03	0.27	0.23	0.36	0.19	T383	0.03	Y	2021	2212	14.2
IT-Yb1	59954 59974	-0.25	0.00	0.02	0.19	0.28	0.34	0.19	T383	0.03	Y	2021	2301	18.8
IT-Yb1	59974 59999	-0.30	0.00	0.02	0.11	0.23	0.26	0.19	T383	0.03	Y	2021	2302	29.4
IT-Yb1	59999 60034	-0.28	0.00	0.02	0.12	0.23	0.26	0.19	T383	0.03	Y	2021	2303	27.6

Fig. 5.3 Summary of data collected by IT-Yb1 since October 2018, taken from BIPM website [175]. The period of estimation is indicated as MJD, while the value of d and the uncertainties are expressed in units of 10^{-15}. The red square highlights the data collected during the years of my Ph.D.

The uptime of IT-Yb1 in this period ranges from a few percent values up to 76% for some weeks. For example, the contribution of IT-Yb underlined in yellow in the Circular T shown in Figure 5.2 is characterized by a total uptime of 45.8%, a particularly high value for a non-automated optical clock. Moreover, the total uncertainty u of IT-Yb1 in this Circular T is 1.9×10^{-16}. This is the lowest uncertainty ever reported

for a single optical clock, equaled only by the contribution of NICT-Sr1 in Circular T number 408. Curiously, the total uncertainty u is limited by the satellite link, and such a lower value is therefore attainable only when the measurement interval (and consequently the averaging time) is sufficiently long (35 days for the Circular T reported in Figure 5.2).
The enhancement in the uptime of IT-Yb1 is a consequence of the implementation of upgraded parts of the setup, such as the automatic relock of the duplication cavity for the generation of the radiation at 399 nm described in Section 2.3.1 and the implementation of a new laser system at 1112 nm used for the generation of the green radiation at 556 nm. Indeed, the new diode laser (Section 2.3.2) is more stable and reliable than the previous one, which was a fiber laser. Moreover, the implementation of the vertical setup and the consequent reduction of the lattice power in the operational conditions have also contributed to the improvement in the robustness of the clock. Lastly, my dedication to the upkeep of the entire experimental setup, coupled with the supervision of the operational conditions constituted a factor in the improvement of the reliability of IT-Yb1.
To confirm the robustness achieved in recent years by IT-Yb1, in Figure 5.3, all the contributions of our optical clocks to TAI since October 2018 are shown. Data collected during my Ph.D. (from June 2021 to March 2023) are highlighted in the red square. Each submission is complemented by a brief report that includes all the relevant information about the clock and the data collected over the month. The reports are available on the BIPM website, in the section "Reports of evaluation of Primary and Secondary Frequency Standards" [176].
Finally, it is important to note, that the recommended value of Yb as SRS indicated by CCTF has changed in April 2022, and the associated uncertainty has decreased from 5×10^{-16} to 1.9×10^{-16}, as reported in Figure 5.3.

5.3 Optical clocks contribution to TAI

In the last few years, the number of optical clocks contributing to TAI has increased significantly. Figure 5.4 represents all the primary and secondary frequency standards submitting evaluations to the BIPM since 2003. The Figure is provided by BIPM [177].

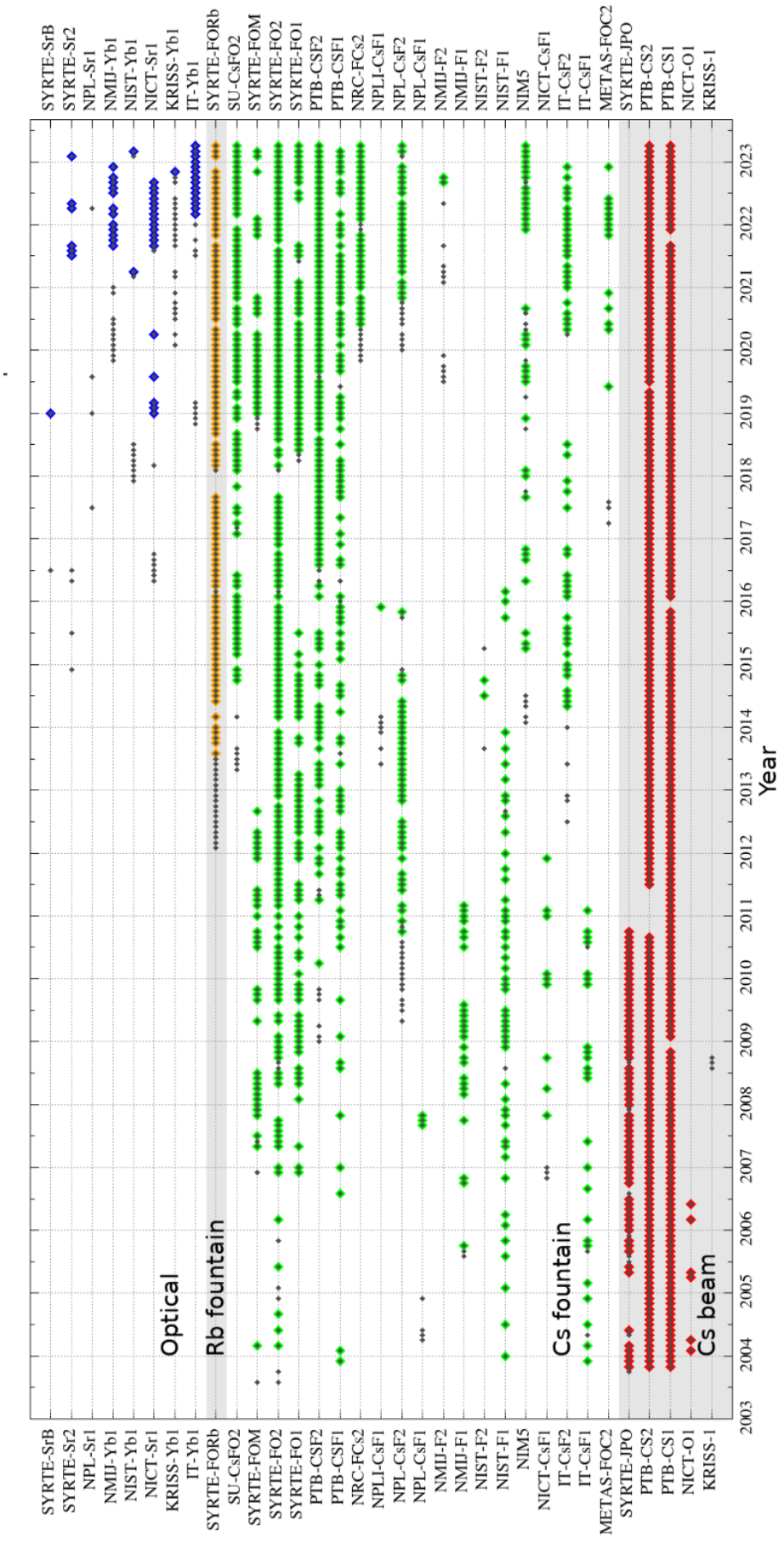

Fig. 5.4 Graphical representation of all submissions of primary and secondary frequency standards reported since Circular T 190 (September 2003). Enhanced color diamonds indicate evaluations carried out within the month of TAI computation. This Figure is taken from the BIPM website [177].

Colored diamonds indicate data provided "real-time" by contributing laboratories. In particular, red diamonds represent data obtained with atomic clocks based on Cs beam, while green diamonds represent the on-time data collected with Cs fountains standard. In orange are reported the data collected with the Rb fountain developed at SYRTE.

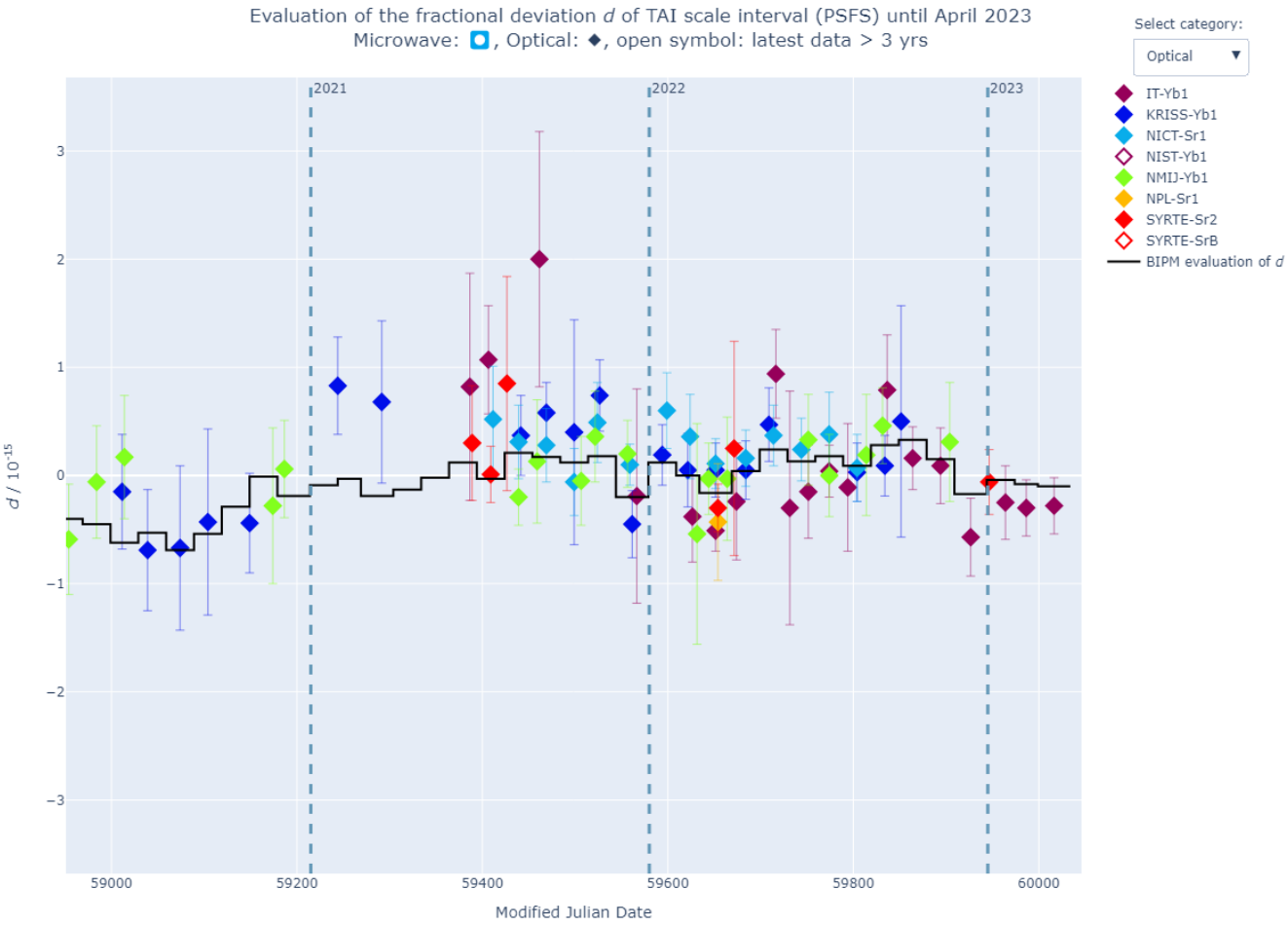

Fig. 5.5 Optical clock data appearing in Circular T compared with the duration on the TAI scale interval *d* represented as a black solid line. The data are shown as diamonds, and colors depend on the experiment that carried out the measurement (see legend). The data and the figure are taken from the BIPM Time Department DataBase [178].

Finally, in blue are indicated the contributions of optical clocks. It is significant to note that the first sporadic real-time data from optical clocks were collected in 2019 and that their contributions become considerably more regular in 2021. In particular,

IT-Yb1 holds the record for the longest period of regular contribution to TAI, with its 14 consecutive on-time submissions (from February 2022 to April 2023).
At the moment, 8 optical clocks worldwide have participated in TAI estimation: IT-Yb1, SYRTE-SrB, SYRTE-Sr2, NPL-Sr1, NMIJ-Yb1, NIST-Yb1, NICT-Sr1 and KRISS-Yb1. All these frequency standards are neutral clocks based on Yb atoms or Sr atoms.
Figure 5.5 provides an insight into the contributions of optical clocks: it reports, as a function of the MJD, the data collected and submitted by optical clocks to the BIPM during the last 3 years. The black solid line represents the BIPM evaluation of the fractional deviation d of the TAI scale interval (PSFS). Both the data and the plot can be found in the BIPM Time Department DataBase [178] updated to April 2023.
The weight of optical measurements in the TAI estimation has increased significantly in the last few years, as shown in Figure 5.6. The data used for this Figure are provided by BIPM [179] in "Fractional frequency of EAL from primary and secondary frequency standards".

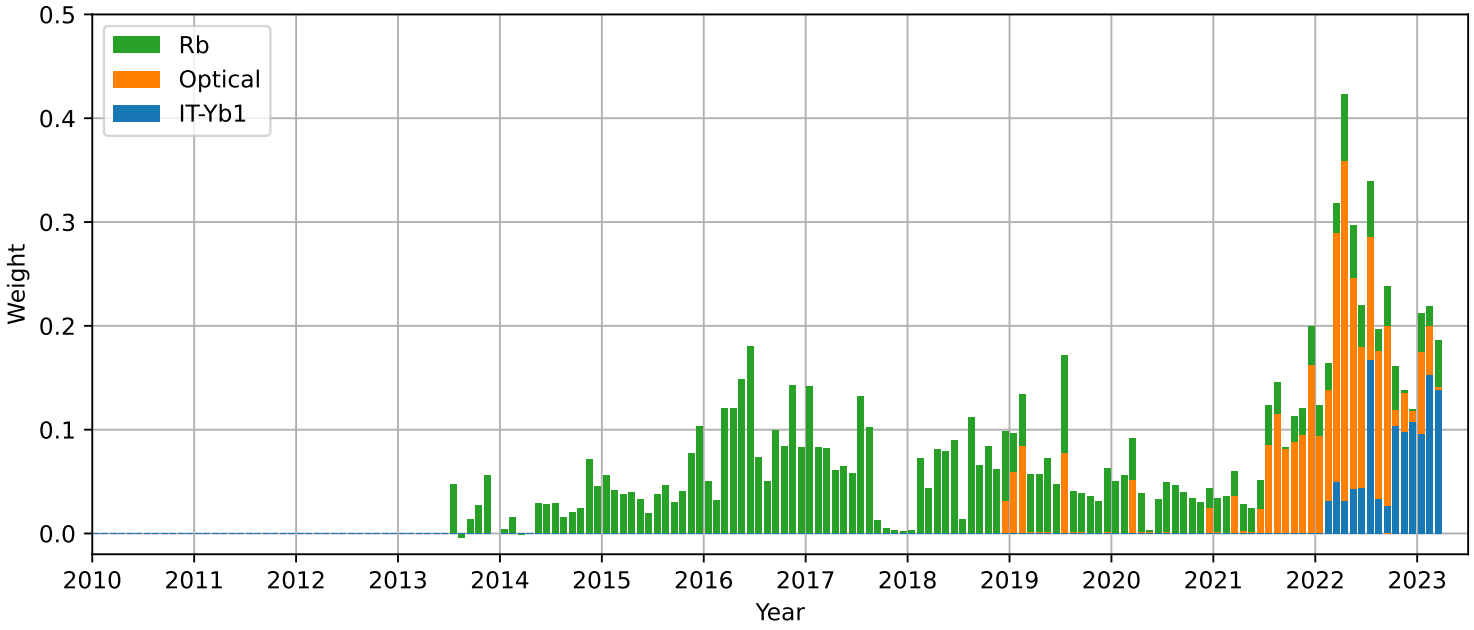

Fig. 5.6 Graphical representation of the weight of SRS in the computation of TAI over the last decade. Green bars represent the weight associated with the Rb fountain (SYRTE-FORb), while orange and blue bars represent the weight of the contributions of optical clocks. In particular, blue bars highlight the weight of the single IT-Yb1 clock. Data used to realize this Figure are provided by BIPM [179] in "Fractional frequency of EAL from primary and secondary frequency standards".

The contributions of optical clocks (orange and blue bars in Figure 5.6) have been quite regular since the middle of 2021. Moreover, the weight of optical clocks has increased since April 2022 as a consequence of the modification of the recommended values of frequency standards defined by CCTF. In the last year, the contribution of optical clocks has registered an average weight of about 20%, with a peak of about 40% in April 2022.
The weight of IT-Yb1 in the computation of TAI is reported in Figure 5.6 in blue bars. Since October 2022, the weight of IT-Yb1 is constantly at the level of 10%. During this period, the contribution of IT-Yb1 to the steering of TAI has the highest weight if compared to other optical clocks.
With their low uncertainty and relatively high uptime, optical frequency standards represent an important tool to improve the reliability of the uncertainty of TAI. In addition, in the future, the contribution of optical clocks in the evaluation of TAI is expected to continue to grow, making important steps toward the redefinition of the SI second. An essential element to ensure the regular contribution of optical clocks could be the implementation of automation and the development of commercial optical clocks.

Chapter 6

Cyclopix project: the observation of collective light scattering phenomena

In the last year of my Ph.D., I spent four months at the Laboratoire Charles Fabry in Palaiseau (France) with an Erasmus+Traineeship fellowship. During this experience, I joined the experimental team led by Antoine Browaeys, which works on the Cyclopix project. The goal of the internship was to study experimentally the collective effects in the light emitted by a laser-cooled ensemble of atoms held in an optical trap [180]. Indeed, in this experiment, an adjustable number of Rb atoms are trapped in microscopic dipole traps. The trapping conditions can be modified so that the atomic ensemble, whose number ranges from 1 to thousands, can be arranged forming either ordered arrays or disordered and very dense ensembles [181]. These effects originate for instance by light-induced dipole-dipole interaction or by the identical (cooperative) coupling of all the atoms to the electromagnetic field, as in Dicke superradiance [182, 183]. Among others, collective effects manifest as a modification in the photon emission rate with respect to the single atom case, which is given by the transition linewidth Γ_0. In particular, a photon emission rate larger than Γ_0 is called superradiance, while a smaller one is called subradiance [184–188]. Besides the fundamental interest in the study of many-body atomic systems and collective effects, several key components of the Cycplopix experiment are crucial also in the context of next-generation optical clocks. First, the Cyclopix optical setup allows the implementation of a dipole trap characterized by a diameter of a few micrometers to realize a tight optical tweezer [181] and, as described in Section 1.5, it is possible to exploit an optical tweezer and the fine control provided by this

trapping technique to realize optical clocks with a state-of-the-art accuracy [54, 55]. In addition, both the superradiance and subradiance phenomena are of great interest in the metrological context. Indeed, one can use the atomic collective behavior to extend the clock interrogation time and improve the clock stability [189–192]. Moreover, superradiance can be exploited to realize a new generation of atomic clocks based on the collective emission from the atoms that populate the excited state of the clock transition [193, 194].
The chapter is organized as follows: in Section 6.1, I describe the setup of the Cyclopix experiment. In Section 6.2, I present the results obtained during my internship. Finally, in Section 6.3, I briefly introduce a project that I started during my internship aiming at the observation of quantum interference effects between trapped atoms and an incoming field.

6.1 Setup of the Cyclopix experiment

Figure 6.1 shows a picture of the Cyclopix setup with the atomic chamber and the optical components.
In the Cyclopix experiment, a sample of Rb atoms can be confined in two optical dipole traps assembled in a crossed configuration.
As usual, the atoms are firstly cooled by implementing a Zeeman slower and a MOT stage to make the loading in the dipole trap efficient. In particular, a Toptica TA pro laser at 780 nm resonant with the D2 transition is exploited for this cooling process. In addition, the D1 transition ($\lambda = 795\,\text{nm}$) is utilized for the implementation of the grey-molasses technique that further increases the loading efficiency in the dipole trap. This cooling mechanism has been used to achieve a large loading probability in arrays of optical tweezers [195].
Each optical trap is realized by a red-detuned off-resonant laser beam, focused by an aspherical lens (AL) with NA = 0.44, placed inside the vacuum chamber. By placing the aspheric lenses under the vacuum chamber, eventual optical aberrations produced by the atomic chamber windows are avoided, and, in the meanwhile, the lenses are as close as possible to the trapping region. The two pairs of lenses are arranged in the Maltese Cross configuration [196]. This provides two imaging axes operating at the diffraction limit and allows atomic manipulation, via optical potential, at a micrometer scale. A sketch of the dipole crossed trap setup is shown in Figure 6.2. One

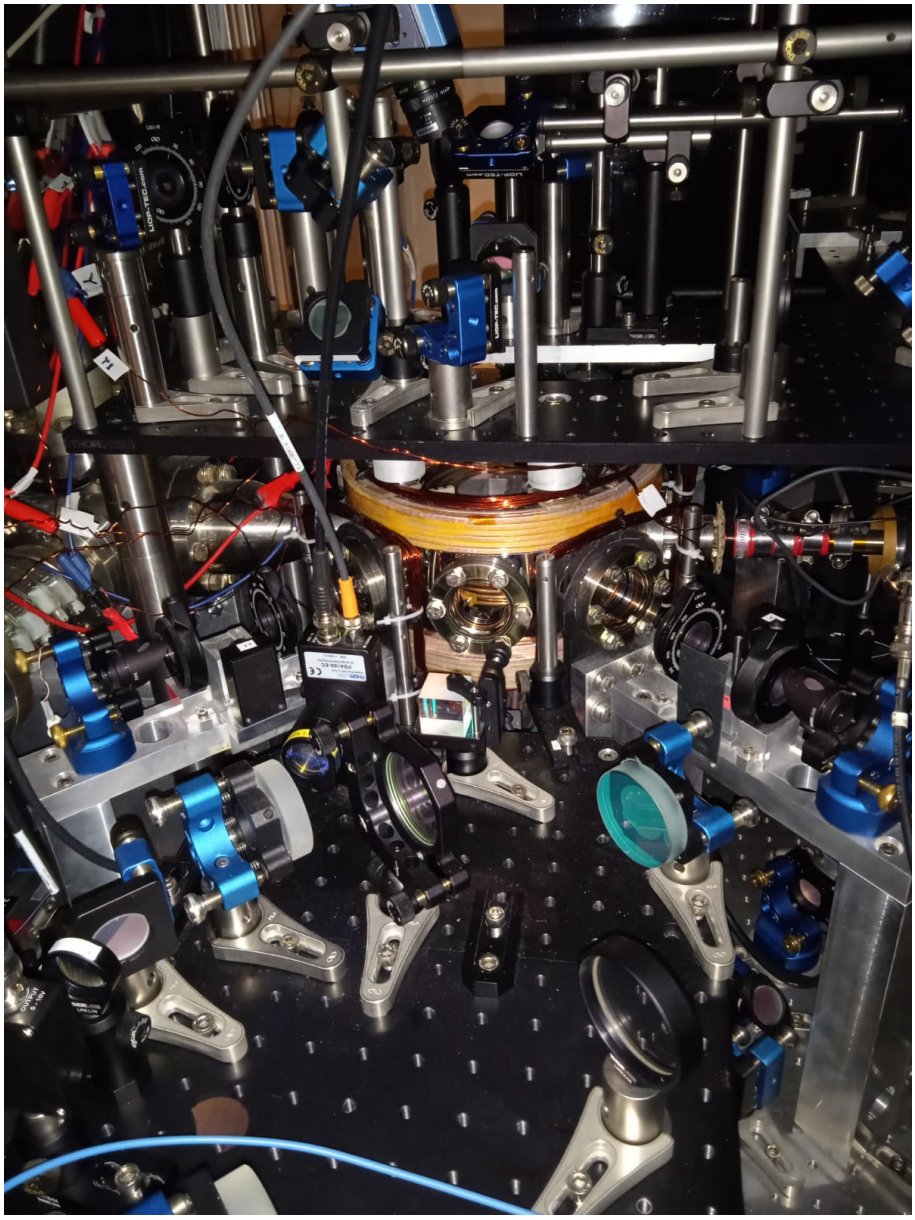

Fig. 6.1 Picture of the optical setup of the Cyclopix experiment.

of the dipole traps, which is called "horizontal trap", is generated by a laser beam at 940 nm with a power of about 280 mW. The waist of this dipole trap is dynamically controlled via a telescope characterized by a controllable magnification [181], which can range between 1 and 5. The telescope, manufactured by OptoTune, is composed of two lenses whose focal length is modified by an applied current. In this way, it is possible to modify the size of the collimated beam before being focused by the in-vacuum aspheric lens and, therefore, it is possible to control the waist of the

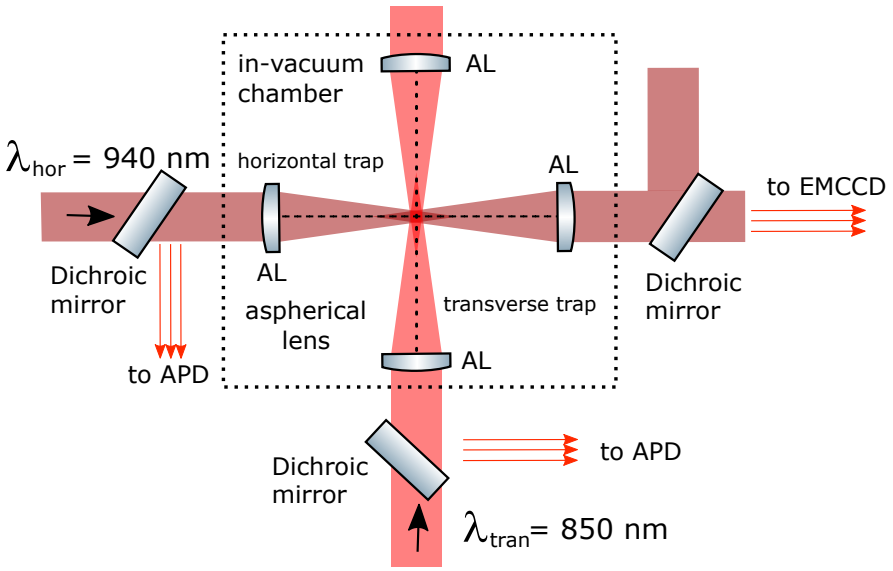

Fig. 6.2 Simple sketch of the Cyclopix optical setup. The dotted box represents the vacuum chamber, with the four aspherical lenses (AL) utilized to create the crossed dipole trap. Four dichroic mirrors are used to distinguish the atomic fluorescence signal from the trapping beams and to collect it with two EMCCD cameras and two APDs.

dipole trap.

The second dipole trap is called "transverse trap" and is perpendicular to the horizontal one. It is generated by a laser beam at 850 nm. Typically, both the horizontal and the transverse traps have a waist of about 2 µm. In the next section, I will describe the technique that allows the measurement of the trap waist.

The atomic signal is collected and observed through an imaging system composed of two avalanche photodiodes (APD) in single photon counting mode and an electron-multiplying CCD camera (EMCCD). Significantly, the EMCCD high gain ensures the detection of a single atom. Several dichroic mirrors are added in the setup to separate the atomic fluorescence signal from the trapping beams.

By implementing the setup described above, it is possible to realize various physical scenarios and conduct different experiments. In particular, besides loading a dense cloud of Rb atoms, exploiting light-assisted collisions [197], it is also possible to trap a single atom in the crossed dipole trap, as well as realize a 1D array of atoms in a single retroreflected dipole trap.

Both the dense cloud and the 1D array of atoms have proven to be physical systems useful to realize light-matter interfaces based on collective effects [182, 198, 199, 183, 200].

6.2 Characterization of trapping conditions

During my internship at the Laboratoire Charles Fabry, I learned how to characterize in-situ the trapping potential realized by a single or by a combination of optical tweezers.
In the first weeks, I worked to trap atoms in the crossed dipole trap. Figure 6.3 shows a fluorescence, in-situ image of the Rb cloud trapped in the crossed dipole trap.

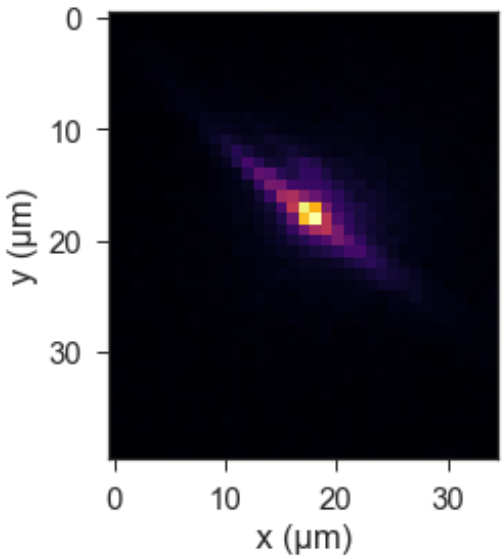

Fig. 6.3 In-situ image of a sample of Rb atoms trapped in the crossed dipole trap acquired with the CCD. The typical cigar shape of the dipole trap perpendicular to the CCD is visible. From a first qualitative estimate, the waist of the trap is about 2 µm.

Waist measurement

To calculate the waist w_0 of the horizontal and transverse dipole traps, we measure the radial oscillation frequency of the atoms in the traps (ω_r) by using the parametric heating technique. This technique consists of applying a sinusoidal modulation to the trapping beam intensity. In this way, when the modulation frequency is equal to $2\omega_r$ the atoms are heated, and losses are induced. The upper panel of Figure 6.4 illustrates the results obtained by applying this technique to the horizontal dipole trap. By repeating this measure for different trap beam power P, remembering that $\omega_r = \sqrt{\frac{4U_0}{mw_0^2}}$ where m is the Rb mass and the trap depth $U_0 \propto P$ and knowing the Rb polarizability, it is possible to calculate the waist of the trap. The results are

shown in the lower panel of Figure 6.4. From this measurement, the waist of the horizontal dipole trap results to be $w_{0,hor} = 1.65(10)\,\mu$m. With the same procedure,

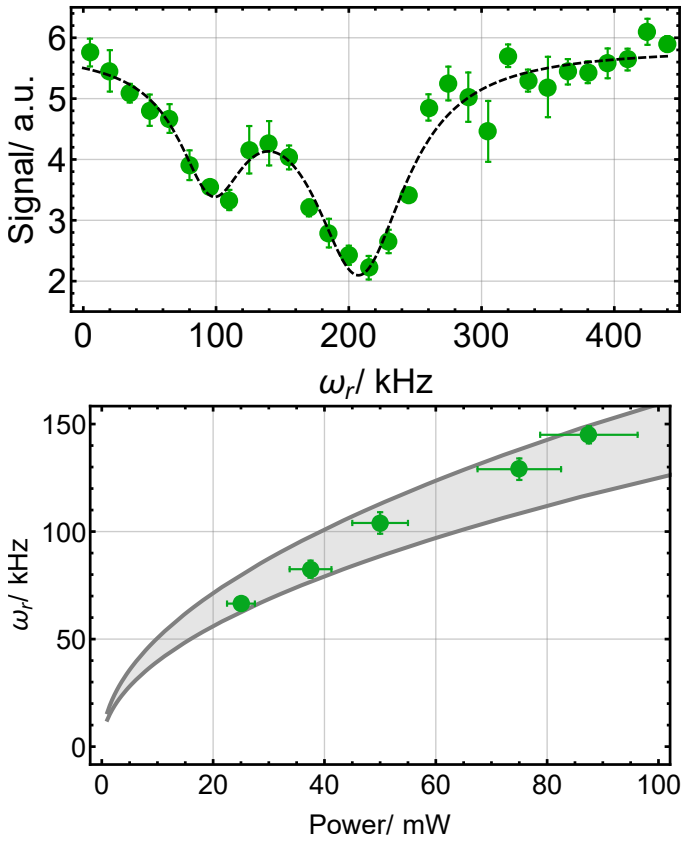

Fig. 6.4 Horizontal dipole trap waist measurement via parametric heating. Top panel: parametric heating measurement of the trap radial oscillation frequency ω_r. The atomic signal, evaluated in arbitrary units, decreases when the trap beam modulation frequency is $2\omega_r$. The atomic loss in correspondence of ω_r is due to a non-ideal modulation of the trap beam power or to a potential not perfectly harmonic [201]. The radial oscillation frequency is calculated from the atomic signal with a Gaussian fit. Bottom panel: ω_r as a function of the trap beam power. From the equation reported in the main text, it is possible to fit the data and calculate the waist w_0 of the trap. The result of the fit $w_{0,hor} = 1.65(10)\,\mu$m is shown as grey lines and the shaded area.

we estimate the waist of the transverse dipole trap to be $w_{0,tran} = 2.05(10)\,\mu$m.

Rabi oscillation measurement

In order to get rid of the internal structure of Rb and create a cloud of two-level emitters, we carried out the experiment under the presence of a strong magnetic field.

In this way, after performing hyperfine and Zeeman optical pumping to the state $|F, m_F\rangle = |2,2\rangle$, when the atomic cloud is excited by a high-intensity resonant laser pulse the system undergoes Rabi oscillation between the states $|2,2\rangle$ and $|3,3\rangle$. This coherent dynamic can be measured via a time-resolved fluorescence using an APD, being the photon emission rate proportional to the population of the excited state. The result of this measurement is shown in Figure 6.5, where the atomic population in the excited state expressed as the density matrix element ρ_{ee} is plotted as a function of time. Remarkably, for resonant light, the Rabi frequency Ω_R is related to the pulse

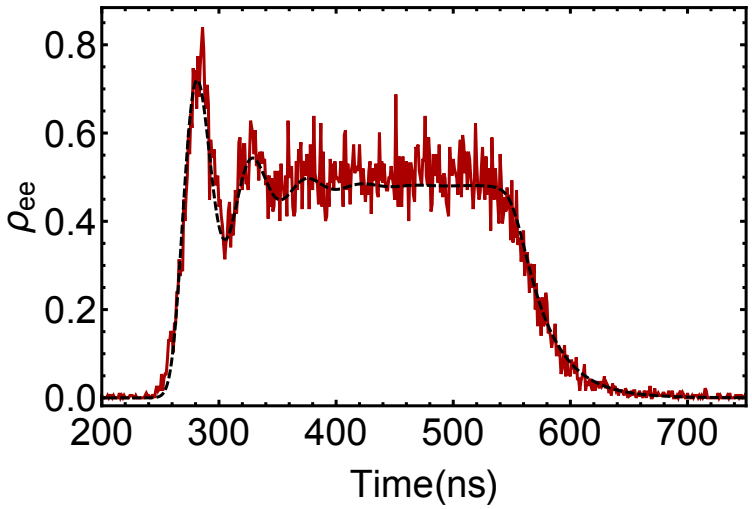

Fig. 6.5 Fluorescence signal collected on an APD. The excited state population ρ_{ee} presents the Rabi oscillations typical of a two-level system. The Rabi frequency is evaluated by fitting the signal with the well-known Optical Bloch Equations [202]. The result of the fit is shown as a black dashed line.

intensity as $\Omega_R = \Gamma\sqrt{s/2}$, where $s = I/I_{sat}$ is the saturation parameter and Γ is the decay rate of the excited state. As a consequence, the Rabi oscillation measurement allows us to estimate the light intensity on the atoms.

Optimization of gray-molasses parameters

The grey molasses (GM) is a cooling technique that allows us to reach sub-Doppler temperatures. GM is based on the interaction of a blue-detuned laser beam with a Λ-type atomic system [203, 204]. The eigenstates of the total system composed of the Λ-type atom and the electromagnetic field are the so-called dressed states. At the end of the cooling mechanism, the atoms occupy the dark state, which is a superposition of the two atomic ground states. By adding a GM stage before the

loading in the dipole trap, the achievable atomic density increases if compared to the case of direct loading from the MOT [205]. In addition, it has been proven that the implementation of the GM increases the loading efficiency of a single atom in the optical tweezer up to a loading probability of about 90% [195], much higher than the 50% achievable with more standard techniques such as collisional blockade [197].

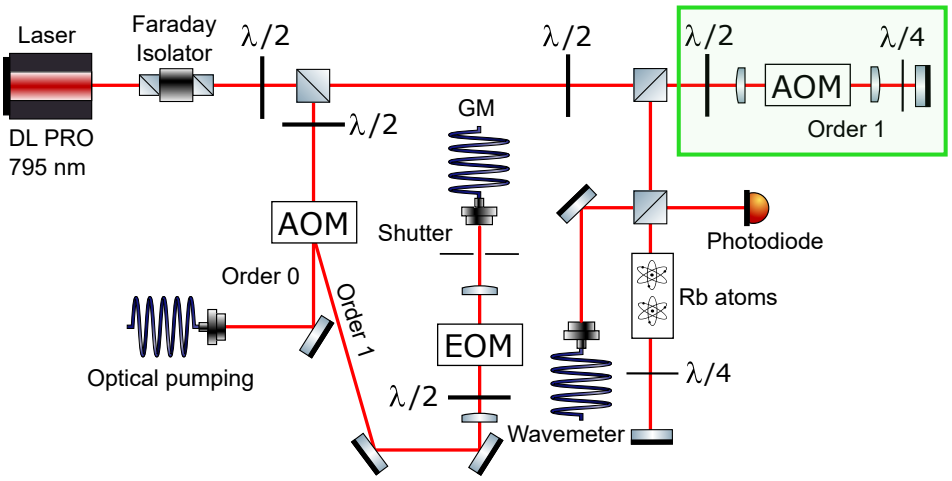

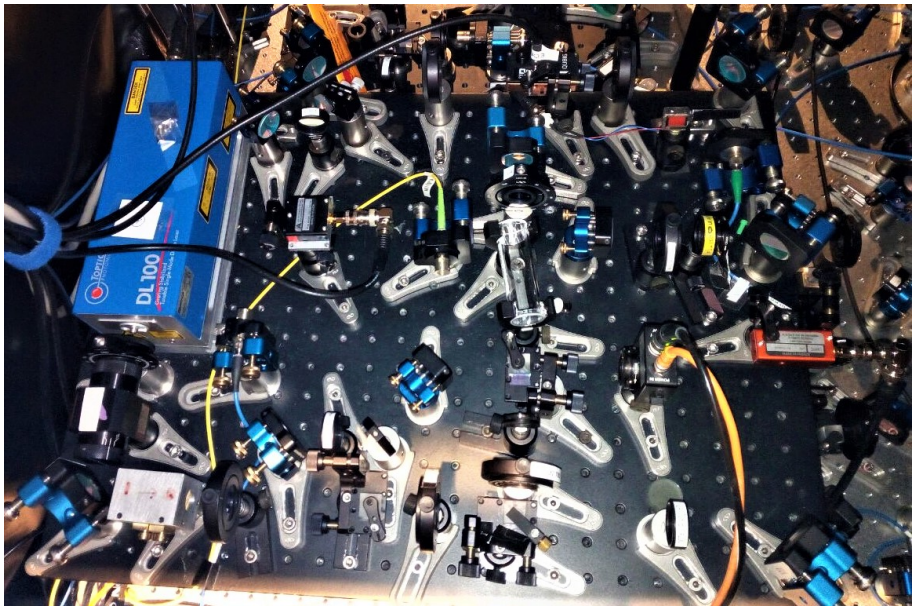

Fig. 6.6 Scheme and picture of the new setup for the realization of the GM. The additional AOM that is used to scan the frequency of the laser is represented in the green box.

The efficacy of the GM process strongly depends on various experimental parameters, such as the laser frequency, the duration and the power of the cooling pulse, and the absence of any residual magnetic field. During the optimization of these parameters,

we realized that we needed more flexibility in terms of frequency to perform a wider scan and find the optimal value. For this reason, I implemented a new optical setup for the GM, which is shown in Figure 6.6.
Compared to the previous setup, the new one is provided with an additional AOM (represented in Figure 6.6 in the green box) that is used to shift the frequency of the cooling laser. In this way, it is possible to scan the laser frequency in a range of about 20 MHz.
After a careful optimization of the GM parameters, we succeeded in trapping a sample of about 3×10^3 Rb atoms in the crossed dipole trap. Figure 6.7 shows the atomic signal collected with the CCD camera and the corresponding signal fitted with a Gaussian curve. The implementation and optimization of the GM technique

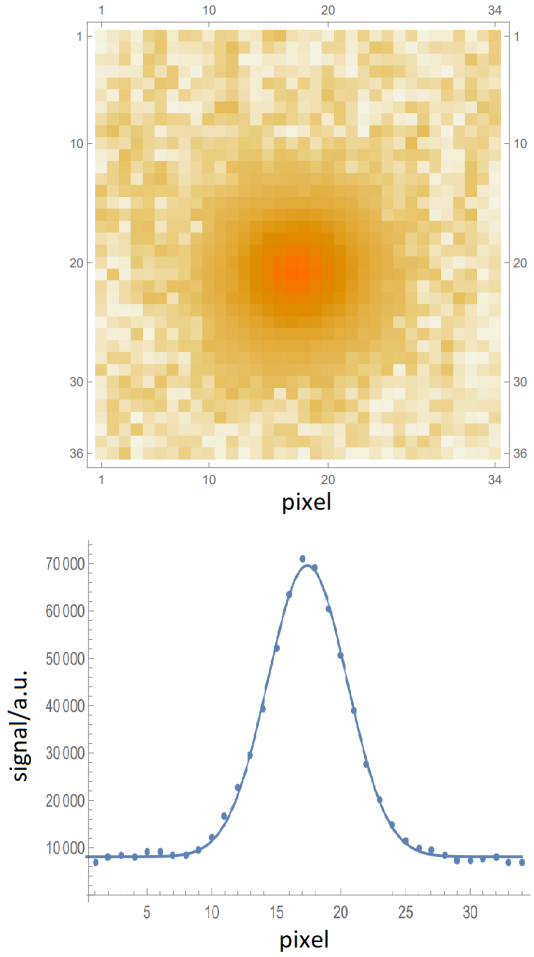

Fig. 6.7 Top panel: fluorescence imaging of an atomic cloud of about 3×10^3 atoms trapped in the crossed dipole trap. Bottom panel: atomic signal integrated along the horizontal direction and fitted with a Gaussian curve.

allowed us to increase the number of trapped atoms by a factor of 10.
The temperature of the atomic cloud is estimated to be about 100 μK from a time-of-flight measurement.

6.3 Searching for quantum interference effects

In a recent theoretical proposal [206], Goncalves *et al.* show that quantum correlations are supposed to arise when a single two-level atom is resonantly illuminated by two coherent and continuous laser beams, i.e., a probe and a pump beams, that propagate orthogonally to each other. In this case, the transmitted light collected in the probe direction is composed of three contributions: the probe beam and the field scattered by the atoms due to the interaction with the probe and the pump beams. In the weak driving regime, i.e., when $|\Omega| = \left|\Omega_{\text{pump}} + \Omega_{\text{probe}}\right| \ll \Gamma_0$, where Γ_0 is the atomic free-space spontaneous emission rate and Ω is the Rabi frequency of the total driving field, the transmission coefficient in the probe mode is $T = |1 - 2\Lambda|^2$, where $\Lambda = \eta\Omega/\Omega_{\text{probe}}$. In this expression, Λ plays the role of an effective coupling parameter and depends on the free-space atom-photon coupling η, the ratio $\left|\Omega_{\text{pump}}\right|/\left|\Omega_{\text{probe}}\right|$ and the relative phase ϕ between the two driving fields. Figure 6.8 illustrates how the pump beam power affects the transmission of the light in the probe mode. In particular, Figure 6.8 shows the transmission coefficient T in the probe mode as a function of the laser detuning Δ in units of Γ_0 for different effective coupling efficiency $\Lambda = \{0.05, 0.25, 0.5, 1.1\}$ represented in different colors from light to dark blue. From the Figure, we note that by increasing the pump beam power and thus the value of Λ, it is possible to reduce the transmission down to 0 when $\Lambda = 0.5$ and reach $T > 1$ for $\Lambda > 0$. Essentially, the pump beam is used to finely control and modify the coupling efficiency between a beam and a single atom, which is generally low due to the diffraction limit.
In addition, in Ref. [206], the authors show that also the second-order correlation function $g^{(2)}(\tau)$ depends on Λ. Notably, when $\Lambda = 0.4$ it is possible to predict both antibunched correlations ($g^{(2)}(\tau) < 0.5$) and large photon bunching effect ($g^{(2)}(\tau) > 10$).

We try to implement this theoretical proposal, exploiting the two axes that characterize Cyclopix. However, differently from the original idea, we try to use an

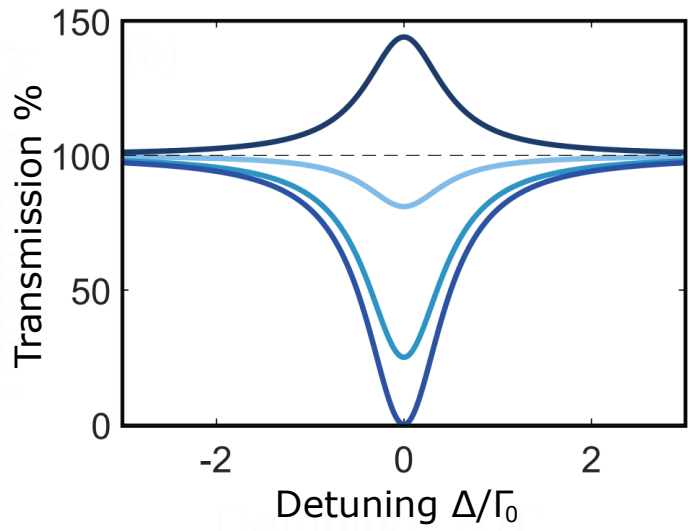

Fig. 6.8 Transmission coefficient as a function of the laser detuning Δ, adapted from [206]. Different colors represent, from light to dark blue, different values of the effective coupling parameter $\Lambda = \{0.05, 0.25, 0.5, 1.1\}$.

ensemble of atoms rather than a single one. This choice is motivated by the low collection efficiency we have, which makes it hard to operate with a single emitter. Due to the severe constraints imposed by the theoretical analysis over the position of the emitter, we confine the atoms in the cross-dipole trap which ensures a strong trapping potential in 3D. In our case, the probe beam propagates along the horizontal dipole trap direction (see Figure 6.2), while the pump beam propagates along the vertical direction, perpendicular to the probe beam. The transmission (or the fluorescence) signal in the probe mode was then measured as a function of the laser detuning Δ through the EMCCD.

However, we did not observe any correlation effect, as shown in Figure 6.9. Indeed, the transmission in the probe mode, represented in yellow dots, is simply composed of the linear sum of the pump beam fluorescence (blue dots) and the probe beam transmission (red dots). The pump beam intensity was set to $s/2$, where s is the saturation parameter, and the laser detuning was scanned in a range of about 40 MHz, centered on the resonance value.

We performed a numerical simulation using a mesoscopic number of emitters, showing that light-induced dipole-dipole interaction destroys the enhanced response described by Goncalves *et al*. The experimental findings are in qualitative agreement with the numerical results.

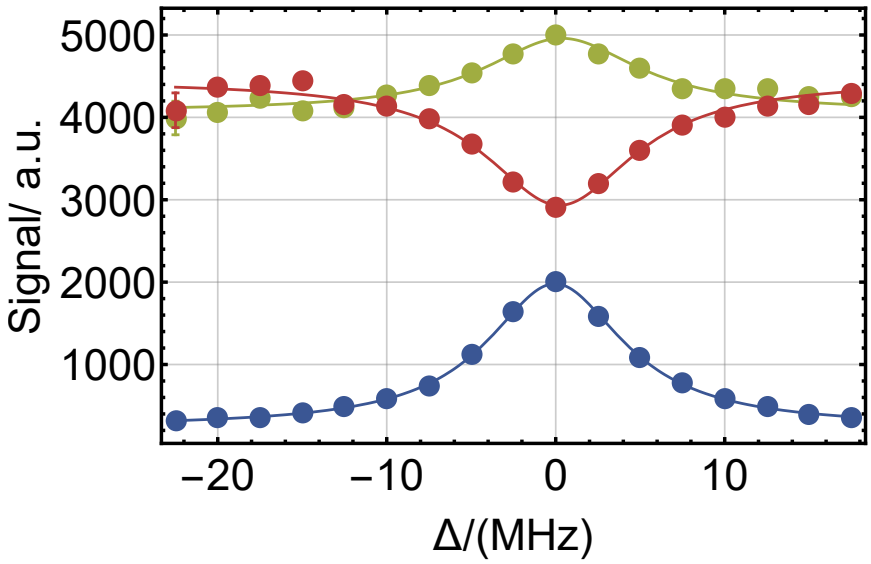

Fig. 6.9 Measurement of the transmission signal in arbitrary units in the probe mode as a function of the driving laser detuning. The signal collected when the atoms are driven by both the probe and the pump beam is represented in yellow dots. This is the linear sum of the fluorescence due to the pump beam, represented in blue dots, and the transmission of the probe beam, shown in red dots. The pump beam intensity was set to $s/2$, where s is the saturation parameter.

Even though we did not observe any non-linear effect in the transmission signal, we are confident that the experimental setup is suitable to observe the quantum correlations and that this work laid the ground for future data acquisitions. In particular, before proceeding with further measurements, it would be necessary to implement a phase control to monitor the phase difference between the pump and the probe beams. Moreover, it would be essential to carry out this experiment with a single atom in order to avoid interaction between different atomic dipoles that may affect the transmission signal.

Chapter 7

Conclusions and future projects

The research I carried out during my Ph.D. has been focused on the improvement of the optical clock based on Yb atoms developed at the INRiM institute, IT-Yb1. In the first part of my Ph.D., I implemented a new optical setup for generating a vertical lattice that enables better control of the atomic sample and, consequently, an improvement in the clock accuracy. Therefore, once accomplished the new setup, I determined the accuracy budget of IT-Yb1. This analysis has led to a total fractional uncertainty of about 2×10^{-17}. The main limiting factors to the accuracy of our clock are related to the experimental setup itself (such as the atomic chamber). To further improve the accuracy of IT-Yb1, substantial changes in the whole apparatus are inevitable.
In the second part of my Ph.D., I focused on running the clock while maintaining the usual operating conditions and monitoring the systematic shifts. I managed to collect data almost continuously for a year and a half, with an uptime of about 40% in some months. Over the past year and a half, IT-Yb1 has shown good stability and robustness, allowing almost continuous operation, with only minor intervention to maintain the working conditions unchanged. Yb frequency measurements performed at this stage have been collected and processed for different purposes:

- to evaluate the absolute frequency of IT-Yb1 against the local primary standard IT-CsF2. The result of this comparison is in agreement with the recommended value of Yb indicated by the CCTF and has a fractional uncertainty of 2.7×10^{-16}, the lowest ever obtained with a Yb clock measured against a single Cs fountain. In addition, during this campaign, we tested a new method to

generate the microwave signal for the interrogation of Cs atoms by synthesizing it from the optical signal of the Yb local oscillator using an optical frequency comb;

- to compare the frequency of IT-Yb1 with the Cs-Rb fountain developed at SYRTE. This measure is the first clock comparison ever performed via the new optical fiber link between INRiM and SYRTE. This campaign has led to the evaluation of both the absolute frequency of IT-Yb1 against the French Cs fountain and the frequency ratio between Yb and Rb. Both these results are comparable with the frequency values of Yb and Rb recommended by the CCTF;

- to contribute to the International Atomic Time (TAI) steering. In February 2022, we submitted to the BIPM the first data of IT-Yb1 for real-time calibrations of TAI. Since February 2022, IT-Yb1 data have been regularly included in the steering of TAI. With its 14 consecutive months of contribution, our clock boasts the longest on-time contributing period without interruption for an optical clock. Moreover, IT-Yb1 data submitted to the BIPM in March 2022 have the lowest total uncertainty ever reported for a single optical clock contributing to TAI (equaled only by NICT-Sr1 data submitted for Circular T 408). Finally, since October 2022, IT-Yb1 data has the highest weight in the steering of TAI with respect to other SRS, with a constant weight of about 10%.

My research activity helped to improve the performance of IT-Yb1 and to perform several clock comparison measurements, making important progress toward the redefinition of the SI second.

Lastly, in the last year of my Ph.D., I spent 4 months at the Laboratoire Charles Fabry, Palaiseau (France), with a student mobility European Erasmus+Traineeship fellowship. There, I gained experience in the field of atomic manipulation and optical tweezer, a promising tool that can be implemented in next-generation optical clocks. The goal of the internship was to study experimentally the collective emission of light by an ensemble of laser-cooled atoms held in an optical trap.

Ongoing projects

In the last few years, IT-Yb1 has participated in several projects and international campaigns whose results are still under analysis and are not yet published. Therefore these results are not reported in this thesis. In the following, I briefly describe the most interesting ongoing projects:

- *ROCIT (Robust Optical Clocks for International Timescales) campaign*: it is a three-year long EMPIR (European Metrology Programme for Innovation and Research) project (code 18SIB05) that aims to improve the robustness of optical clocks and their reliability. In March 2022, a comparison campaign was carried out using the data of IT-Yb1 and the optical clocks developed at PTB, NPL, SYRTE, VTT, UMK and NMIJ, for a total of 10 optical clocks involved. The clock comparison was performed by using GPS and satellite techniques. INRiM, SYRTE and PTB were also connected via optical fiber. The ROCIT comparison was the first campaign involving up to 5 optical clocks connected via a fiber link. The project was terminated in October 2022, and the results of the measurement campaign are still under analysis.

- *Yb clocks comparison with KRISS via VLBI*: in December 2021, we measured the frequency of IT-Yb1 against the Yb optical clock developed at the KRISS institute in South Korea. This frequency comparison was performed via the VLBI (very long baseline interferometry) techniques. For this measurement, we compared the frequency of IT-Yb1 with that of the local H-maser, and we sent the H-maser signal to the Medicina INAF Radio Observatory using the fiber link. Similarly, the Yb clock at KRISS was measured against a local H-maser and the signal was sent to the radio station baseline. The H-maser signals are thus shared via the two antennas, and it is possible to calculate the frequency ratio between the two Yb clocks. Given the complexity of the experiment and the data analysis, the results of this measure are still under evaluation.

- *2023 International campaign*: in March and April 2023, we participated in a comparison campaign, together with SYRTE, PTB, NPL and the transportable Sr clock developed at the RIKEN institute in Japan. The clock comparisons between up to 8 optical clocks were performed through the optical fiber link. In the first stage of this comparison, the transportable RIKEN Sr clock was

brought to NPL, as well as the Sr transportable clock developed at PTB. Then, the two transportable clocks were moved to PTB, where a second measurement phase was performed. The common uptime of the involved optical clocks is promising, and the data analysis will be carried out in the next months.

- *Optical timescale based on IT-Yb1*: IT-Yb1 data are currently used to produce a robust algorithm for generating an optical time scale [207–209]. The algorithm is applied to experimental data of the Yb frequency measured against a local H-maser. Two types of algorithms are currently under analysis: an online and an offline test. Preliminary results show a sub-nanosecond accuracy for both the online and the offline test, and future developments, such as the inclusion of IT-Yb1 data in the generation of the Italian time scale UTC(IT), are under evaluation.

Future projects

In the coming years, IT-Yb1 will continue to collect data and contribute to the steering of TAI. In addition, we will be involved in other clock comparison campaigns. In particular, we will participate in the three-year-long EPM (European Partnership on Metrology) project (code 22IEM01) TOCK (Transportable optical clocks for key comparisons) together with the other major NMIs in Europe. The main goal of TOCK is the development of transportable clocks and the assessment of their performance. To do that, INRiM will host the transportable Sr clock developed at PTB, and we will perform a local comparison measurement with IT-Yb1, and a remote comparison with clocks located at NPL and SYRTE via fiber link.

Regarding the performance of our apparatus, the accuracy budget of our clock is currently close to its limit. Indeed, the main contributions to the total uncertainty derive from how the experimental apparatus was conceived. To achieve the goal of a fractional uncertainty of 10^{-18}, we will develop a new Yb optical clock, IT-Yb2. For IT-Yb2, we are planning a new experimental apparatus, and the details of the project of IT-Yb2 are currently under evaluation. We are planning a different vacuum system with two atomic chambers to prevent the oven from being in the line of sight with the interrogation region. Also, the design of the new experiment includes an enhancement cavity to improve the lattice shift evaluation. To avoid the DC Stark

shift, the windows of the atomic chamber will be provided with ITO coating. Moreover, the new clock will be equipped with in-vacuum thermal sensors to monitor the temperature in the trapping region and to improve the evaluation of the blackbody radiation shift uncertainty.
To improve the instability of IT-Yb1, in the coming years, we will install a new ultrastable cavity for the clock laser stabilization. The new ultrastable cavity will be 30 cm long, and the instability of IT-Yb1 and IT-Yb2 are expected to reach the 10^{-16} level at 1 s of averaging time.
All these upgrades will lead to meeting the criteria indicated by the CCTF in order to redefine the SI second with optical standards.

List of publications

- *"Absolute frequency measurement of a Yb optical clock at the limit of the Cs fountain"*, I. Goti, S. Condio, C. Clivati, M. Risaro, M. Gozzelino, G. A. Costanzo, F. Levi, D. Calonico, and M. Pizzocaro, Metrologia 60 no. 3, (May, 2023) 035002.

- *"Coherent optical-fiber link across Italy and France"*, C. Clivati, M. Pizzocaro, E. Bertacco, S. Condio, G. Costanzo, S. Donadello, I. Goti, M. Gozzelino, F. Levi, A. Mura, M. Risaro, D. Calonico, M. Tønnes, B. Pointard, M. Mazouth-Laurol, R. Le Targat, M. Abgrall, M. Lours, H. Le Goff, L. Lorini, P.-E. Pottie, E. Cantin, O. Lopez, C. Chardonnet, and A. Amy-Klein, Phys. Rev. Appl. 18 (Nov, 2022) 054009.

- *Generation of a robust optical time scale at INRiM*, V. Formichella, G. Signorile, T. T. Thai, L. Galleani, M. Pizzocaro, I. Goti, S. Condio, C. Clivati, M. Risaro, F. Levi, D. Calonico and I. Sesia, in preparation.

References

[1] J. Guena, M. Abgrall, D. Rovera, P. Laurent, B. Chupin, M. Lours, G. Santarelli, P. Rosenbusch, M. E. Tobar, R. Li, K. Gibble, A. Clairon, and S. Bize, "Progress in atomic fountains at LNE-SYRTE", *IEEE Transactions on Ultrasonics, Ferroelectrics and Frequency Control* **59** no. 3, (Mar, 2012) 391–409.

[2] A. Takamizawa, S. Yanagimachi, and K. Hagimoto, "First uncertainty evaluation of the cesium fountain primary frequency standard NMIJ-F2", *Metrologia* **59** no. 3, (Apr, 2022) 035004.

[3] S. Weyers, V. Gerginov, M. Kazda, J. Rahm, B. Lipphardt, G. Dobrev, and K. Gibble, "Advances in the accuracy, stability, and reliability of the PTB primary fountain clocks", *Metrologia* **55** no. 6, (Oct, 2018) 789.

[4] F. Levi, D. Calonico, C. E. Calosso, A. Godone, S. Micalizio, and G. A. Costanzo, "Accuracy evaluation of ITCsF2: a nitrogen cooled caesium fountain", *Metrologia* **51** no. 3, (May, 2014) 270.

[5] S. Beattie, B. Jian, J. Alcock, M. Gertsvolf, R. Hendricks, K. Szymaniec, and K. Gibble, "First accuracy evaluation of the NRC-FCs2 primary frequency standard", *Metrologia* **57** no. 3, (Apr, 2020) 035010.

[6] BIPM, "Recommended values of standard frequencies." https://www.bipm.org/en/publications/mises-en-pratique/standard-frequencies.

[7] K. Beloy, M. Bodine, T. Bothwell, S. Brewer, S. Bromley, J.-S. Chen, J.-D. Deschênes, S. Diddams, R. Fasano, T. Fortier, Y. Hassan, D. Hume, D. Kedar, C. Kennedy, I. Khader, A. Koepke, D. Leibrandt, H. Leopardi, A. Ludlow, and X. Zhang, "Frequency ratio measurements at 18-digit accuracy using an optical clock network", *Nature* **591** (03, 2021) 564–569.

[8] S. Brewer, J.-S. Chen, A. Hankin, E. Clements, C. Chou, D. Wineland, D. Hume, and D. Leibrandt, "$^{27}Al^{+}$ Quantum-logic clock with a systematic uncertainty below 10^{-18}", *Physical Review Letters* **123** no. 3, (Jul, 2019) .

[9] W. F. McGrew, X. Zhang, R. J. Fasano, S. A. Schäffer, K. Beloy, D. Nicolodi, R. C. Brown, N. Hinkley, G. Milani, M. Schioppo, T. H. Yoon, and A. D. Ludlow, "Atomic clock performance enabling geodesy below the centimetre level", *Nature* **564** no. 7734, (Nov, 2018) 87–90.

[10] I. Ushijima, M. Takamoto, M. Das, T. Ohkubo, and H. Katori, "Cryogenic optical lattice clocks", *Nature Photonics* **9** (02, 2015) .

[11] P. Gill, "Is the time right for a redefinition of the second by optical atomic clocks?", *Journal of Physics: Conference Series* **723** no. 1, (Jun, 2016) 012053.

[12] J. Lodewyck, "On a definition of the SI second with a set of optical clock transitions", *Metrologia* **56** no. 5, (Sep, 2019) 055009.

[13] F. Riehle, P. Gill, F. Arias, and L. Robertsson, "The CIPM list of recommended frequency standard values: guidelines and procedures", *Metrologia* **55** no. 2, (Feb, 2018) 188.

[14] CCTF, "Draft resolution E - On the future redefinition of the second", 2022. https://www.bipm.org/documents/20126/73561404/CCTF+contribution+to+CGPM-Accompanying+doc-Resolution+E-June+14+2022.pdf/691a4902-27c8-5a3d-dc3d-07976eec9deb.

[15] N. Dimarcq, M. Gertsvolf, G. Mileti, S. Bize, C. W. Oates, E. Peik, D. Calonico, T. Ido, P. Tavella, F. Meynadier, G. Petit, G. Panfilo, J. Bartholomew, P. Defraigne, E. A. Donley, P. O. Hedekvist, I. Sesia, M. Wouters, P. Dube, F. Fang, F. Levi, J. Lodewyck, H. S. Margolis, D. Newell, S. Slyusarev, S. Weyers, J. P. Uzan, M. Yasuda, D. H. Yu, C. Rieck, H. Schnatz, Y. Hanado, M. Fujieda, P. E. Pottie, J. Hanssen, A. Malimon, and N. Ashby, "Roadmap towards the redefinition of the second", `arXiv:2307.14141 [physics.atom-ph]`.

[16] D. Allan, "Statistics of atomic frequency standards", *Proceedings of the IEEE* **54** no. 2, (1966) 221–230.

[17] G. Santarelli, C. Audoin, A. Makdissi, P. Laurent, G. Dick, and A. Clairon, "Frequency stability degradation of an oscillator slaved to a periodically interrogated atomic resonator", *IEEE Transactions on Ultrasonics, Ferroelectrics, and Frequency Control* **45** no. 4, (1998) 887–894.

[18] A. D. Ludlow, M. M. Boyd, J. Ye, E. Peik, and P. O. Schmidt, "Optical atomic clocks", *Rev. Mod. Phys.* **87** (Jun, 2015) 637–701.

[19] W. M. Itano, J. C. Bergquist, J. J. Bollinger, J. M. Gilligan, D. J. Heinzen, F. L. Moore, M. G. Raizen, and D. J. Wineland, "Quantum projection noise: Population fluctuations in two-level systems", *Phys. Rev. A* **47** (May, 1993) 3554–3570.

[20] G. J. Dick, "Local oscillator induced instabilities in trapped ion frequency standards", in *Proceedings of the 19th Annual Precise Time and Time Interval Systems and Applications Meeting*, pp. 133–147. 1989.

[21] M. Schioppo, R. C. Brown, W. F. McGrew, N. Hinkley, R. J. Fasano, K. Beloy, T. H. Yoon, G. Milani, D. Nicolodi, J. A. Sherman, N. B. Phillips, C. W. Oates, and A. D. Ludlow, "Ultrastable optical clock with two cold-atom ensembles", *Nature Photonics* **11** no. 1, (Nov, 2016) 48–52.

[22] M. Takamoto, T. Takano, and H. Katori, "Frequency comparison of optical lattice clocks beyond the Dick limit", *Nature Photonics* **5** (04, 2011) 288–292.

[23] P. Grangier, A. Levenson, and J.-P. Poizat, "Quantum non -demolition mesurements in optics", *Nature* **396** (12, 1998) 537–542.

[24] W. Bowden, A. Vianello, I. R. Hill, M. Schioppo, and R. Hobson, "Improving the Q Factor of an Optical Atomic Clock Using Quantum Nondemolition Measurement", *Phys. Rev. X* **10** (Dec, 2020) 041052.

[25] D. B. Orenes, R. J. Sewell, J. Lodewyck, and M. W. Mitchell, "Improving Short-Term Stability in Optical Lattice Clocks by Quantum Nondemolition Measurement", *Phys. Rev. Lett.* **128** (Apr, 2022) 153201.

[26] W. Paul, "Electromagnetic traps for charged and neutral particles", *Rev. Mod. Phys.* **62** (Jul, 1990) 531–540.

[27] H. Margolis, G. Barwood, K. Hosaka, G. Huang, H. Klein, S. Lea, A. Stannard, B. Walton, S. Webster, and P. Gill, "Trapped ion optical clocks at NPL", *AIP Conference Proceedings* **869** (11, 2006) 97–107.

[28] E. Perego, A. Detti, L. Duca, M. Pomponio, C. E. Calosso, M. D. Pas, and C. Sias, "Towards a new atom-ion experiment in Italy", *Quantum Information and Measurement (QIM) V: Quantum Technologies* (2019) F4B.3.

[29] N. Huntemann, C. Sanner, B. Lipphardt, C. Tamm, and E. Peik, "Single-ion atomic clock with 3×10^{-18} systematic uncertainty", *Phys. Rev. Lett.* **116** (Feb, 2016) 063001.

[30] T. Udem, J. Reichert, R. Holzwarth, and T. W. Hänsch, "Accurate measurement of large optical frequency differences with a mode-locked laser", *Opt. Lett.* **24** no. 13, (Jul, 1999) 881–883.

[31] T. Ideguchi, "Dual-comb spectroscopy", *Opt. Photon. News* **28** no. 1, (Jan, 2017) 32–39.

[32] S. A. Diddams, D. J. Jones, J. Ye, S. T. Cundiff, J. L. Hall, J. K. Ranka, R. S. Windeler, R. Holzwarth, T. Udem, and T. W. Hänsch, "Direct link between microwave and optical frequencies with a 300 THz femtosecond laser comb", *Phys. Rev. Lett.* **84** (May, 2000) 5102–5105.

[33] I. Goti, S. Condio, C. Clivati, M. Risaro, M. Gozzelino, G. A. Costanzo, F. Levi, D. Calonico, and M. Pizzocaro, "Absolute frequency measurement of a Yb optical clock at the limit of the Cs fountain", *Metrologia* **60** no. 3, (May, 2023) 035002.

[34] C. Thomas, "Impact of new clock technologies on the stability and accuracy of the International Atomic Time TAI", *IEEE Transactions on Ultrasonics, Ferroelectrics, and Frequency Control* **44** no. 3, (1997) 693–700.

[35] G. Panfilo and F. Arias, "The Coordinated Universal Time (UTC)", *Metrologia* **56** no. 4, (Jun, 2019) 042001.

[36] BIPM, "Circular T." https://www.bipm.org/en/time-ftp/circular-t.

[37] "IERS Bulletin C (leap second announcements)." https://datacenter.iers.org/data/latestVersion/16_BULLETIN_C16.txt.

[38] S. B. Koller, J. Grotti, S. Vogt, A. Al-Masoudi, S. Dörscher, S. Häfner, U. Sterr, and C. Lisdat, "Transportable optical lattice clock with 7×10^{-17} uncertainty", *Phys. Rev. Lett.* **118** (Feb, 2017) 073601.

[39] S. Origlia, M. S. Pramod, S. Schiller, Y. Singh, K. Bongs, R. Schwarz, A. Al-Masoudi, S. Dörscher, S. Herbers, S. Häfner, U. Sterr, and C. Lisdat, "Towards an optical clock for space: Compact, high-performance optical lattice clock based on bosonic atoms", *Phys. Rev. A* **98** (Nov, 2018) 053443.

[40] M. Takamoto, I. Ushijima, N. Ohmae, T. Yahagi, K. Kokado, H.-a. Shinkai, and H. Katori, "Test of general relativity by a pair of transportable optical lattice clocks", *Nature Photonics* **14** (07, 2020) 1–5.

[41] Y. Huang, H. Zhang, B. Zhang, Y. Hao, H. Guan, M. Zeng, Q. Chen, Y. Lin, Y. Wang, S. Cao, K. Liang, F. Fang, Z. Fang, T. Li, and K. Gao, "Geopotential measurement with a robust, transportable Ca^{+} optical clock", *Phys. Rev. A* **102** (Nov, 2020) 050802.

[42] J. Cao, J. Yuan, S. Wang, P. Zhang, Y. Yuan, D. Liu, K. Cui, S. Chao, H. Shu, Y. Lin, S. Cao, Y. Wang, Z. Fang, F. Fang, T. Li, and X. Huang, "A compact, transportable optical clock with 1×10^{-17} uncertainty and its absolute frequency measurement", *Applied Physics Letters* **120** no. 5, (02, 2022) 054003.

[43] J. Stuhler, M. Abdel Hafiz, B. Arar, A. Bawamia, K. Bergner, M. Biethahn, S. Brakhane, A. Didier, J. Fortágh, M. Halder, R. Holzwarth, N. Huntemann, M. Johanning, R. Jördens, W. Kaenders, F. Karlewski, F. Kienle, M. Krutzik, M. Lessing, T. Mehlstäubler, D. Meschede, E. Peik, A. Peters, P. Schmidt, H. Siebeneich, C. Tamm, E. Vogt, A. Wicht, C. Wunderlich, and J. Yu, "Opticlock: Transportable and easy-to-operate optical single-ion clock", *Measurement: Sensors* **18** (2021) 100264.

[44] C. W. Chou, D. B. Hume, T. Rosenband, and D. J. Wineland, "Optical clocks and relativity", *Science* **329** no. 5999, (2010) 1630–1633.

[45] H. Denker, L. Timmen, C. Voigt, S. Weyers, E. Peik, H. Margolis, P. Delva, P. Wolf, and G. Petit, "Geodetic methods to determine the relativistic redshift at the level of 10^{-18} in the context of international timescales: a review and practical results", *Journal of Geodesy* **92** (12, 2017) .

[46] J. Grotti, S. Koller, S. Vogt, S. Häfner, U. Sterr, C. Lisdat, H. Denker, C. Voigt, L. Timmen, A. Rolland, F. Baynes, H. Margolis, M. Zampaolo, P. Thoumany, M. Pizzocaro, B. Rauf, F. Bregolin, A. Tampellini, P. Barbieri, and D. Calonico, "Geodesy and metrology with a transportable optical clock", *Nature Physics* **14** (05, 2018) .

[47] E. J. Angstmann, V. A. Dzuba, and V. V. Flambaum, "Atomic clocks and the search for variation of the fine structure constant", *arXiv: Atomic Physics* (2004) .

[48] R. Lange, N. Huntemann, J. M. Rahm, C. Sanner, H. Shao, B. Lipphardt, C. Tamm, S. Weyers, and E. Peik, "Improved limits for violations of local position invariance from atomic clock comparisons", *Phys. Rev. Lett.* **126** (Jan, 2021) 011102.

[49] P. Wcislo, P. Ablewski, K. Beloy, S. Bilicki, M. Bober, R. Brown, R. Fasano, R. Ciurylo, H. Hachisu, T. Ido, J. Lodewyck, A. Ludlow, W. McGrew, P. Morzynski, D. Nicolodi, M. Schioppo, M. Sekido, R. Targat, P. Wolf, and M. Zawada, "Dark matter searches within the intercontinental optical atomic clock network", pp. 322–325. 04, 2018.

[50] A. Derevianko and M. Pospelov, "Hunting for topological dark matter with atomic clocks", *Nature Physics* **10** (11, 2013) 933–936.

[51] B. M. Roberts, P. Delva, A. Al-Masoudi, A. Amy-Klein, C. Bærentsen, C. F. A. Baynham, E. Benkler, S. Bilicki, S. Bize, W. Bowden, J. Calvert, V. Cambier, E. Cantin, E. A. Curtis, S. Dörscher, M. Favier, F. Frank, P. Gill, R. M. Godun, G. Grosche, C. Guo, A. Hees, I. R. Hill, R. Hobson, N. Huntemann, J. Kronjäger, S. Koke, A. Kuhl, R. Lange, T. Legero, B. Lipphardt, C. Lisdat, J. Lodewyck, O. Lopez, H. S. Margolis, H. Álvarez Martínez, F. Meynadier, F. Ozimek, E. Peik, P.-E. Pottie, N. Quintin, C. Sanner, L. D. Sarlo, M. Schioppo, R. Schwarz, A. Silva, U. Sterr, C. Tamm, R. L. Targat, P. Tuckey, G. Vallet, T. Waterholter, D. Xu, and P. Wolf, "Search for transient variations of the fine structure constant and dark matter using fiber-linked optical atomic clocks", *New Journal of Physics* **22** no. 9, (Sep, 2020) 093010.

[52] C. Clivati, R. Ambrosini, T. Artz, A. Bertarini, C. Bortolotti, M. Frittelli, F. Levi, A. Mura, G. Maccaferri, M. Nanni, M. Negusini, F. Perini, M. Roma, M. Stagni, M. Zucco, and D. Calonico, "A VLBI experiment using a remote atomic clock via a coherent fibre link", *Scientific Reports* **7** (Feb., 2017) 40992.

[53] T. Schuldt, M. Gohlke, M. Oswald, J. Wüst, T. Blomberg, A. Peters, A. Wicht, M. Lezius, K. Voss, M. Krutzik, S. Herrmann, and C. Braxmaier, "Optical clock technologies for Global Navigation Satellite Systems", *GPS Solutions* **25** (07, 2021) .

[54] M. A. Norcia, A. W. Young, W. J. Eckner, E. Oelker, J. Ye, and A. M. Kaufman, "Seconds-scale coherence on an optical clock transition in a tweezer array", *Science* **366** no. 6461, (2019) 93–97.

[55] A. Young, W. Eckner, W. Milner, D. Kedar, M. Norcia, E. Oelker, N. Schine, and J. Ye, "Half-minute-scale atomic coherence and high relative stability in a tweezer clock", *Nature* **588** (12, 2020) 408–413.

[56] N. Schine, A. Young, W. Eckner, and M. Martin, "Long-lived Bell states in an array of optical clock qubits", *Nature Physics* **18** no. 9, (2022) 1067–1073.

[57] L. I. R. Gil, R. Mukherjee, E. M. Bridge, M. P. A. Jones, and T. Pohl, "Spin squeezing in a Rydberg lattice clock", *Phys. Rev. Lett.* **112** (Mar, 2014) 103601.

[58] J. Kitching, "Chip-scale atomic devices", *Applied Physics Reviews* **5** no. 3, (08, 2018) 031302.

[59] M. Travagnin, "Chip-scale atomic clocks physics, technologies, and applications", *JRC Technical Reports* (02, 2022) .

[60] Z. L. Newman, V. Maurice, T. Drake, J. R. Stone, T. C. Briles, D. T. Spencer, C. Fredrick, Q. Li, D. Westly, B. R. Ilic, B. Shen, M.-G. Suh, K. Y. Yang, C. Johnson, D. M. S. Johnson, L. Hollberg, K. J. Vahala, K. Srinivasan, S. A. Diddams, J. Kitching, S. B. Papp, and M. T. Hummon, "Architecture for the photonic integration of an optical atomic clock", *Optica* **6** no. 5, (May, 2019) 680–685.

[61] V. Maurice, Z. Newman, S. Dickerson, M. Rivers, P. Greene, M. Mescher, J. Hsiao, J. Kitching, M. Hummon, and C. Johnson, "Miniaturized optical frequency standard for next-generation portable optical clocks", *Optics Express* **28** (07, 2020) .

[62] M. Corato-Zanarella, A. Molina, X. Ji, M. Shin, A. Mohanty, and M. Lipson, "Widely tunable and narrow-linewidth chip-scale lasers from near-ultraviolet to near-infrared wavelengths", *Nature Photonics* **17** (12, 2022) 1–8.

[63] L. Von der Wense and B. Seiferle, "The ^{229}Th isomer: prospects for a nuclear optical clock", *Eur. Phys. J. A* **56** no. 11, (09, 2020) .

[64] E. Peik, T. Schumm, M. S. Safronova, A. Pálffy, J. Weitenberg, and P. G. Thirolf, "Nuclear clocks for testing fundamental physics", *Quantum Science and Technology* **6** no. 3, (Apr, 2021) 034002.

[65] V. V. Flambaum, "Enhanced effect of temporal variation of the fine structure constant and the strong interaction in ^{229}Th", *Phys. Rev. Lett.* **97** (Aug, 2006) 092502.

[66] V. V. Flambaum and A. F. Tedesco, "Dependence of nuclear magnetic moments on quark masses and limits on temporal variation of fundamental constants from atomic clock experiments", *Phys. Rev. C* **73** (May, 2006) 055501.

[67] C.-Y. Xu, J. Singh, J. C. Zappala, K. G. Bailey, M. R. Dietrich, J. P. Greene, W. Jiang, N. D. Lemke, Z.-T. Lu, P. Mueller, and T. P. O'Connor, "Measurement of the hyperfine quenching rate of the clock transition in ^{171}Yb", *Phys. Rev. Lett.* **113** (Jul, 2014) 033003.

[68] M. Pizzocaro, P. Thoumany, B. Rauf, F. Bregolin, G. Milani, C. Clivati, G. A. Costanzo, F. Levi, and D. Calonico, "Absolute frequency measurement of the transition $^1S_0 \rightarrow ^3P_0$ of ^{171}Yb", *Metrologia* **54** no. 1, (Jan, 2017) 102–112.

[69] H. Katori, M. Takamoto, V. G. Pal'chikov, and V. D. Ovsiannikov, "Ultrastable optical clock with neutral atoms in an engineered light shift trap", *Phys. Rev. Lett.* **91** (Oct, 2003) 173005.

[70] S. G. Porsev, A. Derevianko, and E. N. Fortson, "Possibility of an optical clock using the $6^1S_0 \rightarrow 6^3P_0$ transition in ^{171,173}Yb atoms held in an optical lattice", *Phys. Rev. A* **69** (Feb, 2004) 021403.

[71] F. Bregolin, *"^{171}Yb optical frequency standards towards the redefinition of the second"*. PhD thesis, Politecnico di Torino, 2019.

[72] R. Drever, J. Hall, F. Kowalski, J. Hough, G. Ford, A. Munley, and H. Ward, "Laser phase and frequency stabilization using an optical resonator", *Appl. Phys. B* **31** (06, 1983) 97–105.

[73] E. Black, "An introduction to Pound-Drever-Hall laser frequency stabilization", *American Journal of Physics* **69** (01, 2001) 79–87.

[74] W. Demtröder, *Laser spectroscopy 1: Basic principles*. 11, 2013.

[75] M. Pizzocaro, D. Calonico, P. C. Pastor, J. Catani, G. A. Costanzo, F. Levi, and L. Lorini, "Efficient frequency doubling at 399 nm", *Appl. Opt.* **53** no. 16, (Jun, 2014) 3388–3392.

[76] T. Haensch and B. Couillaud, "Laser frequency stabilization by polarization spectroscopy of a reflecting reference cavity", *Optics Communications* **35** (12, 1980) 441–444.

[77] S. Condio, "Optical lattice clock with an amplified laser diode", Master's thesis, Università degli Studi di Torino, 2020.

[78] G. Milani, *"Realization of advanced ^{171}Yb optical lattice frequency standard"*. PhD thesis, Politecnico di Torino, 2018.

[79] J. I. Thorpe, K. Numata, and J. Livas, "Laser frequency stabilization and control through offset sideband locking to optical cavities", *Opt. Express* **16** no. 20, (Sep, 2008) 15980–15990.

[80] M. Schioppo, N. Poli, M. Prevedelli, S. Falke, C. Lisdat, U. Sterr, and G. M. Tino, "A compact and efficient strontium oven for laser-cooling experiments", *Review of Scientific Instruments* **83** no. 10, (10, 2012) 103101.

[81] T. Ohkubo, *"Frequency ratio measurement of ytterbium/strontium optical lattice clocks"*. PhD thesis, University of Tokyo, 2016.

[82] M. Pizzocaro, *"Realization and characterization of optical frequency standards"*. PhD thesis, Politecnico di Torino, 2013.

[83] W. D. Phillips and H. Metcalf, "Laser deceleration of an atomic beam", *Phys. Rev. Lett.* **48** (Mar, 1982) 596–599.

[84] S. Zhang, P. Ramchurn, M. Menchetti, Q. Ubaid, J. Jones, K. Bongs, and Y. Singh, "Novel repumping on $^3P_0 \rightarrow ^3 D_1$ for Sr magneto-optical trap and landé g factor measurement of $^3D_1$", *Journal of Physics B: Atomic, Molecular and Optical Physics* **53** no. 23, (Oct, 2020) 235301.

[85] H. Metcalf and P. van der Straten, "Laser cooling and trapping", *Journal of the Optical Society of America B* **20** (05, 2003) .

[86] M. Inguscio and L. Fallani, *Atomic Physics: Precise Measurements and Ultracold Matter*. Oxford University Press, 09, 2013.

[87] W. D. Phillips, "Nobel Lecture: Laser cooling and trapping of neutral atoms", *Rev. Mod. Phys.* **70** (Jul, 1998) 721–741.

[88] D. J. Wineland and W. M. Itano, "Laser cooling of atoms", *Phys. Rev. A* **20** (Oct, 1979) 1521–1540.

[89] F. Diedrich, J. C. Bergquist, W. M. Itano, and D. J. Wineland, "Laser cooling to the zero-point energy of motion", *Phys. Rev. Lett.* **62** (Jan, 1989) 403–406.

[90] R. Grimm, M. Weidemüller, and Y. B. Ovchinnikov, "Optical dipole traps for neutral atoms", vol. 42 of *Advances In Atomic, Molecular, and Optical Physics*, pp. 95–170. Academic Press, 2000.

[91] I. Goti, "Towards the production of ultracold mixtures of lithium and chromium atoms", Master's thesis, Università degli Studi di Firenze, 2019.

[92] M. Pizzocaro, F. Bregolin, P. Barbieri, B. Rauf, F. Levi, and D. Calonico, "Absolute frequency measurement of the $^1S_0 \rightarrow ^3 P_0$ transition of ^{171}Yb with a link to international atomic time", *Metrologia* **57** (10, 2019) .

[93] S. Blatt, J. W. Thomsen, G. K. Campbell, A. D. Ludlow, M. D. Swallows, M. J. Martin, M. M. Boyd, and J. Ye, "Rabi spectroscopy and excitation inhomogeneity in a one-dimensional optical lattice clock", *Phys. Rev. A* **80** (Nov, 2009) 052703.

[94] T. Bothwell, D. Kedar, E. Oelker, J. M. Robinson, S. L. Bromley, W. L. Tew, J. Ye, and C. J. Kennedy, "JILA SrI optical lattice clock with uncertainty of 2×10^{-18}", *Metrologia* **56** no. 6, (Oct, 2019) 065004.

[95] N. D. Lemke, J. von Stecher, J. A. Sherman, A. M. Rey, C. W. Oates, and A. D. Ludlow, "p-Wave cold collisions in an optical lattice clock", *Phys. Rev. Lett.* **107** (Aug, 2011) 103902.

[96] N. Nemitz, A. A. Jørgensen, R. Yanagimoto, F. Bregolin, and H. Katori, "Modeling light shifts in optical lattice clocks", *Phys. Rev. A* **99** (Mar, 2019) 033424.

[97] T. L. Nicholson, M. J. Martin, J. R. Williams, B. J. Bloom, M. Bishof, M. D. Swallows, S. L. Campbell, and J. Ye, "Comparison of two independent Sr optical clocks with 1×10^{-17} stability at 10^3 s", *Phys. Rev. Lett.* **109** (Dec, 2012) 230801.

[98] K. Gibble and B. J. Verhaar, "Eliminating cold-collision frequency shifts", *Phys. Rev. A* **52** (Oct, 1995) 3370–3373.

[99] B. DeMarco, J. L. Bohn, J. P. Burke, M. Holland, and D. S. Jin, "Measurement of p-wave threshold law using evaporatively cooled fermionic atoms", *Phys. Rev. Lett.* **82** (May, 1999) 4208–4211.

[100] A. M. Rey, A. V. Gorshkov, and C. Rubbo, "Many-body treatment of the collisional frequency shift in fermionic atoms", *Phys. Rev. Lett.* **103** (Dec, 2009) 260402.

[101] S. Lee, C. Y. Park, W.-K. Lee, and D.-H. Yu, "Cancellation of collisional frequency shifts in optical lattice clocks with Rabi spectroscopy", *New Journal of Physics* **18** no. 3, (Mar, 2016) 033030.

[102] R. Yanagimoto, N. Nemitz, F. Bregolin, and H. Katori, "Decomposed description of Ramsey spectra under atomic interactions", *Phys. Rev. A* **98** (Jul, 2018) 012704.

[103] M. Martin, M. Bishof, M. Swallows, X. Zhang, C. Benko, J. von Stecher, A. Gorshkov, A. Rey, and J. Ye, "A quantum many-body spin system in an optical lattice clock", *Science (New York, N.Y.)* **341** (08, 2013) 632–6.

[104] A. Aeppli, A. Chu, T. Bothwell, C. Kennedy, D. Kedar, P. He, A. Rey, and J. Ye, "Hamiltonian engineering of spin-orbit-coupled fermions in a Wannier-Stark optical lattice clock", *Science advances* **8** (10, 2022) .

[105] J. Lodewyck, M. Zawada, L. Lorini, M. Gurov, and P. Lemonde, "Observation and cancellation of a perturbing dc stark shift in strontium optical lattice clocks", *IEEE transactions on ultrasonics, ferroelectrics, and frequency control* **59** (03, 2012) 411–5.

[106] J. A. Sherman, N. D. Lemke, N. Hinkley, M. Pizzocaro, R. W. Fox, A. D. Ludlow, and C. W. Oates, "High-accuracy measurement of atomic polarizability in an optical lattice clock", *Phys. Rev. Lett.* **108** (Apr, 2012) 153002.

[107] K. Beloy, X. Zhang, W. F. McGrew, N. Hinkley, T. H. Yoon, D. Nicolodi, R. J. Fasano, S. A. Schäffer, R. C. Brown, and A. D. Ludlow, "Faraday-shielded dc Stark-shift-free optical lattice clock", *Phys. Rev. Lett.* **120** (May, 2018) 183201.

[108] BIPM, IEC, IFCC, ILAC, ISO, IUPAC, IUPAP, and OIML, "Evaluation of measurement data - Supplement 1 to the "Guide to the expression of uncertainty in measurement" - Propagation of distributions using a Monte Carlo method." Joint committee for guides in metrology, jcgm 101, 2008. http://www.bipm.org/en/publications/guides/gum.html.

[109] S. E. Pollack, M. D. Turner, S. Schlamminger, C. A. Hagedorn, and J. H. Gundlach, "Charge management for gravitational-wave observatories using UV LEDs", *Phys. Rev. D* **81** (Jan, 2010) 021101.

[110] D. Ugolini, M. Girard, G. Harry, and V. Mitrofanov, "Discharging fused silica test masses with ultraviolet light", *Physics Letters A* **372** no. 36, (2008) 5741–5744.

[111] M. Hewitson, K. Danzmann, H. Grote, S. Hild, J. Hough, H. Lück, S. Rowan, J. R. Smith, K. A. Strain, and B. Willke, "Charge measurement and mitigation for the main test masses of the GEO 600 gravitational wave observatory", *Classical and Quantum Gravity* **24** no. 24, (Nov, 2007) 6379.

[112] M. Harlander, M. Brownnutt, W. Hänsel, and R. Blatt, "Trapped-ion probing of light-induced charging effects on dielectrics", *New Journal of Physics* **12** no. 9, (Sep, 2010) 093035.

[113] T. Lindvall, K. J. Hanhijärvi, T. Fordell, and A. E. Wallin, "High-accuracy determination of Paul-trap stability parameters for electric-quadrupole-shift prediction", *Journal of Applied Physics* **132** no. 12, (Sep, 2022) .

[114] A. V. Taichenachev, V. I. Yudin, V. D. Ovsiannikov, V. G. Pal'chikov, and C. W. Oates, "Frequency shifts in an optical lattice clock due to magnetic-dipole and electric-quadrupole transitions", *Phys. Rev. Lett.* **101** (Nov, 2008) 193601.

[115] A. Derevianko and H. Katori, "Colloquium: Physics of optical lattice clocks", *Rev. Mod. Phys.* **83** (May, 2011) 331–347.

[116] Z. W. Barber, J. E. Stalnaker, N. D. Lemke, N. Poli, C. W. Oates, T. M. Fortier, S. A. Diddams, L. Hollberg, C. W. Hoyt, A. V. Taichenachev, and V. I. Yudin, "Optical lattice induced light shifts in an Yb atomic clock", *Phys. Rev. Lett.* **100** (Mar, 2008) 103002.

[117] H. Katori, V. D. Ovsiannikov, S. I. Marmo, and V. G. Palchikov, "Strategies for reducing the light shift in atomic clocks", *Phys. Rev. A* **91** (May, 2015) 052503.

[118] N. Nemitz, T. Ohkubo, M. Takamoto, I. Ushijima, M. Das, N. Ohmae, and H. Katori, "Frequency ratio of Yb and Sr clocks with 5×10^{-17} uncertainty at 150 s averaging time", *Nature Photonics* **10** (01, 2016) .

[119] V. D. Ovsiannikov, S. I. Marmo, V. G. Palchikov, and H. Katori, "Higher-order effects on the precision of clocks of neutral atoms in optical lattices", *Phys. Rev. A* **93** (Apr, 2016) 043420.

[120] I. Ushijima, M. Takamoto, and H. Katori, "Operational magic intensity for Sr optical lattice clocks", *Phys. Rev. Lett.* **121** (Dec, 2018) 263202.

[121] R. C. Brown, N. B. Phillips, K. Beloy, W. F. McGrew, M. Schioppo, R. J. Fasano, G. Milani, X. Zhang, N. Hinkley, H. Leopardi, T. H. Yoon, D. Nicolodi, T. M. Fortier, and A. D. Ludlow, "Hyperpolarizability and operational magic wavelength in an optical lattice clock", *Phys. Rev. Lett.* **119** (Dec, 2017) 253001.

[122] K. Beloy, W. F. McGrew, X. Zhang, D. Nicolodi, R. J. Fasano, Y. S. Hassan, R. C. Brown, and A. D. Ludlow, "Modeling motional energy spectra and lattice light shifts in optical lattice clocks", *Phys. Rev. A* **101** (May, 2020) 053416.

[123] Z. W. Barber, C. W. Hoyt, C. W. Oates, L. Hollberg, A. V. Taichenachev, and V. I. Yudin, "Direct excitation of the forbidden clock transition in neutral ^{174}Yb atoms confined to an optical lattice", *Phys. Rev. Lett.* **96** (Mar, 2006) 083002.

[124] L.-S. Ma, P. Jungner, J. Ye, and J. L. Hall, "Delivering the same optical frequency at two places: accurate cancellation of phase noise introduced by an optical fiber or other time-varying path", *Opt. Lett.* **19** no. 21, (Nov, 1994) 1777–1779.

[125] P. A. Williams, W. C. Swann, and N. R. Newbury, "High-stability transfer of an optical frequency over long fiber-optic links", *J. Opt. Soc. Am. B* **25** no. 8, (Aug, 2008) 1284–1293.

[126] M. Takamoto, F.-L. Hong, R. Higashi, Y. Fujii, M. Imae, and H. Katori, "Improved frequency measurement of a one-dimensional optical lattice clock with a spin-polarized fermionic ^{87}Sr isotope", *J. Phys. Soc. Jpn.* **75** (Aug, 2006) .

[127] N. Ohmae, F. Bregolin, N. Nemitz, and H. Katori, "Direct measurement of the frequency ratio for Hg and Yb optical lattice clocks and closure of the Hg/Yb/Sr loop", *Opt. Express* **28** no. 10, (May, 2020) 15112–15121.

[128] T. Kobayashi, D. Akamatsu, Y. Hisai, T. Tanabe, H. Inaba, T. Suzuyama, F.-L. Hong, K. Hosaka, and M. Yasuda, "Uncertainty Evaluation of an ^{171}Yb Optical Lattice Clock at NMIJ", *IEEE Transactions on Ultrasonics, Ferroelectrics, and Frequency Control* **PP** (09, 2018) 1–1.

[129] C. Shi, J.-L. Robyr, U. Eismann, M. Zawada, L. Lorini, R. Le Targat, and J. Lodewyck, "Polarizabilities of the ^{87}Sr clock transition", *Phys. Rev. A* **92** (Jul, 2015) 012516.

[130] M. V. Romalis and E. N. Fortson, "Zeeman frequency shifts in an optical dipole trap used to search for an electric-dipole moment", *Phys. Rev. A* **59** (Jun, 1999) 4547–4558.

[131] K. Beloy, N. Hinkley, N. B. Phillips, J. A. Sherman, M. Schioppo, J. Lehman, A. Feldman, L. M. Hanssen, C. W. Oates, and A. D. Ludlow, "Atomic clock with 1×10^{-18} room-temperature blackbody stark uncertainty", *Phys. Rev. Lett.* **113** (Dec, 2014) 260801.

[132] T. Middelmann, C. Lisdat, S. Falke, J. S. R. Vellore Winfred, F. Riehle, and U. Sterr, "Tackling the blackbody shift in a Strontium optical lattice clock", *IEEE Transactions on Instrumentation and Measurement* **60** no. 7, (2011) 2550–2557.

[133] M. Abdel-Hafiz, P. Ablewski, A. Al-Masoudi, H. A. Martínez, P. Balling, G. Barwood, E. Benkler, M. Bober, M. Borkowski, W. Bowden, R. Ciuryło, H. Cybulski, A. Didier, M. Doležal, S. Dörscher, S. Falke, R. M. Godun, R. Hamid, I. R. Hill, R. Hobson, N. Huntemann, Y. Le Coq, R. Le Targat, T. Legero, T. Lindvall, C. Lisdat, J. Lodewyck, H. S. Margolis, T. E. Mehlstäubler, E. Peik, L. Pelzer, M. Pizzocaro, B. Rauf, A. Rolland, N. Scharnhorst, M. Schioppo, P. O. Schmidt, R. Schwarz, Ç. Şenel, N. Spethmann, U. Sterr, C. Tamm, J. W. Thomsen, A. Vianello, and M. Zawada, "Guidelines for developing optical clocks with 10^{-18} fractional frequency uncertainty", *arXiv preprint arXiv:1906.11495* (2019) .

[134] P. Ablewski, M. Bober, and M. Zawada, "Emissivities of vacuum compatible materials: towards minimising blackbody radiation shift uncertainty in optical atomic clocks at room temperatures", *Metrologia* **57** no. 3, (May, 2020) 035004.

[135] M. Barbiero, M. G. Tarallo, D. Calonico, F. Levi, G. Lamporesi, and G. Ferrari, "Sideband-enhanced cold atomic source for optical clocks", *Phys. Rev. Appl.* **13** (Jan, 2020) 014013.

[136] G. Lamporesi, S. Donadello, S. Serafini, and G. Ferrari, "Compact high-flux source of cold sodium atoms", *Review of Scientific Instruments* **84** no. 6, (06, 2013) 063102.

[137] K. Gibble, "Scattering of cold-atom coherences by hot atoms: Frequency shifts from background-gas collisions", *Phys. Rev. Lett.* **110** (May, 2013) 180802.

[138] K. Gibble, "Scattering of cold-atom coherences by hot atoms: Frequency shifts from background-gas collisions", *Phys. Rev. Lett.* **110** (May, 2013) 180802.

[139] S. G. Porsev, M. S. Safronova, A. Derevianko, and C. W. Clark, "Long-range interaction coefficients for ytterbium dimers", *Phys. Rev. A* **89** (Jan, 2014) 012711.

[140] M. G. Tarallo, D. Calonico, F. Levi, M. Barbiero, G. Lamporesi, and G. Ferrari, "A strontium optical lattice clock apparatus for precise frequency metrology and beyond", *2017 Joint Conference of the European Frequency and Time Forum and IEEE International Frequency Control Symposium (EFTF/IFCS)* (2017) 748–750.

[141] T. G. Tiecke, S. D. Gensemer, A. Ludewig, and J. T. M. Walraven, "High-flux two-dimensional magneto-optical-trap source for cold lithium atoms", *Phys. Rev. A* **80** (Jul, 2009) 013409.

[142] P. Lemonde and P. Wolf, "Optical lattice clock with atoms confined in a shallow trap", *Phys. Rev. A* **72** (Sep, 2005) 033409.

[143] G. Nenciu, "Dynamics of band electrons in electric and magnetic fields: rigorous justification of the effective Hamiltonians", *Rev. Mod. Phys.* **63** (Jan, 1991) 91–127.

[144] S. Falke, M. Misera, U. Sterr, and C. Lisdat, "Delivering pulsed and phase stable light to atoms of an optical clock", *Applied Physics B: Lasers and Optics* **107** no. 2, (May, 2012) 301–311.

[145] P. G. Westergaard, *"Strontium Optical Lattice Clock: In Quest of the Ultimate Performance"*. PhD thesis, Edite De Paris, 2010.

[146] R. F. C. Vessot, M. W. Levine, E. M. Mattison, E. L. Blomberg, T. E. Hoffman, G. U. Nystrom, B. F. Farrel, R. Decher, P. B. Eby, C. R. Baugher, J. W. Watts, D. L. Teuber, and F. D. Wills, "Test of relativistic gravitation with a space-borne hydrogen maser", *Phys. Rev. Lett.* **45** (Dec, 1980) 2081–2084.

[147] BIPM, "On the definition of time scales." https://www.bipm.org/en/committees/cg/cgpm/26-2018/resolution-2.

[148] H. Hachisu, G. Petit, F. Nakagawa, Y. Hanado, and T. Ido, "SI-traceable measurement of an optical frequency at the low 10−16 level without a local primary standard", *Opt. Express* **25** no. 8, (Apr, 2017) 8511–8523.

[149] M. Schioppo, J. Kronjaeger, A. Silva, R. Ilieva, J. Paterson, C. Baynham, W. Bowden, I. Hill, R. Hobson, A. Vianello, M. Dovale Álvarez, R. Williams, G. Marra, H. Margolis, A. Amy-Klein, O. Lopez, E. Cantin, H. Álvarez Martínez, R. Targat, and G. Grosche, "Comparing ultrastable lasers at 7×10^{-17} fractional frequency instability through a 2220 km optical fibre network", *Nature Communications* **13** (01, 2022) .

[150] C. Clivati, M. Pizzocaro, E. Bertacco, S. Condio, G. Costanzo, S. Donadello, I. Goti, M. Gozzelino, F. Levi, A. Mura, M. Risaro, D. Calonico, M. Tønnes, B. Pointard, M. Mazouth-Laurol, R. Le Targat, M. Abgrall, M. Lours, H. Le Goff, L. Lorini, P.-E. Pottie, E. Cantin, O. Lopez, C. Chardonnet, and A. Amy-Klein, "Coherent optical-fiber link across Italy and France", *Phys. Rev. Appl.* **18** (Nov, 2022) 054009.

[151] D. Calonico, E. Bertacco, C. Calosso, C. Clivati, G. Costanzo, M. Frittelli, A. Godone, A. Mura, N. Poli, D. Sutyrin, *et al.*, "High-accuracy coherent optical frequency transfer over a doubled 642-km fiber link", *Applied Physics B* **117** (2014) 979–986.

[152] C. Lisdat, G. Grosche, N. Quintin, C. Shi, S. Raupach, C. Grebing, D. Nicolodi, F. Stefani, A. Al-Masoudi, S. Dörscher, S. Häfner, J.-L. Robyr, N. Chiodo, S. Bilicki, E. Bookjans, A. Koczwara, S. Koke, A. Kuhl, F. Wiotte, and P.-E. Pottie, "A clock network for geodesy and fundamental science", *Nature Communications* **7** (11, 2015) .

[153] F. Lahaye, G. Cerretto, and P. Tavella, "GNSS geodetic techniques for time and frequency transfer applications", *Advances in Space Research* **47** (01, 2011) 253–264.

[154] G. Petit, "Sub-10^{-16} accuracy GNSS frequency transfer with IPPP", *GPS Solutions* **25** (01, 2021) .

[155] H. Schuh and D. Behrend, "VLBI: A fascinating technique for geodesy and astrometry", *Journal of Geodynamics* **61** (10, 2012) 68–80.

[156] N. D. Lemke, A. D. Ludlow, Z. W. Barber, T. M. Fortier, S. A. Diddams, Y. Jiang, S. R. Jefferts, T. P. Heavner, T. E. Parker, and C. W. Oates, "Spin-$1/2$ optical lattice clock", *Phys. Rev. Lett.* **103** (Aug, 2009) 063001.

[157] T. Kohno, M. Yasuda, K. Hosaka, H. Inaba, Y. Nakajima, and F.-L. Hong, "One-dimensional optical lattice clock with a fermionic ^{171}Yb isotope", *Applied Physics Express* **2** no. 7, (Jun, 2009) 072501.

[158] M. Yasuda, H. Inaba, T. Kohno, T. Tanabe, Y. Nakajima, K. Hosaka, D. Akamatsu, A. Onae, T. Suzuyama, M. Amemiya, and F.-L. Hong, "Improved absolute frequency measurement of the ^{171}Yb optical lattice clock towards a candidate for the redefinition of the second", *Applied Physics Express* **5** no. 10, (Sep, 2012) 102401.

[159] T. Kobayashi, D. Akamatsu, K. Hosaka, Y. Hisai, M. Wada, H. Inaba, T. Suzuyama, F.-L. Hong, and M. Yasuda, "Demonstration of the nearly continuous operation of an ^{171}Yb optical lattice clock for half a year", *Metrologia* **57** no. 6, (Nov, 2020) 065021.

[160] C. Y. Park, D.-H. Yu, W.-K. Lee, S. E. Park, E. B. Kim, S. K. Lee, J. W. Cho, T. H. Yoon, J. Mun, S. J. Park, T. Y. Kwon, and S.-B. Lee, "Absolute frequency measurement of $^1\mathrm{S}_0(F = 1/2) \rightarrow {}^3\mathrm{P}_0(F = 1/2)$ transition of

^{171}Yb atoms in a one-dimensional optical lattice at KRISS", *Metrologia* **50** no. 2, (Feb, 2013) 119.

[161] H. Kim, M.-S. Heo, W.-K. Lee, C. Y. Park, H.-G. Hong, S.-W. Hwang, and D.-H. Yu, "Improved absolute frequency measurement of the ^{171}Yb optical lattice clock at KRISS relative to the SI second", *Japanese Journal of Applied Physics* **56** no. 5, (Mar, 2017) 050302.

[162] H. Kim, M.-S. Heo, C. Y. Park, D.-H. Yu, and W.-K. Lee, "Absolute frequency measurement of the ^{171}Yb optical lattice clock at KRISS using TAI for over a year", *Metrologia* **58** no. 5, (Aug, 2021) 055007.

[163] L. Luo, H. Qiao, D. Ai, M. Zhou, S. Zhang, S. Zhang, C. Sun, Q. Qi, C. Peng, T. Jin, W. Fang, Z. Yang, T. Li, K. Liang, and X. Xu, "Absolute frequency measurement of an Yb optical clock at the 10^{-16} level using International Atomic Time", *Metrologia* **57** no. 6, (Oct, 2020) 065017.

[164] M. Pizzocaro, M. Sekido, K. Takefuji, H. Ujihara, H. Hachisu, N. Nemitz, M. Tsutsumi, T. Kondo, E. Kawai, R. Ichikawa, K. Namba, Y. Okamoto, R. Takahashi, J. Komuro, C. Clivati, F. Bregolin, P. Barbieri, A. Mura, E. C. Cantoni, and T. Ido, "Intercontinental comparison of optical atomic clocks through very long baseline interferometry", *Nature Physics* **17** (02, 2021) 1–5.

[165] J. Millo, M. Abgrall, M. Lours, E. English, H.-F. Jiang, J. Guéna, A. Clairon, M. Tobar, S. Bize, Y. Le Coq, and G. Santarelli, "Ultralow noise microwave generation with fiber-based optical frequency comb and application to atomic fountain clock", *Appl. Phys. Lett.* **94** (04, 2009) 141105.

[166] B. Lipphardt, V. Gerginov, and S. Weyers, "Optical stabilization of a microwave oscillator for fountain clock interrogation", *IEEE Transactions on Ultrasonics, Ferroelectrics, and Frequency Control* **64** no. 4, (Apr, 2017) 761–766.

[167] Consultative Committee for Time and Frequency (CCTF), "Recommendation CCTF PSFS 2: Updates to the CIPM list of standard frequencies", 2021. https://www.bipm.org/en/committees/cc/cctf/22-_2-2021.

[168] J. Lodewyck, R. Le Targat, P.-E. Pottie, E. Benkler, S. Koke, and J. Kronjäger, "Universal formalism for data sharing and processing in clock comparison networks", *Phys. Rev. Res.* **2** (Nov, 2020) 043269.

[169] J. Guéna, M. Abgrall, A. Clairon, and S. Bize, "Contributing to TAI with a secondary representation of the SI second", *Metrologia* **51** no. 1, (Jan, 2014) 108.

[170] T. Kobayashi, A. Takamizawa, D. Akamatsu, A. Kawasaki, A. Nishiyama, K. Hosaka, Y. Hisai, M. Wada, H. Inaba, T. Tanabe, and M. Yasuda, "Search for ultralight dark matter from long-term frequency comparisons of optical and microwave atomic clocks", *Phys. Rev. Lett.* **129** (Dec, 2022) 241301.

[171] W. F. McGrew, X. Zhang, H. Leopardi, R. J. Fasano, D. Nicolodi, K. Beloy, J. Yao, J. A. Sherman, S. A. Schäffer, J. Savory, R. C. Brown, S. Römisch, C. W. Oates, T. E. Parker, T. M. Fortier, and A. D. Ludlow, "Towards the optical second: verifying optical clocks at the SI limit", *Optica* **6** no. 4, (Apr, 2019) 448–454.

[172] D.-H. Yu, M. Weiss, and T. E. Parker, "Uncertainty of a frequency comparison with distributed dead time and measurement interval offset", *Metrologia* **44** no. 1, (Feb, 2007) 91.

[173] H. Hachisu and T. Ido, "Intermittent optical frequency measurements to reduce the dead time uncertainty of frequency link", *Japanese Journal of Applied Physics* **54** no. 11, (Oct, 2015) 112401.

[174] C. Grebing, A. Al-Masoudi, S. Dörscher, S. Häfner, V. Gerginov, S. Weyers, B. Lipphardt, F. Riehle, U. Sterr, and C. Lisdat, "Realization of a timescale with an accurate optical lattice clock", *Optica* **3** no. 6, (Jun, 2016) 563–569.

[175] BIPM, "IT-Yb1 contributions to TAI." https://webtai.bipm.org/ftp/pub/tai/other-products/taipsfs/it_yb1-ftai.

[176] BIPM, "Report submitted to BIPM." https://www.bipm.org/en/time-ftp/data.

[177] BIPM, "PSFS contributions to TAI." https://webtai.bipm.org/database/show_psfs.html.

[178] BIPM, "BIPM Time Department DataBase." https://webtai.bipm.org/database/d_plot.html.

[179] BIPM, "Time and Frequency data." https://www.bipm.org/en/time-ftp/other-products.

[180] W. Guerin, T. Rouabah, and R. Kaiser, "Light interacting with atomic ensembles: collective, cooperative and mesoscopic effects", *Journal of Modern Optics* **64, 2017** (05, 2016) 895–907.

[181] A. Glicenstein, G. Ferioli, L. Brossard, Y. R. P. Sortais, D. Barredo, F. Nogrette, I. Ferrier-Barbut, and A. Browaeys, "Preparation of one-dimensional chains and dense cold atomic clouds with a high numerical aperture four-lens system", *Phys. Rev. A* **103** (Apr, 2021) 043301.

[182] A. Glicenstein, G. Ferioli, N. Šibalić, L. Brossard, I. Ferrier-Barbut, and A. Browaeys, "Collective shift in resonant light scattering by a one-dimensional atomic chain", *Phys. Rev. Lett.* **124** (Jun, 2020) 253602.

[183] A. Glicenstein, G. Ferioli, A. Browaeys, and I. Ferrier-Barbut, "From superradiance to subradiance: exploring the many-body Dicke ladder", *Opt. Lett.* **47** no. 6, (Mar, 2022) 1541–1544.

[184] N. Skribanowitz, I. P. Herman, J. C. MacGillivray, and M. S. Feld, "Observation of Dicke superradiance in optically pumped HF gas", *Phys. Rev. Lett.* **30** (Feb, 1973) 309–312.

[185] M. O. Araújo, I. Krešić, R. Kaiser, and W. Guerin, "Superradiance in a large and dilute cloud of cold atoms in the linear-optics regime", *Phys. Rev. Lett.* **117** (Aug, 2016) 073002.

[186] D. Das, B. Lemberger, and D. D. Yavuz, "Subradiance and superradiance-to-subradiance transition in dilute atomic clouds", *Phys. Rev. A* **102** (Oct, 2020) 043708.

[187] R. G. DeVoe and R. G. Brewer, "Observation of superradiant and subradiant spontaneous emission of two trapped ions", *Phys. Rev. Lett.* **76** (Mar, 1996) 2049–2052.

[188] A. Cipris, N. A. Moreira, T. S. do Espirito Santo, P. Weiss, C. J. Villas-Boas, R. Kaiser, W. Guerin, and R. Bachelard, "Subradiance with saturated atoms: Population enhancement of the long-lived states", *Phys. Rev. Lett.* **126** (Mar, 2021) 103604.

[189] L. Ostermann, H. Ritsch, and C. Genes, "Protected state enhanced quantum metrology with interacting two-level ensembles", *Phys. Rev. Lett.* **111** (Sep, 2013) 123601.

[190] D. Plankensteiner, L. Ostermann, H. Ritsch, and C. Genes, "Selective protected state preparation of coupled dissipative quantum emitters", *Scientific Reports* **5** (04, 2015) .

[191] S. Bromley, B. Zhu, M. Bishof, X. Zhang, T. Bothwell, J. Schachenmayer, T. Nicholson, R. Kaiser, S. Yelin, M. Lukin, A. Rey, and J. Ye, "Collective atomic scattering and motional effects in a dense coherent medium", *Nature Communications* **7** (03, 2016) 11039.

[192] L. Henriet, J. S. Douglas, D. E. Chang, and A. Albrecht, "Critical open-system dynamics in a one-dimensional optical-lattice clock", *Phys. Rev. A* **99** (Feb, 2019) 023802.

[193] M. Norcia, M. Winchester, J. Cline, and J. Thompson, "Superradiance on the millihertz linewidth strontium clock transition", *Science Advances* **2** (03, 2016) .

[194] Y. Zhang, C. Shan, and K. Mølmer, "Active frequency measurement on superradiant strontium clock transitions", *Phys. Rev. Lett.* **128** (Jan, 2022) 013604.

[195] M. O. Brown, T. Thiele, C. Kiehl, T.-W. Hsu, and C. A. Regal, "Gray-molasses optical-tweezer loading: Controlling collisions for scaling atom-array assembly", *Phys. Rev. X* **9** (Mar, 2019) 011057.

[196] N. Bruno, L. C. Bianchet, V. Prakash, N. Li, N. Alves, and M. W. Mitchell, "Maltese cross coupling to individual cold atoms in free space", *Opt. Express* **27** no. 21, (Oct, 2019) 31042–31052.

[197] Y. R. P. Sortais, A. Fuhrmanek, R. Bourgain, and A. Browaeys, "Sub-poissonian atom-number fluctuations using light-assisted collisions", *Phys. Rev. A* **85** (Mar, 2012) 035403.

[198] G. Ferioli, A. Glicenstein, F. Robicheaux, R. T. Sutherland, A. Browaeys, and I. Ferrier-Barbut, "Laser-driven superradiant ensembles of two-level atoms near Dicke regime", *Phys. Rev. Lett.* **127** (Dec, 2021) 243602.

[199] G. Ferioli, A. Glicenstein, L. Henriet, I. Ferrier-Barbut, and A. Browaeys, "Storage and release of subradiant excitations in a dense atomic cloud", *Phys. Rev. X* **11** (May, 2021) 021031.

[200] G. Ferioli, A. Glicenstein, I. Ferrier-Barbut, and A. Browaeys, "A non-equilibrium superradiant phase transition in free space", *Nature Physics* (06, 2023) 1–5.

[201] L. D. Landau and E. M. Lifshitz, *Quantum mechanics: non-relativistic theory*, vol. 3. Elsevier, 2013.

[202] G. Grynberg, A. Aspect, and C. Fabre, *Introduction to quantum optics: from the semi-classical approach to quantized light*. Cambridge university press, 2010.

[203] D. Boiron, C. Triché, D. R. Meacher, P. Verkerk, and G. Grynberg, "Three-dimensional cooling of cesium atoms in four-beam gray optical molasses", *Phys. Rev. A* **52** (Nov, 1995) R3425–R3428.

[204] S. Rosi, A. Burchianti, S. Conclave, D. Naik, G. Roati, C. Fort, and F. Minardi, "Λ-enhanced grey molasses on the d_2 transition of Rubidium-87 atoms", *Scientific Reports* **8** (01, 2018) .

[205] R. Bourgain, J. Pellegrino, A. Fuhrmanek, Y. R. P. Sortais, and A. Browaeys, "Evaporative cooling of a small number of atoms in a single-beam microscopic dipole trap", *Phys. Rev. A* **88** (Aug, 2013) 023428.

[206] D. Goncalves, M. W. Mitchell, and D. E. Chang, "Unconventional quantum correlations of light emitted by a single atom in free space", *Phys. Rev. A* **104** (Jul, 2021) 013724.

[207] V. Formichella, L. Galleani, G. Signorile, and I. Sesia, "Robustness tests for an optical time scale", *Metrologia* **59** no. 1, (Dec, 2021) 015002.

[208] H. Hachisu, F. Nakagawa, Y. Hanado, and T. Ido, "Months-long real-time generation of a time scale based on an optical clock", *Scientific Reports* **8** (03, 2018) .

[209] J. Yao, J. A. Sherman, T. Fortier, H. Leopardi, T. Parker, W. McGrew, X. Zhang, D. Nicolodi, R. Fasano, S. Schäffer, K. Beloy, J. Savory, S. Romisch, C. Oates, S. Diddams, A. Ludlow, and J. Levine, "Optical-clock-based time scale", *Phys. Rev. Appl.* **12** (Oct, 2019) 044069.